

WARSAW UNIVERSITY
OF TECHNOLOGY

**Faculty of Electronics and Information
Technology**

Ph.D. Thesis

Andrzej Rychter, M.Sc.

**Measurement Based Characterisation and Modelling
of Micropixel Avalanche Photodiodes**

Supervisor

Associate Professor Janusz Marzec, Ph.D, D.Sc.

Warsaw, 2016

Abstract

This dissertation contains a detailed research of new types of Silicon Photomultipliers which have been developed at the beginning of this century. The author was responsible for measuring new types of silicon photomultipliers (SiPM) which were planned to be used as photosensors in the new calorimeter—ECAL0 in COMPASS experiment in CERN. The prototype of the calorimeter was equipped with Micropixel Avalanche Photodiodes (MAPD detectors from Zecotek), the final detector uses MPPC S12572-010 photosensors from Hamamatsu.

First chapter contains a detailed description of both detectors and examples of their usage in high energy physics experiments. To perform measurements and simulations of detectors, a special automated system with low noise front-end electronics has been designed. The thesis contains a description of the system which consists of three subsystems: low noise front-end electronics with data acquisition system, light source and light spot positioning system and temperature regulation system. Work contains a detailed description and schematic of discrete-elements-based charge sensitive amplifier (CSA). Electrical models of both MAPD and MPPC detectors have been proposed and confirmed with electrical measurements of impedance. A set of histogram based measurements has been performed. The main measured parameters are: electron gain, dark rate, relative photon detection efficiency and correlated noise. A new quenching mechanism of MAPD detector was a motivation to measure and analyse the recovery time. The results have shown that MAPD has very long recovery time and non-exponential recovery characteristic. Electron gain measurements showed that electron gain calculated from dark pulses is smaller due to long recovery time. A special care has been taken to measure the parameters uniformity of detectors. One chapter contains results of spacial distribution of parameters measured with both CSA and fast amplifier. Results of scans with histogram collection showed that the PDE (Photon Detection Efficiency) of MAPD is changing over the surface of the detector. Scans of signal shape revealed that the shape of the MAPD signal is dependent on the position of light flux due to thin contact layer. The simulation of contact layer has been performed and compared with measurement data. A big part of this thesis is a model description and Monte Carlo simulations of Geiger discharge probability in SiPM detector. The model has been based on the MPPC detector. The simulation results contain Geiger discharge probability dependency on the applied supply voltage and the position of primary charge and spectral sensitivity simulation of the model. The results of this work could be very useful for experiments willing to use new types of SiPM photosensors in new detectors systems.

Streszczenie

Rozprawa doktorska zawiera dokładną analizę nowych rodzajów wielopikselowych fotodiod lawinowych (SiPM ang. Silicon Photomultiplier). Głównym zadaniem autora była pomiarowa charakteryzacja nowych detektorów SiPM, które zostały zaplanowane jako detektory światła w nowym kalorymetrze ECAL0 w eksperymencie COMPASS w CERN. Prototyp kalorymetru został wyposażony w detektor MAPD firmy Zecotek (MAPD ang. Micropixel Avalanche Photodiode), jednak ostatecznie w kalorymetrze użyto detektorów MPPC (ang. Multipixel Photon Counters) firmy Hamamatsu.

W początkowym rozdziale autor charakteryzuje oraz porównuje oba typy detektorów światła, przedstawia także ich zastosowania w eksperymentach fizyki wysokich energii. Aby wykonać odpowiednie pomiary oraz przeprowadzić symulacje detektorów, został zaprojektowany i zbudowany specjalny, zautomatyzowany system z niskoszumnym wzmacniaczem ładunkowym zbudowanym w oparciu o elementy dyskretne. Praca zawiera szczegółowy opis systemu, który składa się z: niskoszumnej elektroniki front-end z systemem akwizycji danych, systemu pozycjonowania wiązki światła na powierzchni detektora oraz systemu stabilizacji temperatury. Późniejsze rozdziały zawierają szczegółowy opis pomiarów obu detektorów: MAPD i MPPC. W oparciu o pomiary impedancji, zaproponowane zostały modele elektryczne obu detektorów. Kolejny rozdział przedstawia pomiary oparte o analizę histogramów amplitud odpowiedzi. Głównymi parametrami, które zostały zmierzone są: wzmocnienie elektronowe, szum ciemny, wydajność detekcji oraz szum skorelowany. Nowy mechanizm gaszenia lawiny Geigera w detektorze MAPD był główną motywacją do przeprowadzenia pomiarów czasu relaksacji. Pomiary wykazały, że czas relaksacji detektora MAPD jest bardzo długi, a jego kształt nie jest wykładniczy. Pomiary wzmocnień elektronowych dla impulsów ciemnych wykazały mniejsze wzmocnienie niż w przypadku oświetlania słabymi sygnałami świetlnymi, jest to wynik długiego czasu relaksacji. Szczególną uwagę zwrócono na pomiary parametrów detektora w zależności od miejsca padania wiązki światła. Jeden z rozdziałów zawiera wyniki pomiarów jednorodności parametrów detektora MAPD z wykorzystaniem zarówno niskoszumnego wzmacniacza ładunkowego, jak i szybkiego wzmacniacza do pomiarów kształtu sygnału. Pomiary wydajności detekcji wykazały, że nie jest ona jednakowa na całej powierzchni detektora, a spada nieznacznie w obszarach pomiędzy pikselami. Pomiary jednorodności kształtu sygnału ujawniły wpływ cienkiej warstwy kontaktowej na szerokość impulsu. Ostatni rozdział pracy opisuje model oraz symulacje Monte Carlo prawdopodobieństwa wystąpienia wyładowania Geigera w detektorze MPPC. Przedstawiono wyniki symulacji prawdopodobieństwa wywołania lawiny Geigera w funkcji napięcia zasilania oraz pozycji pierwszej pary

elektron-dziura w obszarze zubożonym. Kolejna symulacja dotyczy zależności prawdopodobieństwa wyładowania Geigera w funkcji długości padającej fali.

Wyniki tej pracy: pomiarowa charakteryzacja oraz zaproponowane modele detektorów mogą być bardzo przydatne dla eksperymentów, które planują korzystać z nowych rodzajów detektorów SiPM.

Contents

Contents	7
1 Introduction	9
2 Silicon Photomultiplier (SiPM) theory and usage	11
2.1 Avalanche Photodiode	11
2.2 Silicon Photomultiplier	15
2.3 Micropixel Avalanche Photodiode (MAPD)	21
2.4 Silicon Photomultipliers in High Energy Physics experiments	24
3 Measurement system for SiPM	35
3.1 Requirements	35
3.2 Front-end electronics for histogram based measurements	38
3.3 Front-end for signal shape measurements	47
3.4 Temperature control system	48
3.5 Light source and positioning system	50
4 SiPM measurement results	54
4.1 Electrical measurements	54
4.2 Histogram based measurements	57
4.3 Recovery time measurements	70
4.4 MAPD electron gain investigation	76
5 Results of SiPM parameter scans	82
5.1 Signal shape scans	83
5.2 Histogram based scans	91
6 Monte Carlo simulation of Geiger discharge	101
6.1 Detector structure	102
6.2 Simulation procedure	112

6.3	Simulation results	114
6.4	Simulation summary	118
7	Conclusions	119
	Bibliography	121
	List of Figures	131
	List of Tables	138

Chapter 1

Introduction

In High Energy Physics, scintillating detectors are used to detect and track high-energy particles. They can also be used as calorimeters to measure their energy [1]. Scintillating detectors use a combination of a scintillator and a light detector. Due to a low intensity of light in common detectors, signal amplitudes would be below noise level for typical light detection method (e.g. using a photodiode and a high-gain amplifier). Thus, it is necessary to use photo-sensors with internal signal amplification. The registration of low-intensity light photons flux is one of the critical issues for experimental physics. The most popular combination is usage of a scintillator with a photomultiplier (PMT). Alternatives for the photomultiplier are e.g. an avalanche photodiode (APD) and a silicon photomultiplier (SiPM).

1. Photomultiplier: PMTs are in use for almost one century and are extremely sensitive light detectors. The PMT multiplies the current produced by incident photons by as much as 10^8 . However, photomultipliers have at least two important drawbacks: they are sensitive to magnetic field and their price is high [2]. What is more, high voltage supply is needed.
2. Avalanche Photodiode: APD is a highly sensitive semiconductor device, that uses a photoelectric effect to convert light to electricity. Due to impact ionization (avalanche effect), APD can achieve an internal current gain effect. This detector delivers a higher signal amplitude than standard photodiodes, and also fast time response. Unfortunately gain of the detector is limited to $\approx 10^3$. For higher bias voltages, the APD get unstable and may enter a Geiger mode, where signal is not dependent on number of incident photos.
3. Silicon Photomultiplier: SiPM has been developed at the beginning of this century. This device, like a photomultiplier, can detect single photons and achieve electron

gain up to $1 \cdot 10^6$. Basically, the SiPM detector can be described as a matrix of avalanche photodiodes, working in Geiger mode, connected in parallel. A single avalanche photodiode includes an internal amplification stage, and can detect only one photon at time. However, parallel operation of many photodiodes gives quasi-linear behaviour of the device. The amplification is achieved with high (but much smaller than in PMT) reverse bias voltage [3]. The SiPM detectors are an alternative to PMTs, can achieve high electron gain and are insensitive to magnetic field.

Author is a member of the COMPASS experiment in CERN. A group from Warsaw University of Technology is involved in building a new electromagnetic calorimeter called ECAL0. ECAL0 is a modular, multi-channel, sampling electromagnetic calorimeter with external dimensions of approximately $2 \text{ m} \times 2 \text{ m}$. It consists of 194 9-channel modules, giving a total of 1746 photodetector channels [4]. The author was responsible for measuring new types of silicon photomultipliers (SiPM) which were planned to be used as photosensors in the new calorimeter: Micropixel Avalanche Photodiodes (MAPD). MAPD works like a traditional SiPM but has different structure and mechanism for avalanches quenching without quenching resistors [5][3]. While SiPM detectors with quenching resistors are already well measured and understood, MAPD detector is still relatively new technology which has not been well characterized yet. The main motivation of this dissertation was to measure and propose physical models of both traditional type and novel SiPM detectors. The thesis contains also detailed description and measurements of SiPM detector produced by Hamamatsu called Multi Pixel Photon Counter (MPPC). The MPPC is a good example of a traditional type SiPM detector with quenching resistors. In order to perform measurements, an automated measurement system had to be designed. Detectors have been measured in different ways. The work contains SiPM measurements such as: electrical measurements with vector analyzer, histogram based measurements, signal shape measurements and recovery time measurements. In addition to regular measurements, the scans of parameters uniformity have been performed. The Monte Carlo simulation of Geiger discharge probability has been also conducted.

Chapter 2

Silicon Photomultiplier (SiPM)

theory and usage

In this chapter, Author describes the topology and theory of a new type of silicon photomultiplier called micropixel avalanche photodiode (MAPD). A short description of an avalanche photodiode and a standard SiPM detector will be also included as an introduction.

2.1 Avalanche Photodiode

Avalanche Photodiodes (APD) have been designed and developed over 50 years ago. For a long time these detectors were sensitive only to near infra-red wavelengths and its active area was very small (below 1 mm²). After a large development of the APD, an increase of sensitive area and sensitivity in the blue and near-ultraviolet wavelength region, the detector began to be used in high energy physics (HEP) experiments.

The physics of an APD

The operation principle of an APD is based on the conversion of the energy of photons into free charge carriers in the semiconductor bulk and their further multiplication via the process of impact ionization [6]. A structure of APD includes p-n junction, which is reversely biased. Comparing to PIN diodes, APD's structure is divided into two regions: depleted region for charge collection and avalanche region for signal multiplication (see figure 2.1). The charge carriers created in the depleted region move in the electric field towards the electrodes. When charge carriers travel through an avalanche region, where a very high electric field exist, they acquire enough energy to produce electron-hole pairs

by impact ionization. The newly created charge carriers may create new ones, thus an avalanche of electrons and holes moving through the junction builds up.

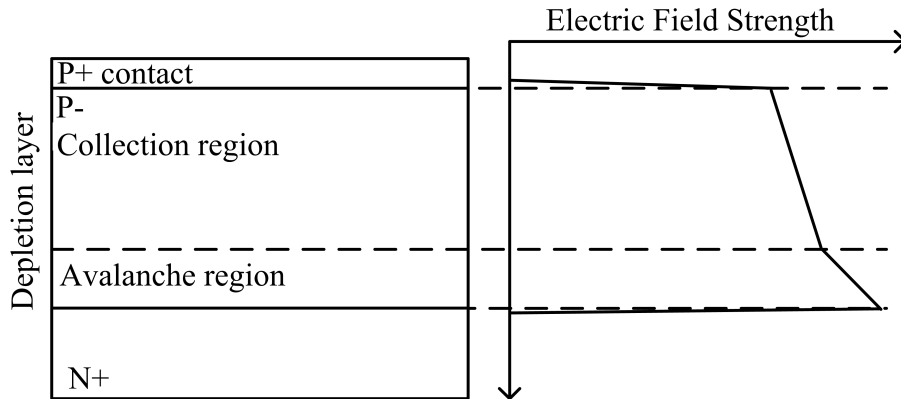


Figure 2.1: The structure and electric field strength distribution of an APD with HPK structure.

Most of available APD detectors are fabricated in so called N/P reach trough structure, where light is incident from N-side of the silicon junction. In this configuration a depletion region is too deep for short wavelengths (ultraviolet and blue) giving the sensitivity range from ≈ 450 nm to 1000 nm. For a structure where photons are incident from P+ side of the silicon (P/N reach through and HPK Reverse Structure) it is possible to obtain a peak sensitive wavelength of 400 nm [7]. An example of an APD with blue light sensitivity is Hamamatsu S8148. The S8148 have been used in an electromagnetic calorimeter in CMS experiment in CERN, where the active medium is a fast radiation tolerant lead-tungsten scintillator, which produces light in the blue-violet region [8].

Theory of impact ionisation

Impact ionisation is an important charge generation mechanism. An electron (or hole) in the conduction (or valence) band gains its energy by external electric fields and becomes energetic enough that can create an electron-hole pair by colliding with an electron in the valence band and exciting it to the conduction band. The number of electron-hole pairs created by carrier running in unit length is called impact ionization coefficient. This coefficient is different for electrons and holes. Impact ionization coefficient of electron and hole is commonly denoted as α and β respectively. Figure 2.2 shows the impact ionization coefficient of silicon as a function of the electric field, α is always higher than β . Impact ionisation can only occur when the particle gains at least the threshold energy for ionisation from the electrical field [9].

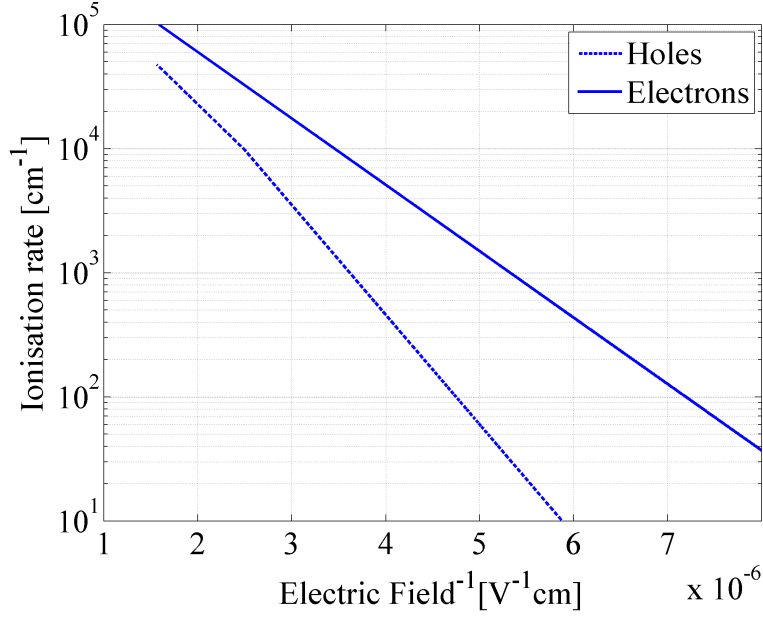


Figure 2.2: Impact ionisation coefficient as a function of inversion of electric field[7].

As shown in figure 2.2, it is important to note that the ionisation coefficient increase rapidly with increasing electric field. Due to this strong dependence, the operating voltage of devices can be strongly reduced by minimizing the width of the depletion region, which results in a high electric field within the device.

Responsivity and Gain

The current generated in APD is calculated as follows:

$$I = R_0 \cdot M \cdot P_S \quad (2.1)$$

where R_0 [A/W] is the spectral responsivity of the APD, M is the internal gain and P_S [W] the incident optical power. The gain of the APD depends on the reverse bias voltage applied (see figure 2.3). According to applied reverse voltage, the APD can work in three modes: no gain, proportional and Geiger mode.

Proportional mode

Figure 2.3 shows dependence of APD gain (M) versus reverse bias voltage for a hypothetical detector. For low bias voltages the APD operates as a standard photodiode and there is no charge amplification, thus $M = 1$. In linear region, $\log(M)$ is linearly proportional to applied reverse voltage. In this region one carrier is amplified to finite number of carriers by means of impact ionisation. Impact ionisation will repeat until carriers will exit the

region with high electric field. Carriers will be collected at the electrodes. In this mode the average current is strictly proportional to the incident optical power. The internal gain M is typically tens or hundreds.

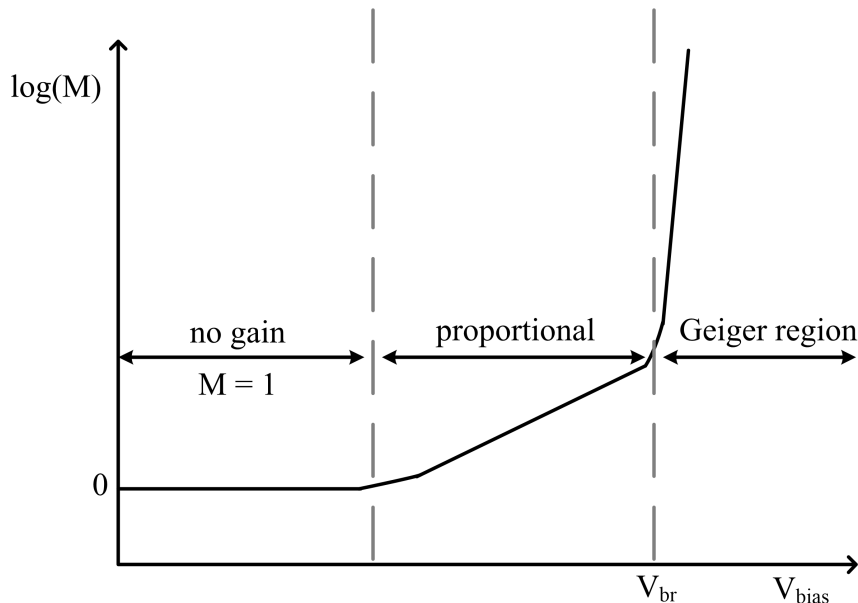


Figure 2.3: Gain versus bias voltage in avalanche photodiode, adopted from [10].

Geiger mode

It is very important to point out that for higher values of electric field, the ionisation rate of holes reaches values close enough to ionisation rate of electrons (see figure 2.2). This results in a strong positive feedback loop of electron and hole multiplication. In principle, an exponentially growing number of avalanches could be created when the product of ionisation rates of both electrons and holes is higher than one in the region with high electric field. The supply voltage at which the critical value of the electric field is reached is called the breakdown voltage (V_{br}). When APD is biased above V_{br} , device will operate in Geiger mode and conduct large current. The difference between supply voltage and breakdown voltage is commonly called overvoltage (ΔV). Once a pair of an electron and a hole starts an avalanche, the growth of current continues as long as the electric field in the device is negligibly affected by a presence of the growing current and the growing population of electrons and holes. The population of electrons and holes in the avalanche region and the associated photocurrent grow exponentially in time. The higher the overvoltage, the faster the growth. Therefore, an avalanche initiated by the

absorption of a single photon will cause the diode current to grow to a value limited by a circuit's resistance. This current will persist unless bias voltage is reduced to (or below) breakdown voltage; doing so restores the APD to the light-sensitive state.

There are two ways to stop an avalanche: passive and active. In passive quenching, there is a quenching resistor R_q in series connected to the diode. Once the APD is turned on and the current reaches maximum value, the voltage dropped across quenching resistance will result in lowering the voltage on APD and thus lowering the strength of electric field in avalanche region. The APD voltage recovers exponentially to its nominal value with time constant $R_q C$, where C is a capacitance of the APD. In active-quenching a series resistor is replaced by an electronic circuit. The circuit senses if the APD starts to self-discharge, and then quickly discharges it to below breakdown voltage with a shunting switch. After sufficient time to quench the avalanche, it then recharges the APD quickly by using another switch.

2.2 Silicon Photomultiplier

Silicon Photomultipliers are a rapidly developing photosensitive devices. Currently, they are a main alternative to well known photomultipliers.

The SiPM is a photon-counting device consisting of multiple APD 'pixels' operating in Geiger mode. Every pixel of the SiPM detector consists of a diode and a quenching resistor (figure 2.4). Every APD pixel outputs a pulse signal when it detects an incident photon. While operating in Geiger mode, each SiPM pixel operates as a binary device and signal from individual pixel is not dependent on number of incident photons. However, the whole SiPM detector in an analog detector, the output signal is a sum of signals from all pixels. The magnitude of the output signal allows us to determine the number of pixels fired, which is proportional to intensity of incident light.

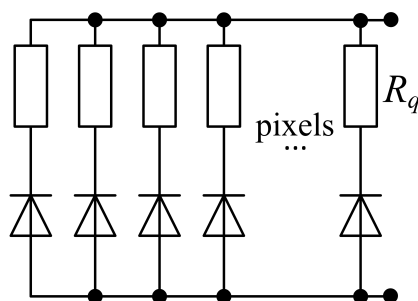


Figure 2.4: Schematic of a SiPM matrix of avalanche diodes and quenching resistors.

Main parameters of Silicon Photomultiplier

Dynamic range

Since each pixel of the SiPM detector operates as a binary device, the dynamic range of the detector is determined by its total number of pixels. SiPM detector produces signal when any of the APD pixel 'triggers'. When many pixels are fired at the same time, the output is the sum of the pulses from these pixels. For a matrix of N_{pixels} pixels, the dynamic range of the detector is limited by the condition that:

$$\left(\frac{N_{ph} \cdot PDE}{N_{pixels}} \right) < 1 \quad (2.2)$$

where N_{ph} is the number of photons, PDE is photon detection efficiency. If the number of detected photons is much smaller than the number of pixels, the response is fairly linear but it saturates when number of photons gets comparable to the number of pixels [11]. The average number of photons should be much less than a number of pixels in the SiPM detector. Thus, saturation characteristics is described by:

$$N_{signal} = N_{pixels} \cdot \left(1 - \exp \left(\frac{-N_{ph} \cdot PDE}{N_{pixels}} \right) \right) \quad (2.3)$$

An example of a response function for the SiPM detector is presented in figure 2.5

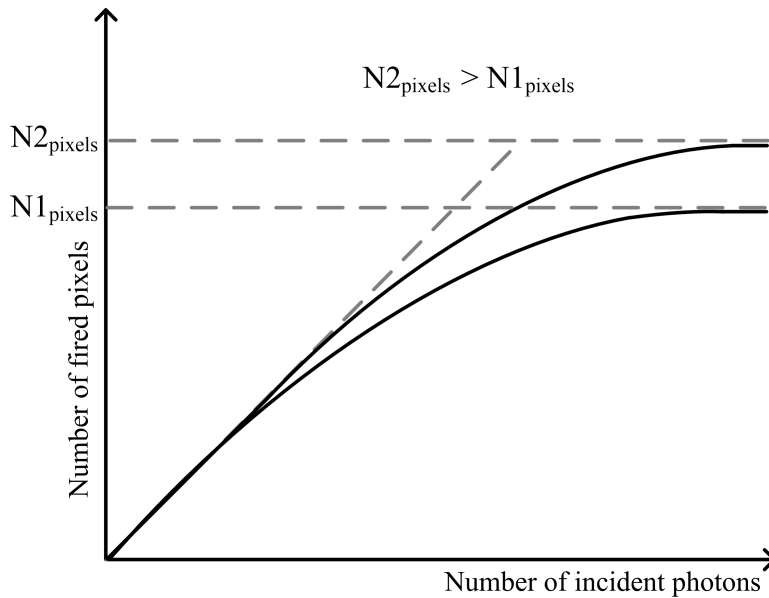


Figure 2.5: Signal response linearity of SiPM detectors with two different number of pixels: $N2_{pixels} > N1_{pixels}$.

The linearity of the SiPM response is mainly limited by number of pixels. The higher the number of pixels, the higher number of photons can be detected. Increasing the

number of pixels reduces their size at the same time, and in result also detector's electron gain and *PDE*. The *PDE* is reduced because it is not possible to reduce the size of quenching resistors and metallic connection grid while reducing the size of pixels, this leads to lower fill factor which is the the ratio of the effective active area of the detector to the total detector's surface. The electron gain is reduced due to smaller pixel capacitance.

Electron gain

Electron gain in the SiPM is proportional to the charge released in the avalanche, and its typical values range from 10^5 to 10^6 . An integral of signal current, equals to charge produced in the avalanche and it is proportional to single pixel capacitance C_{pix} and the overvoltage (ΔV), which is a difference between bias operating voltage (V_{op}) and the breakdown voltage (V_{br}) (see eq. 2.4 and 2.5).

$$Q = C_{pix} \cdot \Delta V \quad (2.4)$$

$$\Delta V = V_{op} - V_{br} \quad (2.5)$$

The charge Q is the total generated charge and the gain M for this process can be defined by equation:

$$M = \frac{Q}{q} \quad (2.6)$$

Where q is the elementary charge.

Dark counts

In Geiger mode a single thermally generated electron or hole can initiate an avalanche in APD pixel. This gives the main limitation of increasing the sensitive area of Si avalanche structures operated in single photon-counting mode at room temperature [11]. An avalanche can be produced by incoming photon or by a free carrier. Signals from incident photons and free carriers look identical. The dark pulses are mainly due to carriers thermally generated in the depleted region. Shockley-Read-Hall (SRH) generation [12] carriers give much contribution to dark rate which is temperature dependent [13]. Two tunneling processes can cause an additional generation of electron-hole pair in the depletion region: trap-assisted tunneling and direct band-to-band tunneling. The first tunneling is much more probable. It is called trap assisted tunneling (TAT) through Shockley-Read-Hall (SRH) generation-recombination centres [12]. The probability of the tunneling effect does not depend on temperature, and it increases with the supply voltage.

A fit function that describes a dark rate (DR) dependence on overvoltage and temperature has been reported in [14]. Equation 2.7 shows a function of dark rate dependence:

$$DR(\Delta V, T) = A \cdot (\Delta V - V_0) \cdot \left(\frac{T}{298}\right)^{3/2} \cdot \exp\left(-\left(\frac{E}{2kT} - \frac{E}{2k \cdot 298}\right)\right) \quad (2.7)$$

where T is absolute temperature, A represents the ratio of dark rate to overvoltage at $T = 298$ K (25 °C)(in MHz/V). V_0 is the offset of breakdown voltage calculated from the dark rate with respect to that obtained from gain measurements, and E is the band gap energy [14].

Dark rate depends on:

- number of generation centres
- temperature
- overvoltage

The rate of thermally generated free carriers can be reduced by cooling the detector. Another possibility is to operate the SiPM at lower bias voltages resulting in lower electric field what unfortunately lowers gain and PDE . The dark rate is dependent on the quality of epitaxial layer, and can be reduced during production process by minimizing the number of generation-recombination centres, caused by impurities and crystal defects [2].

Correlated noise

Correlated noise of the SiPM is the name for avalanches which are triggered by other avalanches. Correlated noise is also called CTAP (Cross-Talk and After-Pulsing) noise because it consists of two different phenomena called optical cross-talk and after-pulsing. A Cross-talk occurs when an avalanche produces a photon which may travel to a neighbouring pixel. As result two or more pixels can be fired at almost the same time. The optical crosstalk can be reduced with special grooves (trenches) between the cells. The trench should completely surround each pixel (see figure 2.6) [15]. Lower electron gain is also advantageous.

Afterpulsing takes place when charge trapped in a pixel starts another, delayed avalanche in the same pixel. The charge of afterpulses is smaller due to recovery time, if the pixel voltage has not come back to the nominal value. The longer delay time, the higher afterpulse amplitude. As a result, the measured number of events, having one avalanche within the specified gate, will be lower than the expectation. This fact can be used to get an estimate of the correlated noise factor. It was shown for some types of SiPM, that

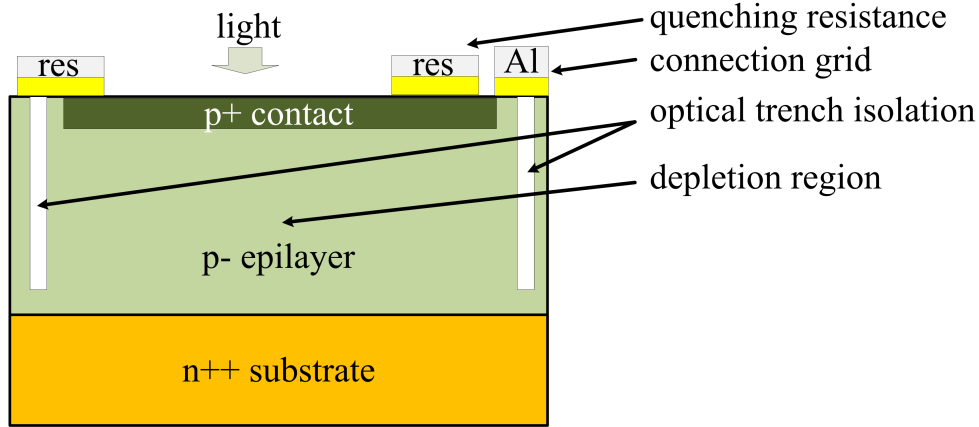


Figure 2.6: Cross section of pixels surrounded by an optical trench isolation preventing penetration of generated secondary photons to neighbouring pixels.

the dependence of correlated noise on temperature is very small and on overvoltage is quadratic [14].

Photon detection efficiency

The photon detection efficiency (PDE) is the product of quantum efficiency of the active area (QE), a geometric factor (ϵ) and the probability that the incoming photon triggers the breakdown P_{trig} .

$$PDE = QE \cdot \epsilon \cdot P_{trig} \quad (2.8)$$

The quantum efficiency is dependent on the wave length and ranges up to 80-90%. When SiPM is p-silicon on an n-substrate, the QE is higher for blue light. When the structure is inverted, n-silicon on p-substrate, the device is more sensitive for green and red light.

The triggering probability is a probability that a carrier (electron or hole) traversing the multiplication region triggers an Geiger avalanche. P_{trig} is dependent on the overvoltage and the position where primary pair electron-hole is generated [2]. If the electron-hole pair is born at a certain position, then the probability that neither the electron nor hole causes an avalanche is given by $(1 - P_e)(1 - P_h)$, consequently the probability that either the electron or the hole initiates a Geiger avalanche is given by:

$$P_{trig} = P_e + P_h - P_e \cdot P_h \quad (2.9)$$

where P_e is a probability that an electron in depletion layer will trigger an avalanche and P_h is analogously defined [16]. Both probability functions are connected with impact ionisation rates thus P_e is always higher than P_h and both are dependent on position in

depletion layer and in result on electric field.

The geometric factor (ϵ) is very critical and limits the *PDE*. It is also called fill factor and it describes the ratio of the active region to the total window area. Larger pixels give higher fill factor because when using same technology the area of a dead space, required for quenching resistors and connection grid, remains the same single pixel.

Electrical model

The equivalent electrical model of SiPM is presented in figure 2.7. Every diode has a quenching resistor R_q to stop the ongoing avalanche. Capacitance of single pixel is modelled as C_{pix} capacitor. The value of C_{pix} defines the amount of charge collected during a breakdown. There is also a parasitic capacitance C_q associated with the quenching resistor R_q and single parasitic capacitor C_g associated with the connection grid [17]. A fired pixel is modelled as a current source connected in parallel with C_{pix} . For the Geiger discharge signal, capacitances (C_{pix} and C_q) act in parallel. Fall time of a signal is determined by recharging C_{pix} and C_q through R_q . Larger pixels have higher pixel capacitance thus the recovery time will be longer for the same R_q .

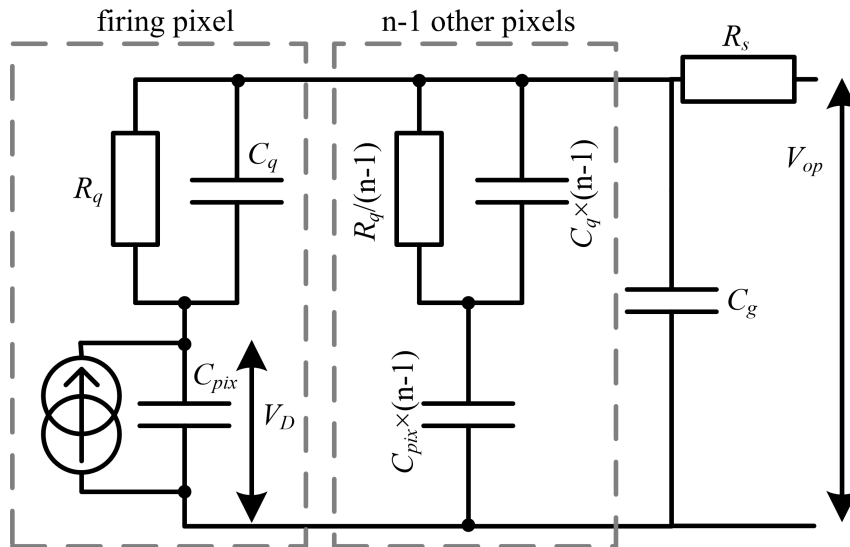


Figure 2.7: Schematic of an equivalent electrical model of SiPM detector.

Figure 2.8 shows how the current changes with time as the SiPM pixel goes into and recovers from an avalanche. During operation, when SiPM is reversely biased with operating voltage V_{op} , current in every pixel is determined with an equation: $i(t) = (V_{op} - V_D)/R_q$. When the pixel is in the 'ready' state, $V_D = V_{op}$ and as a result no current is observed; $i(t) = 0$. A pair of an electron and a hole is created in the depleted region and an avalanche is triggered at the time t_i . At this moment, SiPM pixel's capacitance

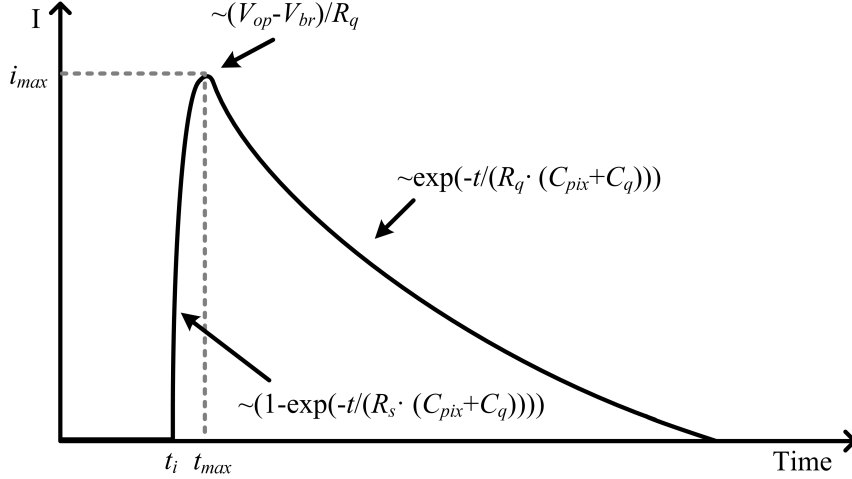


Figure 2.8: Current pulse generated by an SiPM pixel [10].

C_{pix} and capacitance of quenching resistor C_q begin to discharge causing V_D to decrease and $i(t)$ to increase. The current $i(t)$ can reach the maximum value of $i_{max} \approx (V_{op} - V_{br})/R_q$ at the time t_{max} when R_q quenches the avalanche. Between t_i and t_{max} , $i(t) \sim (1 - \exp(-t/(R_s \cdot (C_{pix} + C_q))))$, where R_s is series resistance of the SiPM. For times greater than t_{max} , C_{pix} and C_q charge through R_q , and the current decreases as $i(t) \sim \exp(-t/(R_q \cdot (C_{pix} + C_q)))$. Because $R_s \ll R_q$, the output current pulse has an asymmetric shape. After a pixel recharges to the bias voltage with time constant of $R_q \cdot (C_{pix} + C_q)$, the device becomes ready to detect the arrival of a new photon [10]. An integral of $i(t)$ with respect to time from t_i to infinity is the area under this curve, which equals the net charge Q produced in the avalanche [11].

2.3 Micropixel Avalanche Photodiode (MAPD)

Micropixel Avalanche Photodiode is a new type of SiPM detector. Its design was firstly introduced by Z. Sadygov et al. in 2006 [18]. The detector was produced by Zecotek company. Zecotek offers three different MAPD devices: MAPD-3A, MAPD-3B and MAPD-3N with different pixel sizes [19]. Like the SiPM detector, the MAPD consists of matrix of pixels. Unlike to traditional SiPM, MAPD pixel structures are buried deep in epitaxial layer and are called micro-wells. With respect to the previous devices, the production of the MAPD requires more sophisticated technology such as an epitaxial growing of extremely pure silicon wafers and a deep ion implantation with various dopants [18]. The principle of the MAPD is to fight limitation of pixel densities. Pixel densities in SiPM are mainly limited with fill factor. Novel MAPDs do not have quenching resistors on top

of sensitive window thus the fill factor can be almost 100% [3].

Parameters

Looking at main MAPD parameters given in the table 2.1, one can see that the crucial parameter — *PDE* is at a reasonable level with very high pixel density. As it was mentioned earlier, the absence of quenching resistors result with 100% fill factor. That allows MAPD-3N to gain *PDE* of 30% with pixel density of 15 000 /mm². MAPD-3B has 15% *PDE* with pixel density of 40 000 /mm². Zecotek MAPDs feature high *PDE* at pixel densities and linearity range that are unachievable for older types of SiPMs [5][20]. The dark rate of the MAPD detector is around $1 \cdot 10^6 \text{ s}^{-1}/\text{mm}^2$. There is no official information about correlated noise of this detector.

Table 2.1: Comparison of Zecotek MAPD and Hamamatsu MPPC parameters [19]

	MAPD-3N	MAPD-3B	MPPC S12572-010P
detector area	$3 \times 3 \text{ mm}$	$3 \times 3 \text{ mm}$	$3 \times 3 \text{ mm}$
number of pixels	15 000 /mm ²	40 000 /mm ²	10 000 /mm ²
pixel size	$8 \times 8 \text{ }\mu\text{m}$	$5 \times 5 \text{ }\mu\text{m}$	$10 \times 10 \text{ }\mu\text{m}$
operating voltage	$\sim 90 \text{ V}$	$\sim 70 \text{ V}$	$\sim 70 \text{ V}$
<i>PDE</i>	30%	15%	12%
fill factor	100%	100%	33%
<i>GAIN</i>	$10^4 - 10^5$	3×10^4	1.3×10^5
dark count	$10^5 - 10^6$	$\sim 10^6$	$\sim 10^5$

Topology

The topology of the MAPD is shown in figure 2.9. The device consists of n-type substrate and p-type epitaxial layer. For the MAPD-3N device, N+ type micro-wells are equally distributed in the p-type epitaxial layer with spacing of 8 μm [21][5]. There are three alternating p-n junctions from p+ contact to substrate. First and third junction are reversely biased, the middle one is biased in forward direction. The photocurrent multiplication takes place only in the p-n-p-n junction areas, where first p-n junction is fully depleted [22]. The second, forward biased junction result with 0.5-0.7V potential well, which can be seen in energy diagram in figure 2.9. An array of independent potential n+ wells is formed in depleted layer. Total area of the photosensitive layer is divided into individual multiplication channels. The role of quenching resistors is taken by potential wells. Multiplication of the avalanche takes place in the first p-n junction where the strength of electric field is the highest. During avalanche, electrons accumulated in po-

tential micro-well make electric field less strong which leads to breaking the multiplication process. The initial electric field is restored due to sufficient leakage current of the last p-n junction to substrate [5]. The signals from operating individual pixels are summed up on the common bus by thin p+ contact layer.

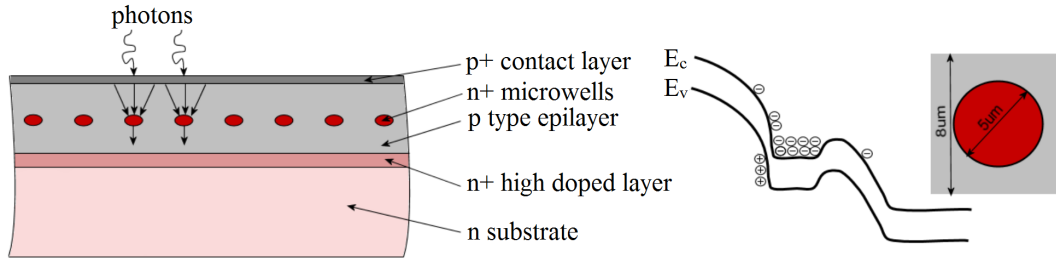


Figure 2.9: To the left: a sectional view of MAPD pixels. To the right: energy band diagram across the APD junction and a top view of the MAPD pixel.

Electrical model

The electrical model of MAPD is different from the one of a traditional SiPM. The terminal capacitance $C_{terminal}$ of the detector will be the sum of all pixels capacitances and parasitic capacitance C_g .

$$C_{terminal} = n \cdot C_x + C_g \quad (2.10)$$

where n is the number of pixels in the detector. C_g corresponds to the capacitance of the metallic connection frame of the detectors anode to the substrate. The analysis of the surface of the connection frame and to the total surface of the detector, showed that $C_g = 0.035 \cdot C_{terminal}$. Single pixel consists of two capacitors, what is showed in figure 2.10. Capacitors C_1 and C_2 refer to alternating p-n-p-n junction where multiplication process takes place. Therefore fired pixel is modelled as two current sources in parallel with C_1 and C_2 . Since the generated charge is accumulated in potential wells between both epitaxial layers, the capacitance of fired pixel C_{pix} is a parallel connection of C_1 and C_2 . For MAPD-3N detector, both epitaxial layers have the same thickness, so $C_1 = C_2 = C_{12}$:

$$C_{pix} = C_1 + C_2 = 2 \cdot C_{12} \quad (2.11)$$

When measured terminal capacitance is taken into account, a single pixel can be modelled as capacitor C_x which is a serial connection of C_1 and C_2 (see eq. 2.12):

$$C_x = \frac{C_1 \cdot C_2}{C_1 + C_2} = C_{12}/2 = C_{pix}/4 \quad (2.12)$$

The terminal capacitance of MAPD-3N detector can be expressed as:

$$C_{terminal} = n \cdot C_{pix}/4 + C_g \quad (2.13)$$

It is also predicted that small parasitic resistance R_s of p+ connection layer will be noticeable [3].

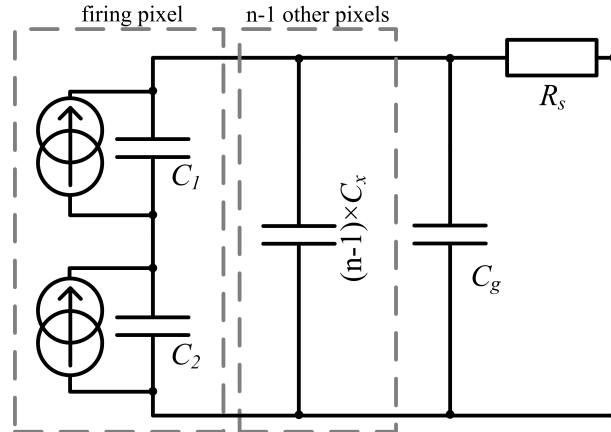


Figure 2.10: Schematic of an equivalent electrical model of MAPD detector.

2.4 Silicon Photomultipliers in High Energy Physics experiments

Silicon Photomultipliers (SiPM) have become increasingly used in high energy physics experiments (HEP), as well as in medical and astrophysical applications [23]. In HEP experiments, silicon photomultipliers have been already introduced in calorimeter and tracker detectors. The first usage of SiPM detectors on a big scale was the near detector complex (ND280) in T2K (Tokai to Kamikoa, Japan) neutrino experiment at J-PARC [24]. From author's point of view, the most important is the new electromagnetic calorimeter ECAL0 at the COMPASS experiment [25] in CERN. The prototype of this detector was equipped with SiPM detectors from Zecotek: MAPD-3N and MAPD-3A [26]. SiPM detectors have also received considerable interest for application in medical imaging modalities such as Positron Emission Tomography (PET) and Single Photon Emission Computed Tomography (SPECT) [27]. In this section, a short review of SiPMs usage examples in new HEP detectors and medical equipment will be presented. Since the usage of SiPM detectors is gaining popularity, only experiments in which the author was or is involved will be mentioned.

SiPM detectors in a new calorimeter ECAL0 at COMPASS

COMPASS experiment at CERN

COMPASS (COMmon Muon Proton Apparatus for Structure and Spectroscopy) is a high-energy physics experiment at the Super Proton Synchrotron (SPS) at CERN in Geneva, Switzerland. The purpose of this experiment is the study of hadron structure and hadron spectroscopy with high intensity muon and hadron beams [28]. The main goal of the COMPASS experiment at CERN is a better understanding of the structure and dynamics of hadrons [29]. Nearly 220 physicists from 13 countries and 24 institutions work in COMPASS. The beginning of the COMPASS experiment is February 1997 when the experiment was approved conditionally by CERN. The final Memorandum of Understanding was signed in September 1998. In 2010 an extension of the COMPASS program has been approved by the CERN Research Board. It consists of a set of measurements to study the structure of hadrons in Deep Virtual Compton Scattering (DVCS), Hard Exclusive Meson Production (HEMP), SIDIS, Polarized Drell-Yan and Primakoff reactions [28]. The COMPASS setup is located at the end of the M2 beam line of the CERN SPS accelerator.

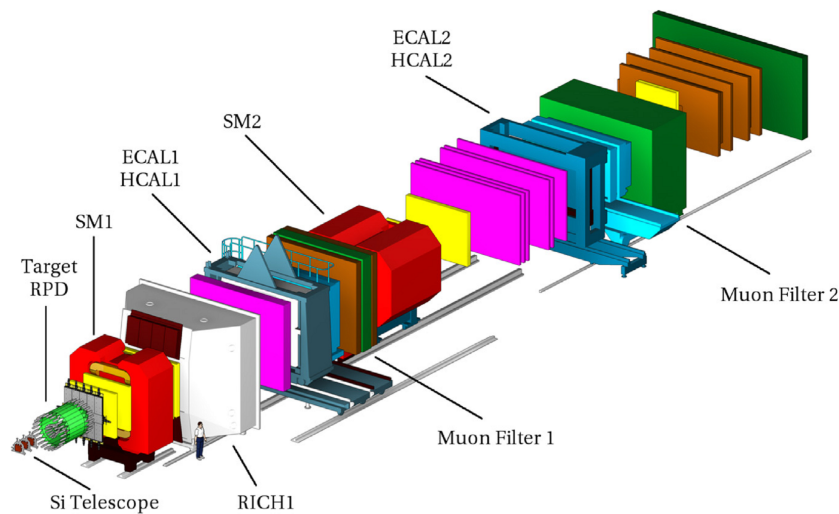


Figure 2.11: Three-dimensional view of the COMPASS setup for measurements with hadron beams. The beam comes from the left side. The upstream part of the setup (beamline) is not shown here [29].

New electromagnetic calorimeter ECAL0.

ECAL0 calorimeter is a new high-granularity large-angle electromagnetic calorimeter in COMPASS experiment [25][4]. Author is a member of the Polish team from Warsaw University of Technology which is involved in the process of design, assembly and tests of

the new calorimeter. Warsaw group was responsible for front-end electronics for Silicon Photomultipliers. Author was involved in measurement of parameters and modelling of new types of SiPM detectors with high pixel densities: MAPD from Zecotek and second generation MPPC detectors from Hamamatsu.

ECAL0 is a modular, multichannel, sampling calorimeter. The ECAL0 will supplement the COMPASS spectrometer for the GPD studies. The main tasks of the ECAL0 are the following:

- together with existing calorimeters ECAL1 and ECAL2 ensure a hermiticity of the setup for photons from DVCS,
- help in reduction of background,
- enlarge the kinematic domain of the DVCS registered by COMPASS.

The external dimensions of ECAL0 are approximately 2.5 m by 2.5 m, the size of the central hole is 81 cm by 59 cm. The whole detector consists of 194 modules, 1746 SiPM detectors and readout channels. Figure 2.12 shows the pictures of the detector during the final assembly in CERN.

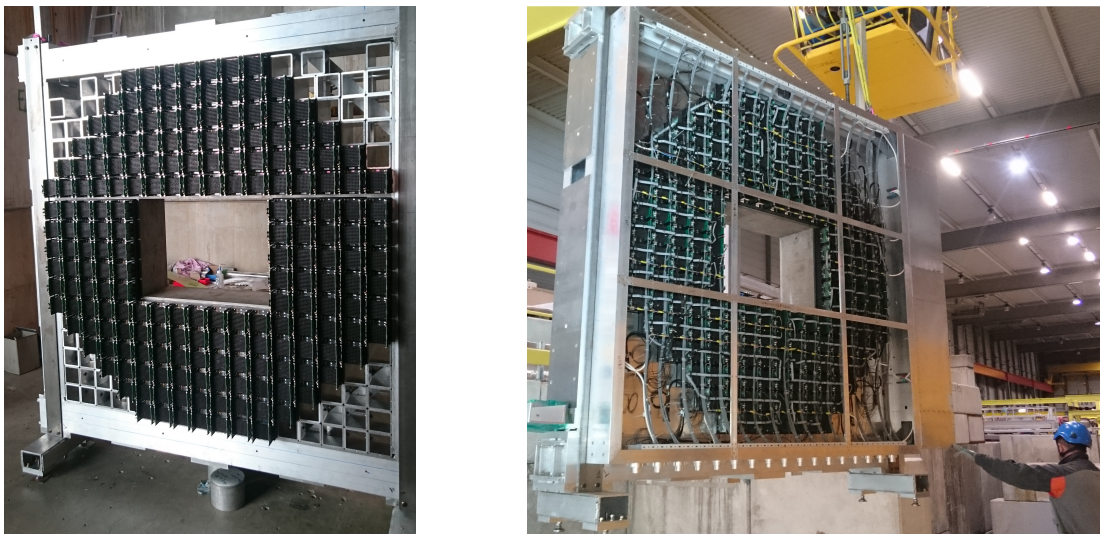


Figure 2.12: To the left: ECAL0 calorimeter before the final assembly. To the right: ECAL0 detector after cabling, transportation to the final beam position. CERN, April 2016.

Each module consists of the calorimeter and the photodetector unit [26]. They are detachable for service and for transportation. The schematic picture of the module is presented in figure 2.13. The calorimeter unit is a sandwich of alternating perforated stamped lead plates and injection-molded polystyrene-based scintillator tiles read out by means of WLS (Wave-Length Shifting) fibres passing through holes in the scintillator and lead.

Bicron BCF-91AMC WLS fibres shift light from blue to green (494 nm). The output light pulse has time constant of 12 ns. The single module consists of 9 readout channels. There are 109 sampling layers, each layer consisting of 0.8 mm thick lead plate with dimensions $119.8 \times 119.8 \text{ mm}^2$ and nine 1.5 mm thick scintillator tile ($39.8 \times 39.8 \text{ mm}^2$) [26]. The light from the scintillator plates of each channel is collected by 16 Bicron BCF-91AMC WLS fibres (1.2 mm), forming a 6.5 mm bundle at the output, along with 1 clear fibre for LED monitoring [4].

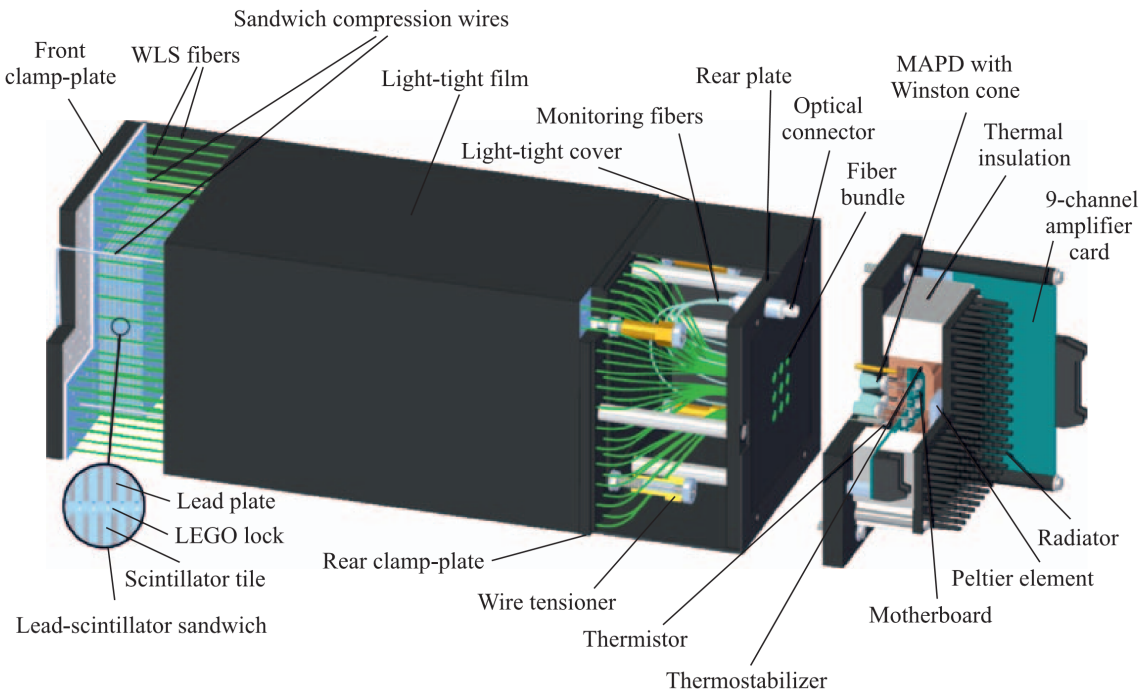


Figure 2.13: Schematic of a module from ECAL0 calorimeter [4].

The photodetector unit incorporates photodetectors, accompanying front-end electronics, high voltage power supply and a Peltier-based temperature stabilisation system. Electronics of the photodetector module consists of three PCBs (Printed Circuit Board):

1. motherboard with nine photodetector sockets,
2. amplifier board with 9 channels of shaping amplifiers,
3. slow control board with high voltage and temperature regulation systems.

Since the ECAL0 calorimeter is installed close to the magnet, the photodetector should be insensitive to magnetic field and PMTs cannot be used. The maximal amplitude of the light pulse was predicted to be around 40000 photons, so pixel density should be as high as possible. Initially, the MAPD-3N detector from Zecotek Company was the only

candidate for the photosensor due to high pixel density (135000 pixels) and thus sufficient linearity and dynamic range. This is very important, because it allows to cover wide range of photon energies. During tests of the prototype detector, a new photodetector from Hamamatsu MPPC S12572-010 has been brought to market [30]. As a result, the prototype of the calorimeter was equipped with MAPD detectors and the final detector uses MPPC S12572-010 photosensors from Hamamatsu. Since the fibre bundle is 6.5 mm in diameter, while the sensitive area of both detectors is square-shaped and 3×3 mm, the polystyrene Winston cone light guide glued to the detector surface is used to increase the light collection [31]. Temperature stabilisation system consists of Peltier element which is glued to the outside surface of the thermostabilizer with heat-conducting glue. The hot side of the Peltier element is cooled by a radiator [31] (see figure 2.14). In the prototype of the calorimeter, the MAPD detectors in metallic TO-39 packages are placed directly on the thermostabilizer which has nine pairs of isolated holes for connection to the motherboard. The MPPC detectors are in ceramic SMT packages, therefore a special aluminium PCB interface boards had to be designed in order to keep stable temperature of the photodetectors. The right picture in figure 2.14 shows the interface board. From one side of the board, pins for connection to motherboard are soldered. On the second side of the interface board, 9 MPPC detectors with Winston cones are mounted.

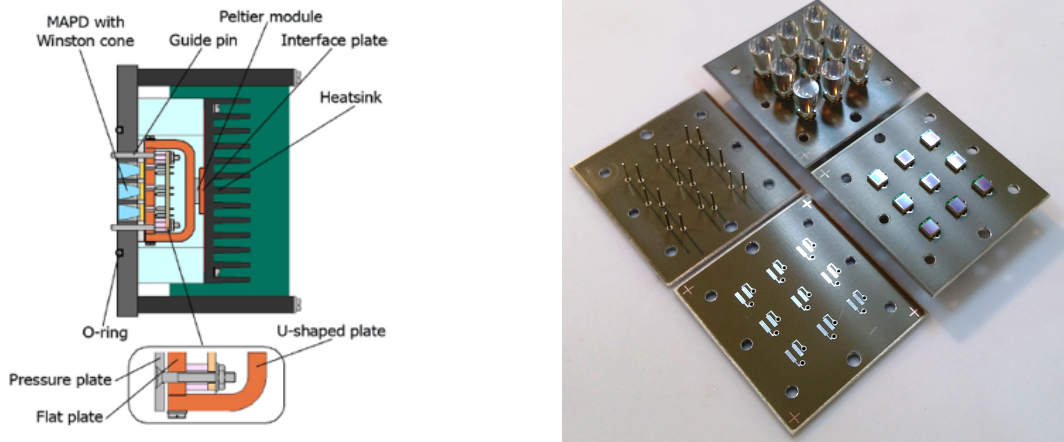


Figure 2.14: To the left: MAPD-3N detectors with Winston cones placed on the thermostabilizer. To the right: MPPC aluminium interface PCB boards with smt pads for MPPC detectors on top side.

SiPMs in T2K

The principal goal of the Tokai to Kamioka (T2K) project is to measure neutrino oscillation parameters by searching for the appearance of electron neutrinos in a beam of muon

neutrinos and by performing precision measurements of the muon neutrino disappearance [24]. The experiment uses two detector facilities, the distant detector at Kamioka (295 km from the target) is placed 2.51° off-axis to measure beam neutrinos. A near detector complex at J-PARC is used to monitor the neutrino beam, measure neutrino event rates and to help minimize systematic uncertainties in the measurements of neutrino oscillation parameters [24]. The near detector complex houses two detectors: an on-axis interactive neutrino grid detector (INGRID) and an off-axis near detector, ND280. A group from Warsaw University of Technology was involved in process of assembly of the side muon range detector (SMRD), which is a part of the ND280 detector set [32]. The principal goals of the SMRD are to measure the muon momentum and angle for charged current quasi-elastic CC-QE reactions to help determine neutrino energy, to identify backgrounds from beam neutrino interactions in magnet yokes and surrounding walls and to provide a cosmic trigger signal for calibration of the inner detectors [33].

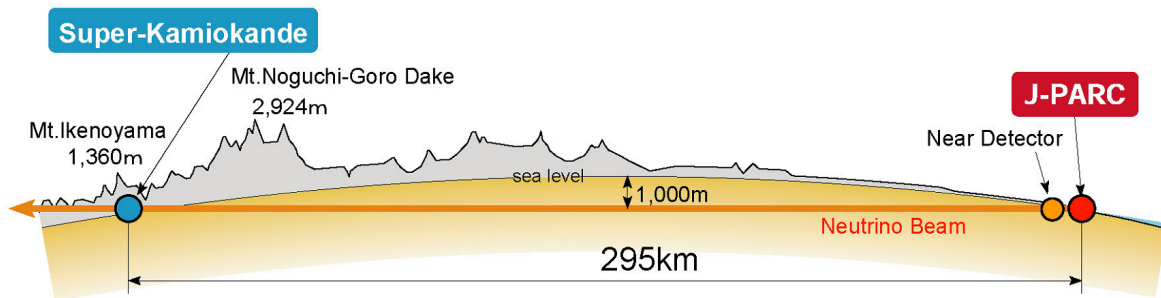


Figure 2.15: Location of the detectors in T2K experiment [32].

The ND280 detector uses scintillator detectors and embedded WLS fibers, with light detection from the fibers by photosensors that must operate in a magnetic field and fit in limited space inside the magnet [14]. Multi Pixel Photon Counters (MPPC) [14] developed for T2K by Hamamatsu were chosen as the photosensor for all ND280 scintillator based detectors, in total, about 60,000 MPPCs were produced for T2K. The total number of MPPCs used for the SMRD is 4016. The standard 1×1 mm MPPC detector was customized, the sensitive area was increased to provide better acceptance of light from 1 mm diameter Y11 Kuraray fibers [14]. A customized MPPC detector is based on S10362-11-050C, it has 667 pixels and the sensitive area of 1.3×1.3 mm [32].

A group from Warsaw University of Technology (WUT) was involved in process of assembly of SMRD detector and quality assurance of MPPC photosensors. For this purpose a special, dedicated and fully automated apparatus for measuring the parameters of the MPPC photodiodes has been designed [34]. The aim of the project was to cre-



Figure 2.16: To the left: A single scintillator module of the SMRD detector - without a light-housing [32]. To the right: a part of automated system for measurement of MPPC detectors: the temperature stabilised feeder for 32 MPPC with preamplifier and LED flasher [34].

ate a compact, portable device allowing measurement of gain, breakdown voltage, PDE (relative), dark rate and cross-talk, afterpulse ratio, with minimum operator interaction required [34]. The system designed by the team from WUT was used to measure approx. 1200 MPPCs designated for installation in the SMRD sub-detector (see figure 2.16).

SiPMs in a new LHCb Tracker

The LHCb (Large Hadron Collider beauty experiment) detector is a single-arm forward spectrometer covering the pseudorapidity range $2 < \eta < 5$, designed for the study of particles containing b or c quarks. The LHCb detector will be upgraded during the Long Shutdown 2 (LS2) of the LHC in order to collect data at instantaneous luminosities up to $2 \cdot 10^{33} \text{ cm}^{-2}\text{s}^{-1}$ [35]. The current tracking detector consists of three tracking stations downstream of the magnet with silicon microstrips in the region closest to the beam-pipe (Inner Tracker, IT) and straw tubes outside (Outer Tracker, OT). During the upgrade, the IT and OT will be replaced by a completely new detector, the Scintillating Fibre (SciFi) Tracker [36], based on scintillating fibres read out by Silicon Photomultipliers. The new tracker will cover the area of 6 m by 5 m and consist of three stations. Each detection plane will have 12 modules. The modules will be constructed from 2.4 m long fibre mats and read out by multi channel SiPM detectors. A module consists of eight 2.4 m fibre-mats. The module is split in the middle, where each fibre mat is equipped with a mirror. The fibres have a diameter of 0.25 mm and are wound into ribbons (mats) with six staggered layers of densely packed fibres as shown in figure 2.17 [35].

The fibres are read out using Silicon Photomultipliers that are enclosed in so-called

“read-out boxes” (ROBs) located at the top and bottom of every module [35]. The photons produced along the trajectory of the particle are propagated to the fibre end and further to the detector. Each pixel of the SiPM channel can detect one photon, thus the signal from individual channel is proportional to the total number of fired pixels. The particle position can be calculated with a weighted mean value of the channel signal [36]. A S10943-3183 Hamamatsu MPPC detector will be used as a photosensor. S10943-3183 detector is a multichannel array consisting of 128 channels. Each channel is composed of 96 pixels of size $57.5\ \mu\text{m}$ by $62.5\ \mu\text{m}$ for a total channel height of $1.0\ \text{mm}$ and width of $250\ \mu\text{m}$. S10943-3183 is a third generation detector, which has trenches between individual pixels for optical cross-talk suppression.

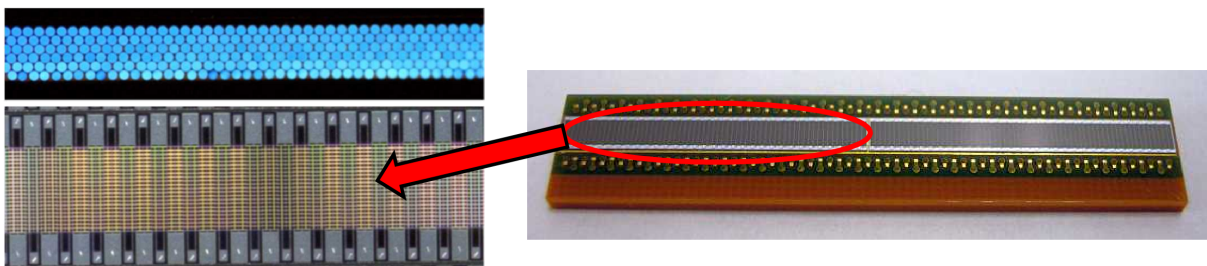


Figure 2.17: To the top-left: a front view of SciFi matrix which is optically coupled a MPPC array detector (bottom-left: zoomed view of MPPC detector). To the right: a photo of Hamamatsu detector S10943-3183 [37]

A total of 4608 SiPMs will be used in new LHCb Tracker, corresponding to around 590000 channels. The MPPC arrays will be operated at $-40\ ^\circ\text{C}$ to reduce the effects of neutron radiation damages and increased dark rate. The small area of each SiPM channel, combined with fast read-out and shaping, make it possible to operate the SiPMs at the single photo-electron level in the LHCb upgrade environment [35]. The group from Warsaw University was involved in quality assurance process of fibre mats and the final modules.

SiPMs in medical imaging applications: PET and SPECT

SPECT and PET detectors are another field where SiPM detectors can replace Photomultipliers or Avalanche Photodiodes (APDs). Positron emission tomography (PET) is a nuclear medicine, functional imaging technique which uses scintillator crystals and photodetectors to detect a pair of $512\ \text{keV}$ gamma annihilation photons moving in approximately opposite directions. Conventional PET systems employ photomultiplier tubes (PMTs) or avalanche photodiodes to detect the scintillation light. Recently, the combination of PET with MRI (magnetic resonance imaging) has become a topic of interest,

as such systems have great potential for soft tissue imaging and whole-body imaging [27]. However, PMTs are sensitive to magnetic fields, and therefore cannot be operated inside an MR system [38]. The use of Silicon Photomultipliers, which are insensitive to magnetic field, could allow to design integrated solution that preserve PET and MR performance. The faster response time means that SiPMs, unlike APDs, are TOF (time-of-flight) compliant. The time of flight (TOF) method allows much better rejection of scattered photons and random coincidence events in PET [39]. The multimodality approach (PET/MR) will be more and more requested in the clinical practice. The SiPM seems to be the choice for future systems being MR compatible, compact and with high performance [38].

SiPM arrays

During the last ten years, a number of PET detector modules with SiPMs or prototype PET scanners for small-animal and human imaging have been developed. The compact size of the SiPM detector allows direct one-to-one coupling between the scintillation crystal and the photosensor, what leads to better timing and energy resolutions. However, the one-to-one coupling technology requires a huge volume of readout and processing electronics if no electric signal multiplexing or encoding scheme is properly applied [40]. To overcome the problem of high volume of readout electronics, SiPM arrays have been brought to market by many manufacturers. The advantage of using SiPM monolithic arrays, instead of single devices assembled together, is that it is possible to easily achieve good uniformity of gain, *PDE* and dark rates over the pixels. Moreover, the gap between pixels can be minimized, thereby improving the effective area of the SiPM arrays as a whole [41] (see figure 2.18).

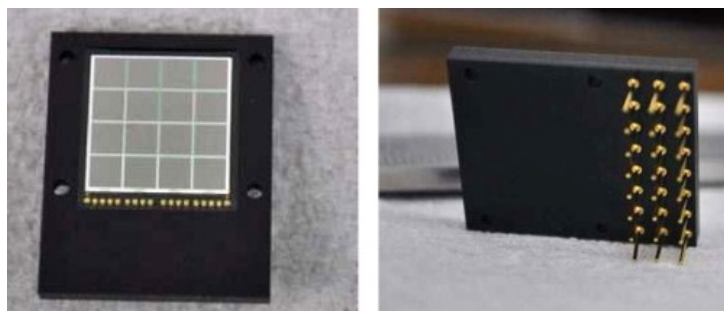


Figure 2.18: Pictures of the 4×4 MPPC array developed by Hamamatsu, picture adopted from [41].

Particularly worth to mention are position-sensitive arrays that may replace conventional multi-anode PMTs in certain applications. Traditional PMTs coupled with pixelated scintillator arrays are often used in single photon emission computed tomography

(SPECT) and positron emission tomography (PET) applications, although their resolution is typically limited to a few mm FWHM (10 mm for SPECT), due to the pixel size of the scintillator fabricated in the array. Very recently, submillimeter spatial resolution based on newly developed SiPM arrays has been reported for PET scanners, but the resolution is still limited to the 0.8-1.2 mm level, partly because of restrictions due to the positron range [42].

Digital SiPM arrays

The most important drawbacks of the monolithic scintillator and multi-channel light sensors concept are the need for dedicated calibration procedures and large number of data channels. Both issues, however, can be solved with modern readout and processing electronics. For example, the number of data that needs to be transferred can be reduced drastically by on-line FPGA (Field-programmable gate array) processing [43]. A relatively new type of photosensor that is very interesting is the so-called digital silicon photomultiplier (dSiPM). This detector offers negligible electronic noise, low photon signal transit time spread, and a *PDE* that is comparable to state-of-the-art photomultiplier tubes or analog SiPMs [44].

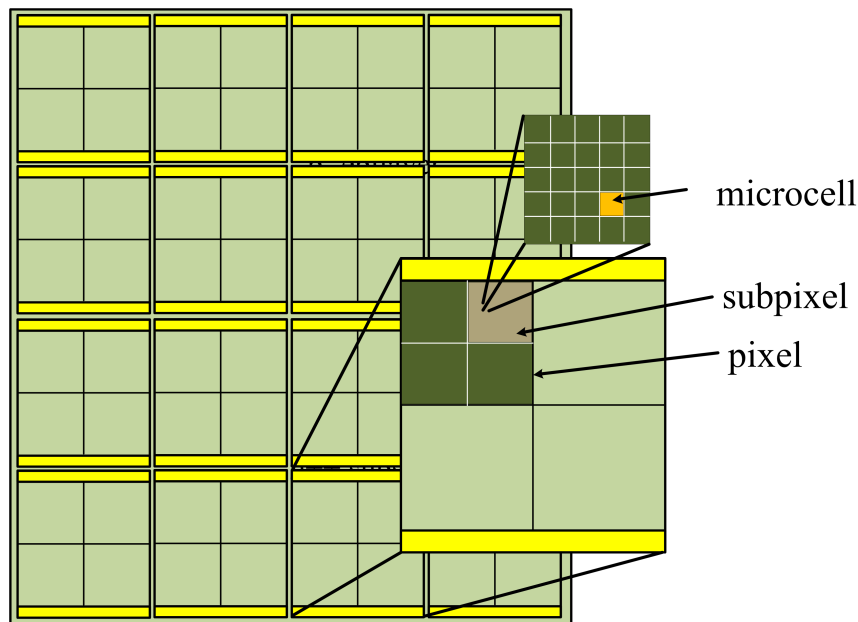


Figure 2.19: Schematic representation of the digital silicon photomultiplier (dSiPM) array. The larger inset depicts a zoom on a single die consisting of four pixels. Each pixel contains 6396 microcells (a number of which are shown in the smaller inset) that are arranged into 4 subpixels.

Figure 2.19 shows the prototype array of dSiPMs (DPC-6400-44-22 from Philips Dig-

ital Photon Counting). dSiPMs consist of a large number of single-photon avalanche photodiodes (SPADs), yet with active quenching as opposed to passive quenching (with quenching resistors). Signals of individual SPADs are digitized, what practically eliminates all electronic readout noise [43]. Furthermore, the SPADs are kept inactive once they have triggered, until a global reset is issued. In result, dSiPMs do not suffer from correlated noise (afterpulses). Digital readout from individual pixels result in lower dynamic range, fortunately this has little consequence for the readout of monolithic scintillators, because of the relatively low number of scintillation photons hitting on each sensor pixel [43]. Each microcell of dSiPM has an additional control circuitry for active quenching of the SPAD after breakdown. Similar to analog SiPMs the breakdown of a SPAD can occur due to either photon-generated or thermally generated charge carriers. The microcell control circuitry includes also functionality for active recharging of the diodes as well as selective enabling/disabling of individual cells. By disabling the cells with high number of thermally generated charge carriers, it is possible to drastically reduce the dark count rate of the detector.

Vacuum Silicon Photomultiplier Tube

The VSiPMT (Vacuum Silicon PhotoMultiplier Tube) is a hybrid photodetector, which has been invented in 2007. The purpose of the detector is to use a SiPM for large detection volumes. The main idea of VSiPMT was to replace the classical dynode chain of PMT with a SiPM detector [45]. In a VSiPMT, the SiPM acts as an electron detector, electron-hole pairs are created by ionization, therefore for this process to happen there is an energy threshold for photo-electrons impinging on the surface of the SiPM. Photoelectrons emitted by a photocathode are accelerated and focused by an electric field towards a small focal area covered by a SiPM [46]. A couple of prototypes of the Vacuum Silicon PhotoMultiplier Tube (VSiPMT) have been produced by Hamamatsu in 2014, the measurements have shown that the VSiPMT seems to be a very good competitor of the conventional PMT, with some practical advantages [45].

Chapter 3

Measurement system for SiPM

3.1 Requirements

Most of SiPM measurements are based on illuminating the surface of the detector with short light pulses and analysing its response. Most of the parameters are strongly dependent on the detector temperature and applied reverse bias voltage, thus the temperature control and high voltage control systems has to be designed. Measurement of the parameters of SiPM detector requires also stable and short light pulses. The light source system has to be remotely controlled. To measure the uniformity of parameters, a movable light source with a proper light spot focusing is required. Figure 3.1 presents a simplified schematic of the measurement system. In principle, SiPM detector is placed inside the light-tight box. The surface of the SiPM is illuminated with a light source via an optical fibre and a proper lens. SiPM signal is amplified and digitized for further analysis.

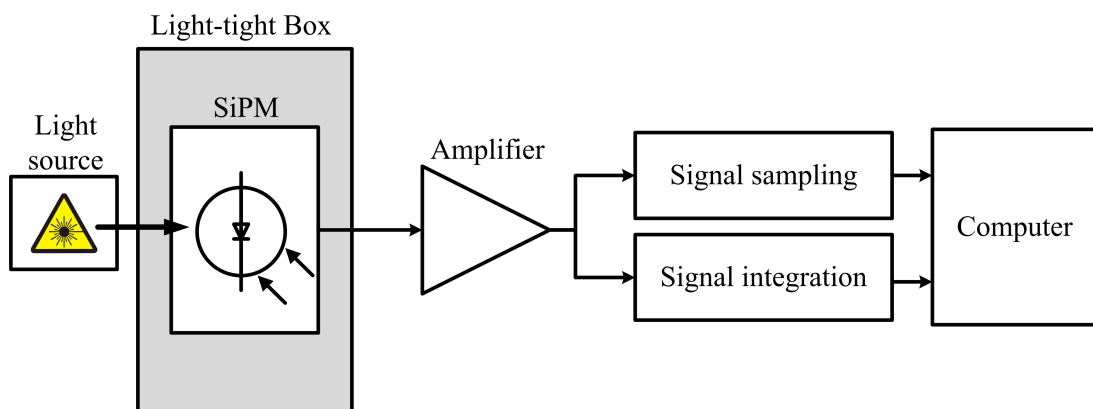


Figure 3.1: A simplified schematic of measurement system consisting of: light-tight box with SiPM detector inside, light source, amplifier circuit and data acquisition system for signal sampling and integration.

Two types of measurements were planned to be performed, thus two types of front-end

electronics and DAQ (data acquisition) systems had to be developed: signal integration and signal shape sampling. Measurement of signal charge are called histogram based measurements. Front-end electronics consists of two stages: a low noise charge sensitive amplifier (CSA) and a second stage amplifier for signal shaping. A charge to digital converter was used for signal integration. Example of signal charge histogram has been presented in figure 3.2. Another measurement system was designed for measurement of shape of the SiPM signal. The system consisted of a wide bandwidth amplifier and an oscilloscope with Ethernet connection for signal waveform sampling (right plot in figure 3.2).

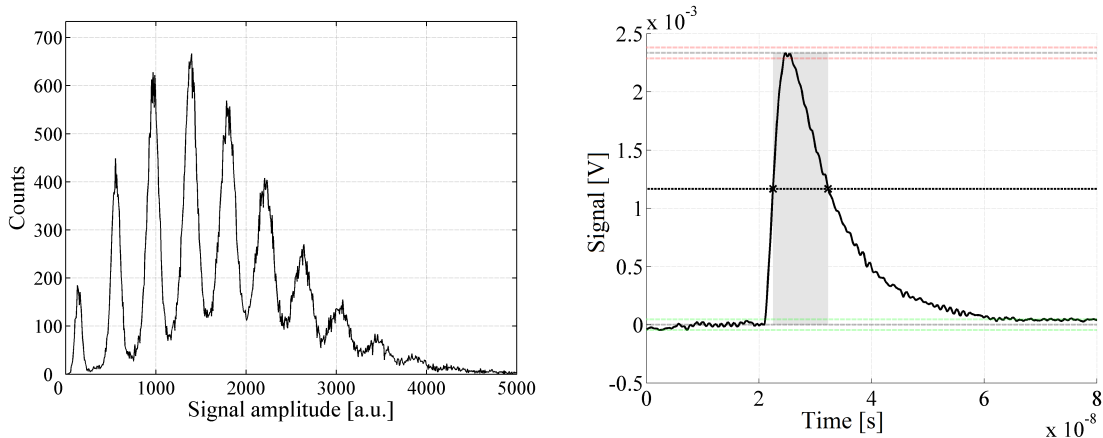


Figure 3.2: To the left: signal charge histogram example. To the right: signal waveform sampled with an oscilloscope and full width at half maximum (FWHM) calculation.

Light-tight box

The central part of the measurement system is a light-tight box with a SiPM detector inside. The box is made of a standard aluminium toolbox of dimensions $580 \times 380 \times 275$ mm. The size of the box was determined by dimensions of the XYZ moving stage to be mounted inside (see figure 3.4). The inside of the box is covered with a black material in order to prevent light leaks and photon reflections from aluminium walls. Figure 3.3 shows the measurement system: a light-tight box with power supplies, a pulse generator, VME crate with charge to digital converter (QDC), a laser system and a computer as the main controller. Part of water cooling system and a controller for three stepper motors are mounted on the front wall of the light-tight box. The top power supply to the right is the power supply of the 50 W Peltier cell.

Figure 3.4 shows the inside of the light-tight box. All elements inside are mounted on a solid aluminium optical breadboard. An aluminium thermostabilizer plate is well fixed

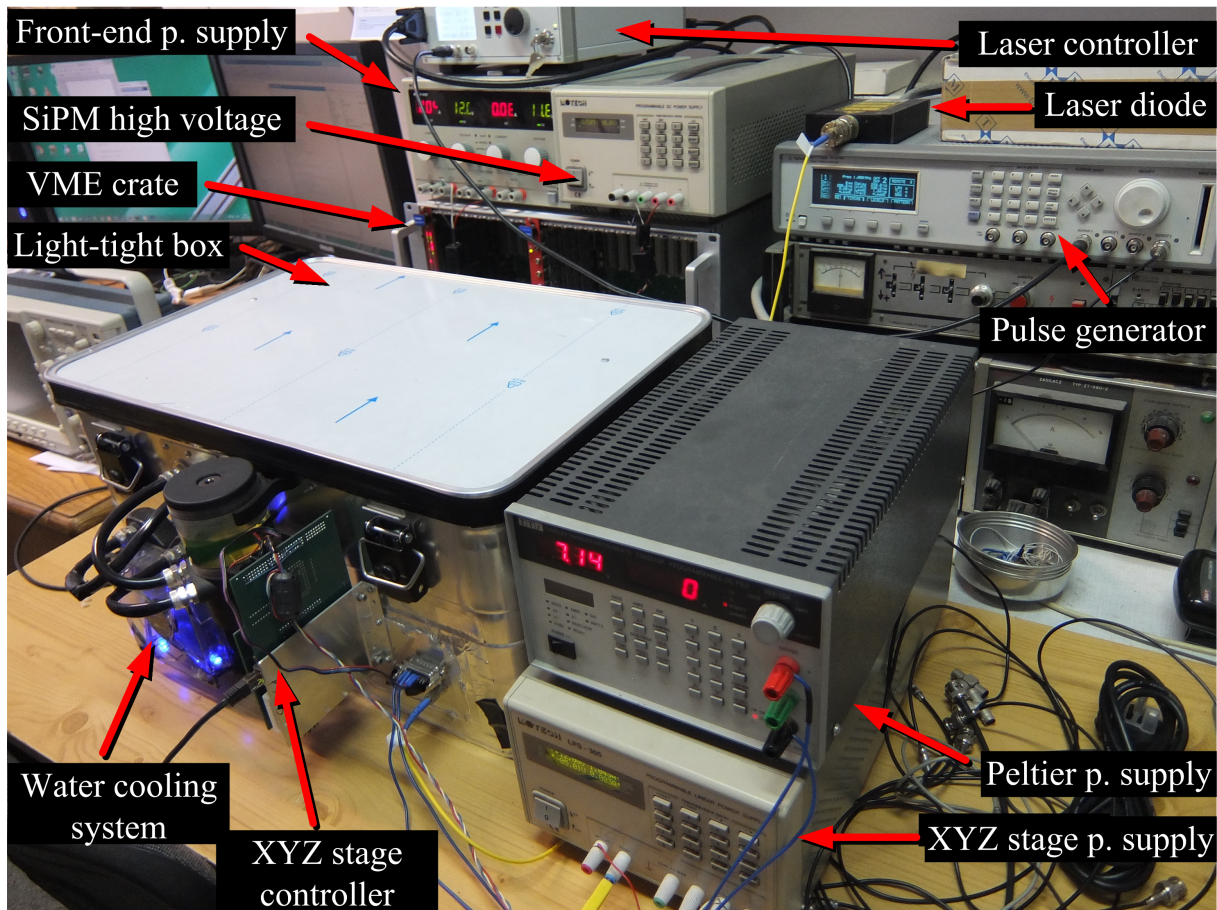


Figure 3.3: A photo of the light-tight box with water cooling system mounted on the front wall and accompanying electronics.

and positioned in front of the XYZ moving stage. The SiPM detector is directly mounted on one side of the thermostabilizer. The temperature of the thermostabilizer plate is controlled with a Peltier cell and a temperature sensor for feedback. The cold side of the Peltier cell is glued with a thermal grease to the thermostabilizer. A water heat exchanger is attached to the hot side of the Peltier cell. A water pump and a radiator with fan are outside the box, which helps to keep stable temperature and prevents from heating the air inside the box. The front-end electronics PCB (pre-amplifier and voltage regulator circuit) is attached close to the thermostabilizer plate. A light spot positioning system inside the box consists of an XYZ moving stage with three stepper motors, collimator and microfocus lens attached on the top of the stage. The controller board of the motors is attached to the front wall outside the box.

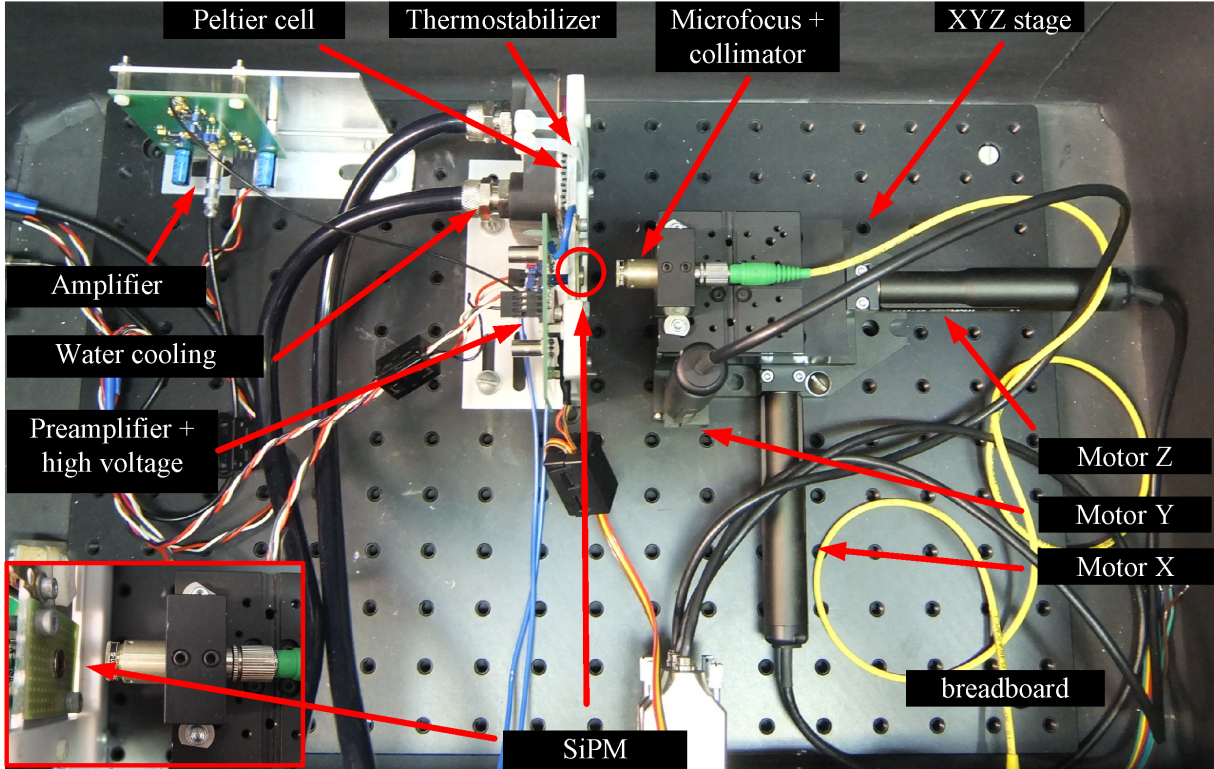


Figure 3.4: A photo of the inside of the light-tight box.

3.2 Front-end electronics for histogram based measurements

While performing a histogram based measurements, signal to noise ratio must be high enough in order to calculate a detector's parameters. The equivalent noise charge (ENC) of front-end electronics must be significantly lower than signal charge of a detector response for single photon in desired working conditions. This implies usage of a low noise charge preamplifier, proper signal shaping and selecting proper width of the integration window. SiPM detectors with high density of pixels have relatively low electron gain, what is the result of a small pixel size. The MAPD-3N detector, for example, has relatively high dark rate and terminal capacitance. Due to the fact of high dark rate, the shaping of the output signal must be fast. Fast signal shaping and high terminal capacitance of the detector results in dominant role of voltage noise of the input amplifier in ENC . Thus, the amplifier has to have very low voltage noise (in practise less than $1\text{ nV}/\sqrt{\text{Hz}}$). Amplifiers with low voltage noise, that are available on the market, have bipolar transistors as an input stage. However, the bipolar transistor has an unacceptable level of current noise. As a result, it was necessary to design a custom CSA using discrete elements, with J-FET transistors as an input stage.

Charge sensitive preamplifier

CSAs are widely used as a front-end due to their low noise and insensitivity of the gain to the detector capacitance variations. A schematic of a designed CSA is presented in figure 3.5. The generated charge Q is integrated onto a small feedback capacitance C_f , which gives a step of the voltage signal at the output of the CSA [47]. An input stage of the designed CSA is a pair of J-FET (junction gate field-effect transistor) transistors (Q1 and Q2) connected with a cascode configured PNP transistor (Q3), which keeps drains of J-FETs at a constant voltage. A $270\ \Omega$ drain resistor R_d is responsible for conducting a quiescent current in the J-FET transistors. The output stage of the designed CSA is a pair of two bipolar transistors (Q4 and Q5).

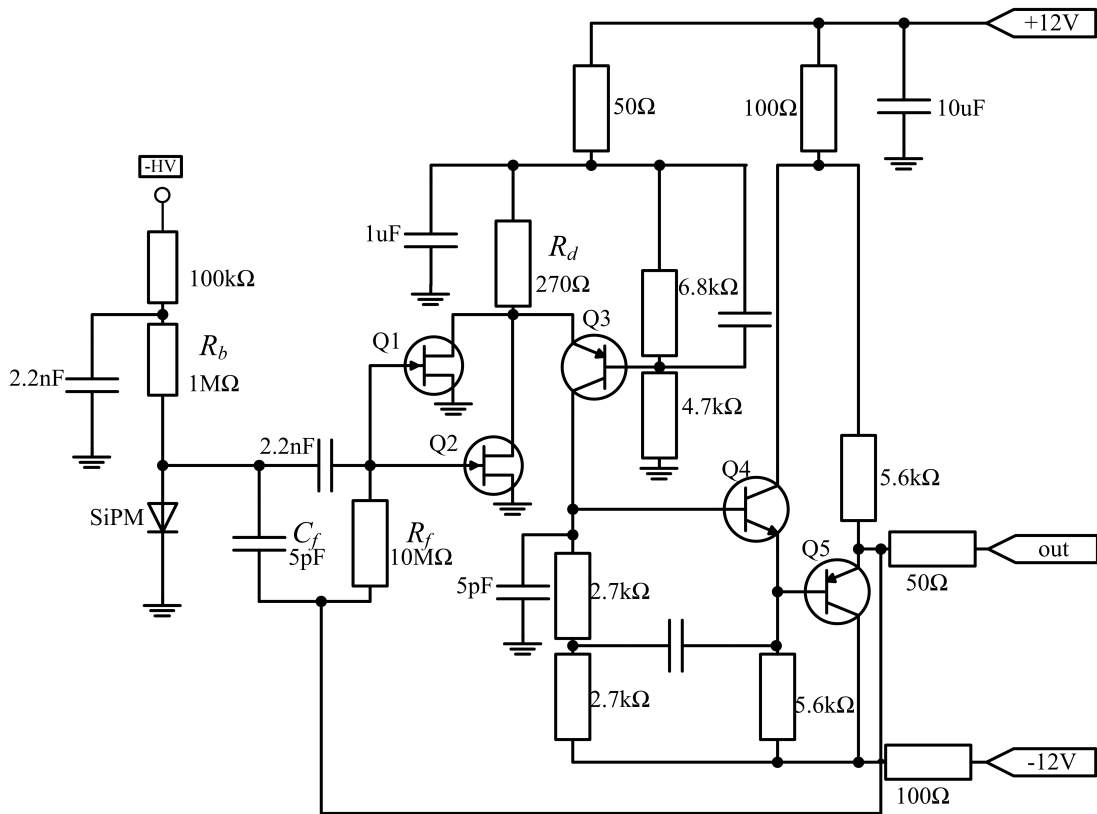


Figure 3.5: A schematic of a low noise charge amplifier used in the measurement system.

In the CSA, the voltage noise is dominated by the noise of the input transistor. The current noise is associated with the detector's leakage current, the resistance of the detector biasing circuit and the feedback resistor of the charge amplifier. A noise simulation has been performed (described later in this section), and in result the first stage of a designed charge amplifier is a pair of a low-noise J-FETs, instead of a single transistor, as this gives better noise performance.

The signal from the charge amplifier is fed to a shaping amplifier which provides required pulse shaping and noise filtration to maximize signal to noise ratio.

Shaping amplifier

The second stage of the front-end electronics consists of two inverting operational amplifiers making a shaping circuit. The DC gain of a first amplifier is 10. It is based on a low noise operational amplifier-LMH6624. Its input voltage noise is very low and equals $0.92 \text{ nV}/\sqrt{\text{Hz}}$. The second amplifier is based on wide bandwidth current feedback AD8000 and has DC gain of ≈ 2 .

Simple RC-CR circuit would introduce a signal undershoot when the amplifier pulse attempts to return to baseline. This is a result of the long exponential decay of the preamplifier output pulse. Most spectroscopy amplifiers incorporate a pole-zero cancellation circuit to eliminate this undershoot. For this purpose a resistor R_{PZ} is added in parallel with the capacitor C_D in shaping circuit (see figure 3.6). The cancellation requirement leads to condition given in equation 3.1.

$$R_{PZ} \cdot C_D = \tau_i \quad (3.1)$$

where τ_i is the time constant of an exponential input function, which is an output signal from the CSA.

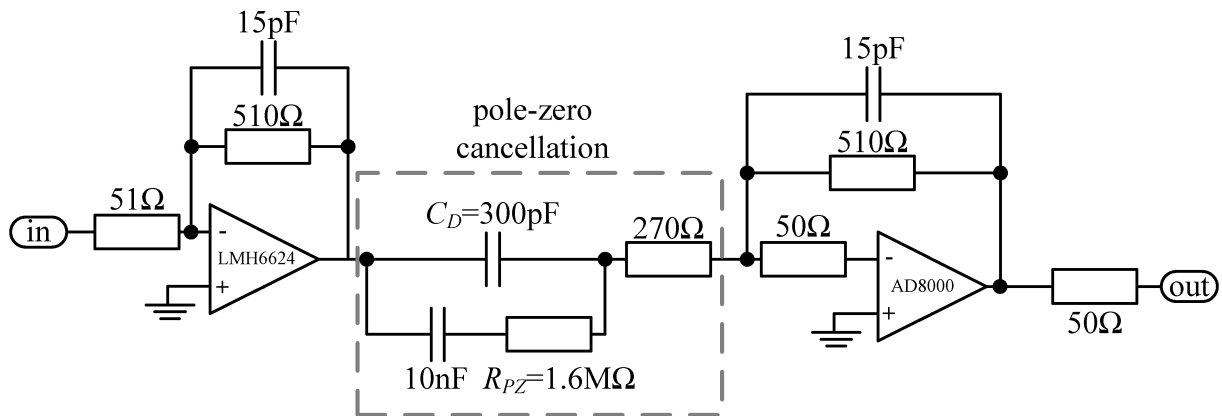


Figure 3.6: A schematic of a second stage amplifier.

Noise analysis

The noise performance of a detector readout system can be expressed as equivalent noise charge (ENC). The ENC may be defined as the ratio of the total integrated RMS (root mean square) noise at the output of the pulse shaper to the signal amplitude due to one

electron charge. It depends on the characteristic of both the charge sensitive amplifier and the pulse shaper [47].

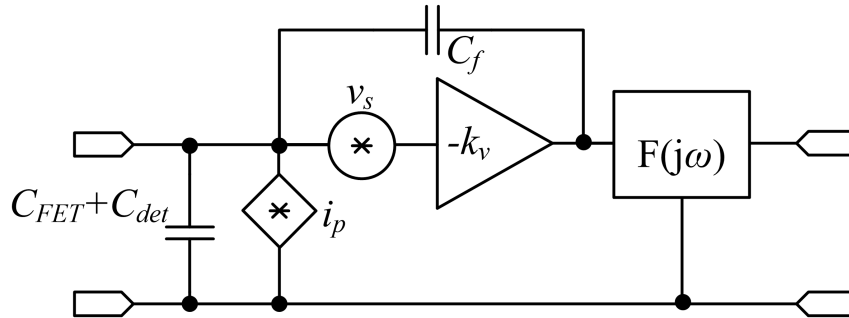


Figure 3.7: Equivalent noise scheme of the CSA.

The simplified noise model of a CSA is shown in figure 3.7. The noise performance of this system can be analysed using the equivalent input series noise source (voltage noise v_s) and input parallel noise source (current noise i_p). In the CSA, the series noise is dominated by thermal noise of the input transistor. Serial resistance of the detector R_s is also taken into account. The effect of $1/f$ noise is neglected. The formula for mean-square equivalent input voltage noise is:

$$v_s^2 = 4kT \cdot \left(\frac{0.7}{N \cdot g_m} + R_s \right) \quad (3.2)$$

where $0.7/g_m$ is equivalent noise resistance for J-FET transistors, and N is the number of input transistors. kT is the product of the Boltzmann constant, $k = 1.38 \cdot 10^{-23}$ J/K, and T is the absolute temperature in Kelvins, T . For the temperature of $T = 25^\circ\text{C} = 298$ K we assume that $4kT = 1.65 \cdot 10^{-20}$ J. The input series noise of a transistor depends on its transconductance, g_m . According to series noise, a transistor with high transconductance should be used, it is also possible to use more than one input transistor in parallel. The limitation is growing input capacitance of input transistor.

The current noise of CSA is associated with the resistance of detectors's biasing circuit R_b and the feedback resistor R_f .

$$i_p^2 = \frac{4kT}{R_f} + \frac{4kT}{R_b} \quad (3.3)$$

As it was mentioned at the beginning of this section, ENC is dependent on both noise of preamplifier and signal shaping, but also the signal readout technique should be taken into account when analysing noise performance. F. S. Goulding in [48] performed an analysis in time domain of the relative noise performance of many types of pulse-shaping systems. Knowing the front-end electronics and the method of signal collection (in this

case a gated integrator) it was possible to choose proper weights for both noises and calculate the resultant ENC of front-end electronics:

$$ENC^2 = \frac{v_s^2 \cdot C^2 \cdot N_\Delta / \tau_n}{q^2} + \frac{i_n^2 \cdot \tau_n \cdot N_s}{q^2} \quad (3.4)$$

$$C = C_{det} + N \cdot C_{FET} \quad (3.5)$$

where τ_n is the integrator's gate time, $q = 1.6 \cdot 10^{-19}$ C is the elementary charge, C_{det} is SiPM's capacitance, C_{FET} is J-FET transistor's input capacitance, N is the number of J-FETs used in CSA, N_s and N_Δ are weights for current noise and voltage noise respectively. According to [48], for shaping with RC differentiator with time constant of $\tau_{RC} = \tau_n/3$ and a gated integrator, noise constants are $N_s = 0.89$ and $N_\Delta = 1.87$.

ENC calculation

ENC calculation has been performed according to equation 3.4. First ENC calculation has been performed for one input J-FET transistor and different time of integration gate. Knowing the predicted values of dark rates, $DR = 10^5 - 10^6$ [19], the time of integration window has been set from 0 to 8 μ s. The shorter the gate time, the smaller DR influence on performed measurements.

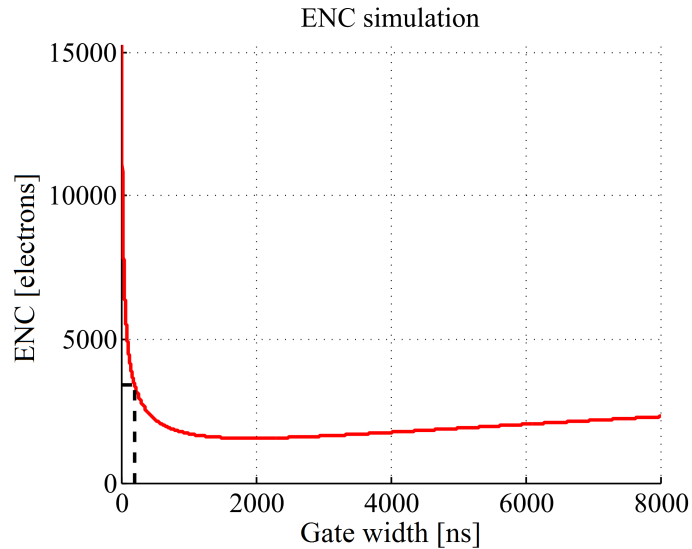


Figure 3.8: ENC calculation as a function of width of integrating gate.

Simulation of ENC in figure 3.8 shows that the minimum value of ENC can be achieved for $\tau_n = 2 \mu$ s. Knowing the predicted values for electron gain (around 10^5), expected DR and ENC simulation, it has been decided to choose integration time of 200 ns. ENC for

$\tau_n = 200$ ns expressed in elementary charges equals 3400. Assuming mean electron gain equals 10^5 , the signal to noise ratio (SNR) value can be calculated using equation 3.6.

$$SNR = \frac{GAIN}{ENC} = \frac{10^5}{3400} \approx 29 \quad (3.6)$$

After setting the integration time, the ENC simulation for different number of J-FET transistors has been performed. The resultant ENC value is influenced by the sum of thermal noise and input capacitances of a given number of J-FET transistors. The results of simulation are shown in figure 3.9.

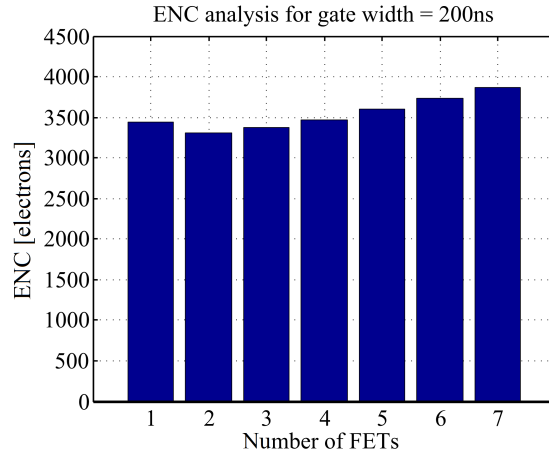


Figure 3.9: ENC calculation as a function of number of input transistors.

According to equation 3.2 the voltage noise part of ENC value is proportional to sum of input capacitances, while the level of the voltage noise is inversely proportional to transconductance of J-FET transistor. The found optimal number of J-FET transistors is 2. For higher number of transistors, the influence of rising input capacitance is higher than advantages of growing transconductance.

The final calculation of ENC for two input transistors and 200 ns integration window is presented below.

The voltage noise of CSA is:

$$v_s = \sqrt{1.65 \cdot 10^{-20} \text{J} \cdot \left(\frac{0.7}{2 \cdot 35 \text{mS}} + 40 \Omega \right)} = \sqrt{8.23 \cdot 10^{-19} \text{V}^2/\text{Hz}} = 0.91 \text{ nV}/\sqrt{\text{Hz}} \quad (3.7)$$

The current noise of CSA is:

$$i_p = \sqrt{\frac{1.65 \cdot 10^{-20} \text{J}}{10 \text{M}\Omega} + \frac{1.65 \cdot 10^{-20} \text{J}}{1 \text{M}\Omega}} = \sqrt{1.81 \cdot 10^{-26} \text{A}^2/\text{Hz}} = 0.13 \text{ pA}/\sqrt{\text{Hz}} \quad (3.8)$$

The total input capacitance is:

$$C = 170 \text{pF} + 2 \cdot 10 \text{pF} = 190 \text{pF} \quad (3.9)$$

Knowing voltage and current noise, input capacitance, integrator window length and signal shaping, ENC has been calculated according to equation 3.4:

$$ENC^2 = \frac{8.23 \cdot 10^{-19} \text{V}^2/\text{Hz} \cdot (190 \text{pF})^2 \cdot 1.87/200 \text{ns}}{(1.6 \cdot 10^{-19} \text{C})^2} + \frac{1.81 \cdot 10^{-26} \text{A}^2/\text{Hz} \cdot 200 \text{ns} \cdot 0.89}{(1.6 \cdot 10^{-19} \text{C})^2} = 1.10 \cdot 10^7 \text{electrons}^2 \quad (3.10)$$

Finally ENC is:

$$ENC \approx 3300 \text{electrons} \quad (3.11)$$

what is 100 electrons less when compared to the circuit with a single J-FET transistor.

QDC - charge to digital converter

For signal integration a QDC VME (Versa Module Europa bus) module V965A in VME8011 crate from CAEN is used. The V965A module houses 8 Charge-to-Digital Conversion channels with negative current integrating inputs (50 Ohm impedance). For each channel, the input charge is converted to voltage by a QAC (Charge to Amplitude Conversion) section. Each QAC output is then converted by two ADCs in parallel; one ADC is preceded by a $\times 1$ gain stage, the other by a $\times 8$ gain stage: a dual input range is featured: 0 – 900 pC (200 fC LSB) and 0 – 100 pC (25 fC LSB); this allows avoiding saturation with big charge pulses while increasing resolution with small ones. The ADCs use a sliding scale technique to decrease differential non-linearity. Programmable zero suppression, multi-event buffer memory, trigger counter and test features complete the flexibility of the unit [49].

The measurement system uses only one channel of the V965A. The integration time is controlled with gate signal of 200 ns generated by an Agilent 81110A pulse generator.

System calibration

The calibration of the front-end electronics (the charge amplifier and the shaping circuit) and the QDC has been performed with injecting a known amount of charge. Also the front-end electronic noise and amplifier linearity have been measured. The injector system, presented in figure 3.10, consisted of a 0.8 ns rise time pulse generator with programmable pulse height, signal attenuator and a 1% precise 20 pF capacitor connected in series.

For different values of injected charge, histograms of the output signals have been collected. Every histogram has been fitted with a Gaussian function, from which mean value and standard deviation have been calculated. To check the linearity of front-end

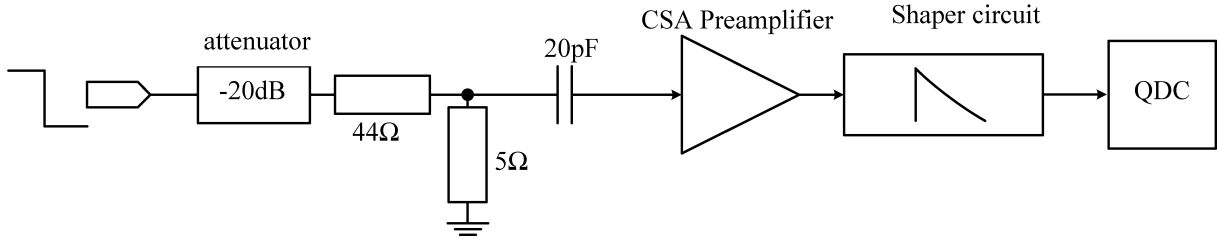


Figure 3.10: Schematic of a calibration system.

electronics, the calculated vector of histogram centres has been fitted with a linear function. The results of measurements and a linear fit function are presented in figure 3.11.

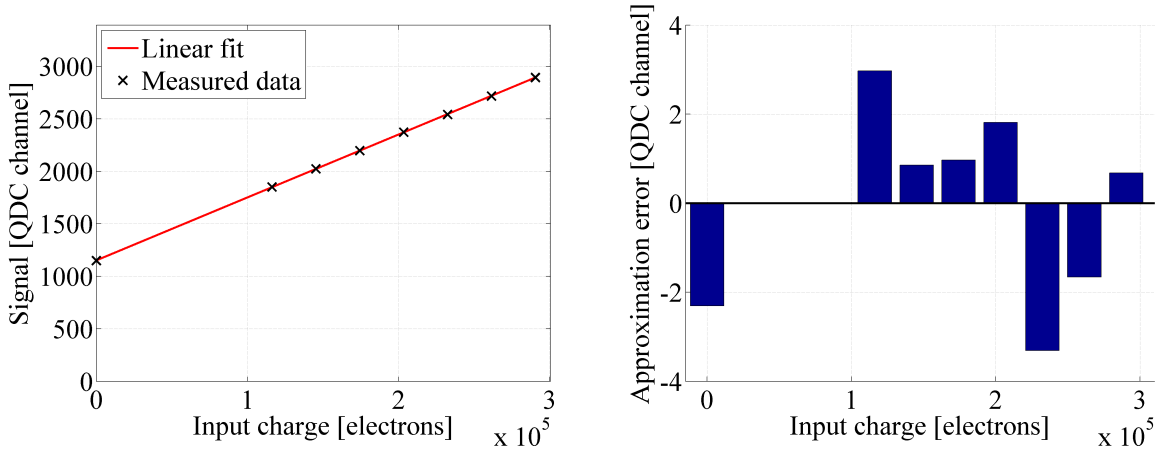


Figure 3.11: To the left: Measurement results and linear fit of system calibration procedure. To the right: Deviations of the measured values from linear approximated curve.

The measurement points fit a linear function very well. The right plot in figure 3.11 shows that approximation error is very low. From the slope of the fit function, a calibration constant can be calculated. The linear fit function of signal ($Signal[QDC\ channel]$) is presented in equation 3.12. From the slope parameter, the calibration constant has been calculated: 1 QDC channel = 167 electrons.

$$Signal[QDCchannel] = 5.99 \cdot 10^{-3} \cdot \text{electrons} + 1149 \quad (3.12)$$

Noise measurement

Knowing the calibration constant (1 QDC channel = 167 electrons) and having a histogram of signal pedestal, it is possible to measure the ENC of the front-end electronics.

As it can be seen in figure 3.12, recorded histogram of a pedestal signal has been fitted with Gaussian function. The Gauss fit function can be described as follows:

$$COUNT = 1656 \cdot \exp\left(-\frac{(Signal[QDC] - 1149)^2}{2 \cdot 24.08^2}\right) \quad (3.13)$$

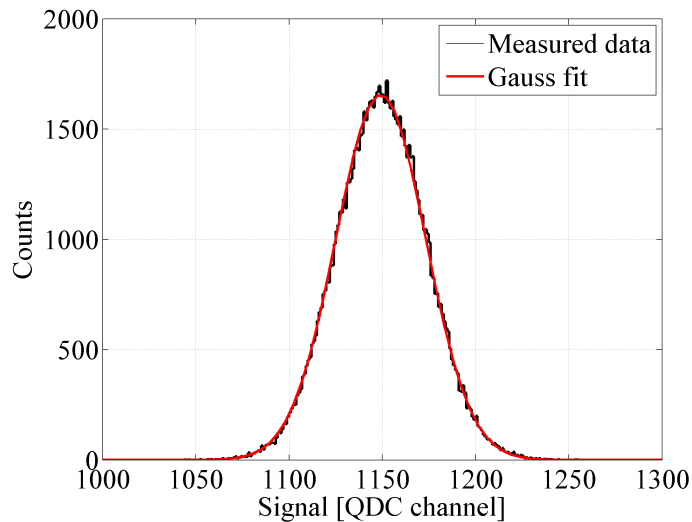


Figure 3.12: Results of system calibration - noise fit of pedestal peak.

The mean value of pedestal peak is 1149 QDC channels. The standard deviation of calculated Gaussian fit function is $\sigma = 24.08$ QDC channels what is 4008 electrons of ENC input noise. The ENC value is higher than the predicted value, which was calculated at the beginning of this chapter. The reason of this difference may be due to additional $1/f$ noise which was neglected and the method which was used for noise calculation in section 3.2.

Summary

The simplified schematic of front-end and the data acquisition system is presented in figure 3.13. The measurements are controlled by a Matlab program running on a PC computer. Signal from SiPM detector is amplified with a low noise charge preamplifier and shaped with a second stage circuit (pole-zero cancellation). Amplified and shaped signal can be read out by a charge to digital converter (QDC) or sampled with an oscilloscope. The bias voltage for SiPM is set with a remotely controlled power supply. Trigger signal for the QDC and the oscilloscope are generated with a pulse generator.

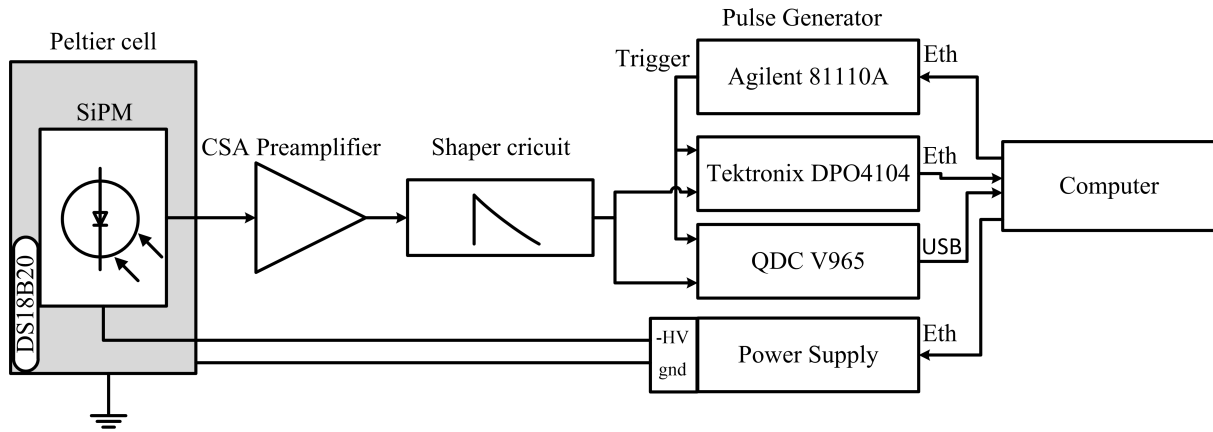


Figure 3.13: Simplified schematic of a front-end electronics and data acquisition system for histogram based measurements.

3.3 Front-end for signal shape measurements

Measurement of signal shape requires usage of fast front-end electronics and analogue to digital converter. For this purpose a wide-bandwidth amplifier was designed. Tektonix DPO4104 oscilloscope was used for signal acquisition. The oscilloscope has 1 GHz bandwidth with 4 analog channels. The maximum sampling rate is up to 5 GS/s on all channels. DPO4104 offers a deep record length of 10^7 points on all channels. It can be remotely controlled via Ethernet connection. Signal acquisition is triggered with Agilent 81110A pulse generator.

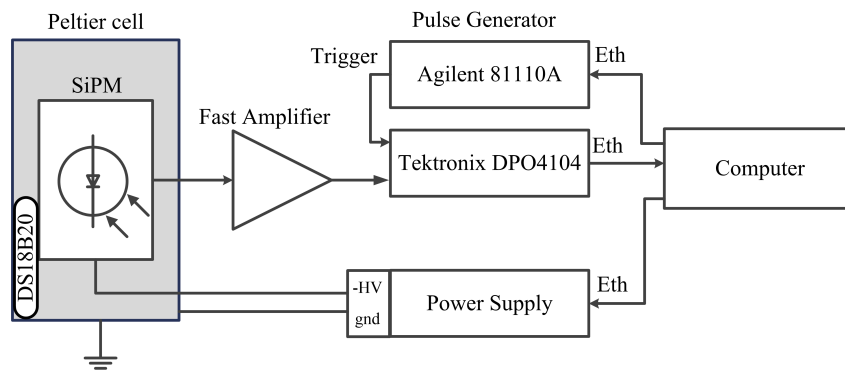


Figure 3.14: Simplified schematic of the front-end electronics and data acquisition system for signal shape measurements.

Fast amplifier

The front-end electronics is realized with a high speed, current feedback amplifier AD8000. The amplifier can achieve unity-gain bandwidth of 1.5 GHz and slew rate of $4100 \text{ V}/\mu\text{s}$.

Input voltage noise of AD8000 is $1.6 \text{ nV}/\sqrt{\text{Hz}}$. The amplifier is configured as a voltage follower in order to keep the bandwidth as high as possible. The advantage of using the AD8000 is also its small input capacitance 3.6 pC .

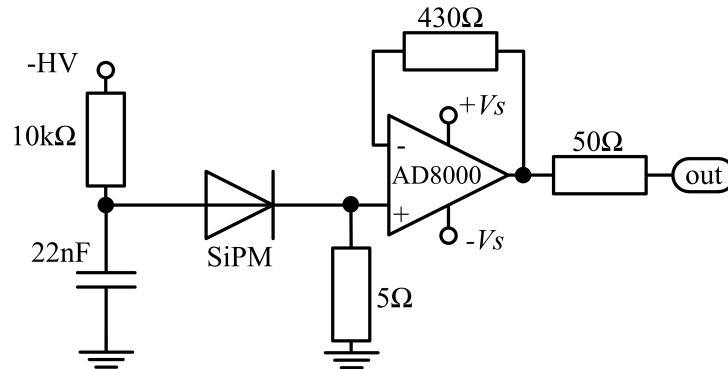


Figure 3.15: Schematic of the fast amplifier.

Figure 3.15 shows the schematic of the fast amplifier. The current generated by SiPM detector causes voltage drop on 5Ω resistor. The voltage drop is then passed to the input of the voltage follower. The 3 dB bandwidth of AD8000 for the voltage follower configuration is 980 MHz.

3.4 Temperature control system

Temperature control system is realized with a proportional-integral (PI) controller running as a Matlab program. A schematic of the temperature control system is shown in figure 3.16.

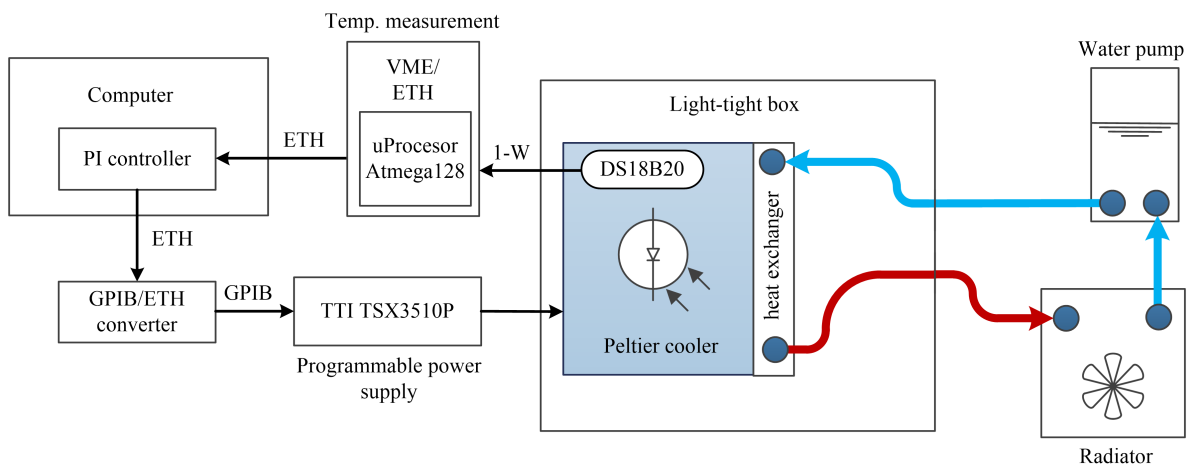


Figure 3.16: Schematic of the temperature control system.

The SiPM detector is placed on a aluminium thermostabilizer plate which is cooled with a 50 W Peltier cell. Temperature of the detector is measured with a DS18B20 digital thermometer. DS18B20 provides temperature measurements with 12-bit resolution and is scaled in Celsius degrees. It communicates over a 1-Wire bus with an Atmega microprocessor, which sends data to a computer. Voltage of the Peltier cell is set with a programmable power supply - TTI TSX3510P controlled via Ethernet connection. Heat from the Peltier cell is transferred outside the lightproof box with a Magicool MC-G12V1 water cooling system, which is a DIY (do it yourself) liquid cooling kit designed for PC microprocessors. The kit consists of a heat exchanger (attached to the hot side of the Peltier cell), a water pump and a radiator with a fan. The system allows controlling the temperature of the detector in range from 0°C to 25°C with an accuracy of 0.5°C. However, when the detector was cooled to the temperature below the dew point, due to a humidity inside the light-tight box the surface of the detector was covered with water drops.

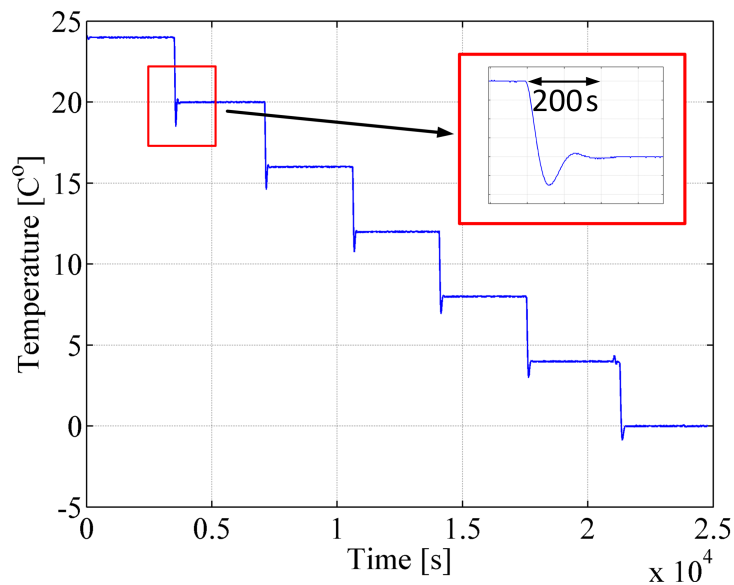


Figure 3.17: The plot of temperature during the SiPM measurement. Measurement was performed for 7 different temperatures. Zoomed picture shows the part of the plot with temperature change from 24°C to 20°C.

The PI controlled has been tuned with Ziegler-Nichols Method [50]. Figure 3.17 shows the temperature plot during the SiPM measurement. The measurement was performed in 7 different temperatures from 24°C to 0°C with a step of 4°C. The measurement started with a stable temperature of 24 V, after a period of 3500 s the temperature has been switched to 20°C. The zoomed part of the plot shows the point of temperature

change. As it can be seen the PI controlled is well tuned. The controller response is fast, a small overshoot is visible but after around 200s the temperature gets stable again.

3.5 Light source and positioning system

The measurement of uniformity of parameters (spacial distribution) requires a special system for positioning and focusing a light spot on surface of the detector. A special system for light positioning has been developed; a schematic of the system is presented in figure 3.18. The device consists of an electrical system and three stepper motors. Stepper motors (Thorlabs ZST213b) drive a micrometer block (Thorlabs RB13M) with a collimator and a microfocus lens mounted on top. The controller can set the position of the micrometer block in 3 directions in range of 13mm with a step of 1 μm . The system allows obtaining a 3 μm spot on the surface of the detector. A picosecond laser controller EIG2000DX with two laser diode modules with wavelength of 370 nm and 440 nm is used as a light source. The EIG2000DX controller can produce light pulses with 60 ps pulse width and maximum repetition rate of 40 MHz.

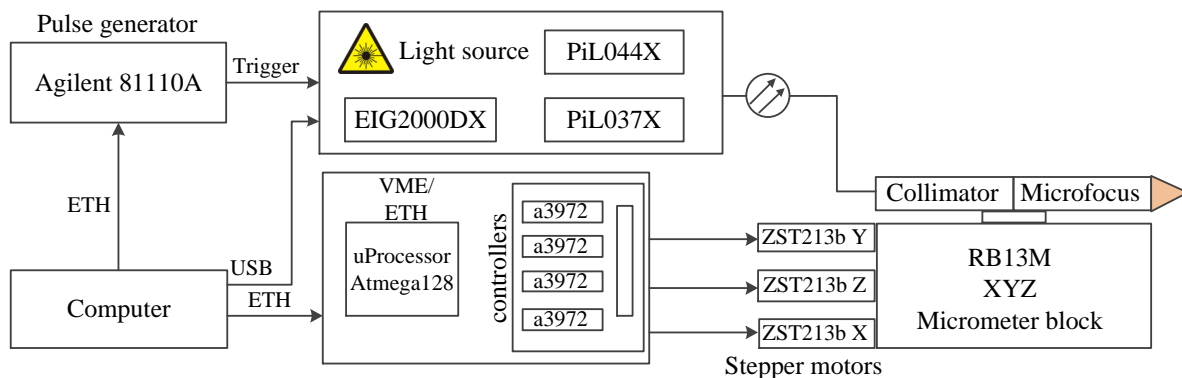


Figure 3.18: Schematic of a light source and light spot positioning system.

A custom made stepper motor controller is connected with a computer via Ethernet interface. A program developed in Matlab environment communicates with both the light source and the positioning system. For the light source, it is possible to set both light level and pulse frequency. The laser controller is triggered with a pulse generator (Agilent 81110A) which also starts the signal conversion of the DAQ system. The positioning system needs to be calibrated before setting the position of the micro focus lens.

Light spot positioning system tests

During the scan in XY directions, the size of the light spot on the surface of the detector cannot be monitored. Before each scan, a light focusing procedure has to be performed. The signal from a measured SiPM detector is used in light spot focusing procedure. To find a focal position of microfocus lens, signal amplitude measurement as the function of distance between the lens and the surface of the SiPM detector has to be performed. The global minimum of the measured curve is the distance at which the size of the light spot on the surface of the detector is the smallest. Unfortunately, with this measurement, only the mean number of fired pixels can be measured.

The achievable spot size is determined by the focal length ratio (micro-focus / collimator) and by the mode field diameter of the singlemode fibre. To a good approximation, the spot size is given by:

$$\varnothing = \frac{f'_{micro-focus}}{f'_{collimator}} \cdot MFD \quad (3.14)$$

Optical system consists of:

- 460HP single mode optical fibre with the mode field diameter $MFD = 3.5 \mu\text{m}$
- Fibre collimator 60FC-0-A11-01 with focal length $f' = 11 \text{ mm}$
- Microfocus lens 5M-A4-01-S with focal length $f' = 4 \text{ mm}$

The theoretical spot size of the system is given by:

$$\varnothing = \frac{f'_{micro-focus}}{f'_{collimator}} \cdot MFD = \frac{4 \text{ mm}}{11 \text{ mm}} \cdot 3.5 \mu\text{m} = 1.27 \mu\text{m} \quad (3.15)$$

The spot size of $1.27 \mu\text{m}$ should be small enough to scan individual pixels of SiPM detectors with pixel size around $10 \mu\text{m} \times 10 \mu\text{m}$. A measurement system consisting of a CCD (Charge Coupled Device) array has been set to measure the profile and the size of the light spot on the surface of the detector. For this purpose, a camera module for Raspberry Pi computer has been used, which is equipped with 5 Megapixels OmniVision CCD matrix. The camera with removed optics has been placed instead of the SiPM detector. The pixel size of the matrix is $1.4 \mu\text{m}$ what is enough to check the light beam profile. The measurement was performed with a stable light intensity while changing distance between the microfocus lens and the CCD matrix. A photo of light beam profile has been taken for every position of the microfocus lens. The example data from CCD matrix is presented in the bottom picture of figure 3.19. Every picture has been fitted with two-dimensional Gaussian function from which the FWHM has been taken.

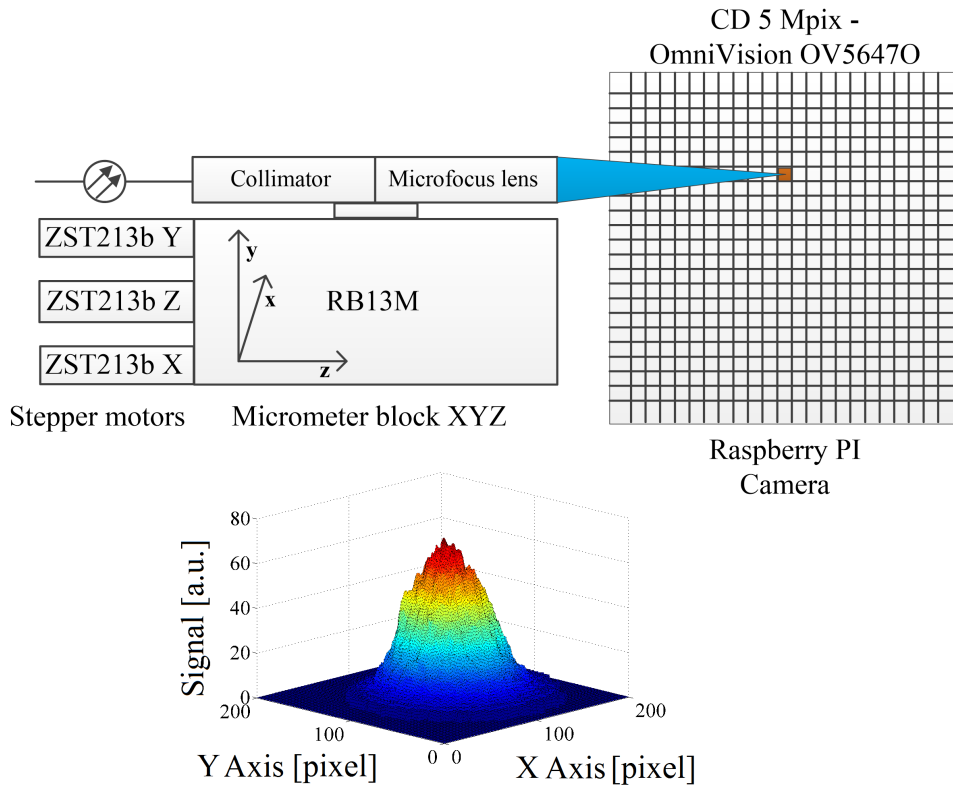


Figure 3.19: A schematic view of micro-focus lens tests with OmniVision CCD camera. On the bottom: the example picture of laser beam profile taken with CCD camera.

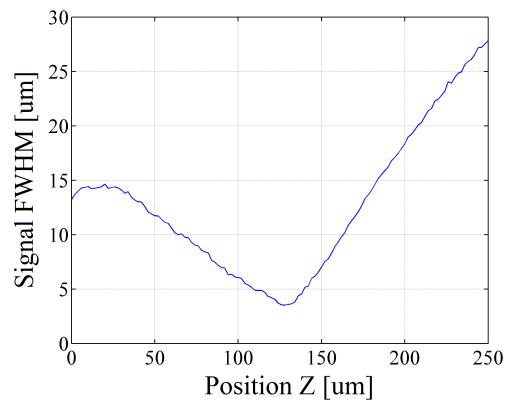
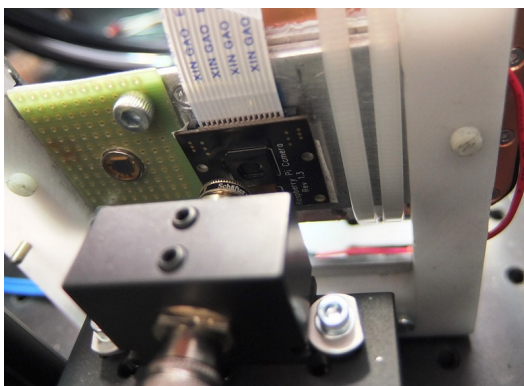


Figure 3.20: To the left: A photo of laser focus lens tests with CCD camera. To the right: result of laser spot width measurement.

The plot in figure 3.20 shows the results of laser spot width measurement as the function of the lens position. Position $Z = 0 \mu\text{m}$ is the closest possible position between the housing of the CCD matrix and the microfocus lens. The best light beam focus on the surface of the CCD matrix has been reached for position $Z = 128 \mu\text{m}$, the spot size in this position is $\varnothing = 3.5 \mu\text{m}$. This size is almost 3 times bigger than the theoretical

one, but still should be small enough to illuminate single pixels of SiPM detectors. The strange behaviour of light spot size at the beginning is the result of the Thorlabs stepper motor backlash which is around $25\ \mu\text{m}$.

Chapter 4

SiPM measurement results

Both detectors: MAPD from Zecotek and MPPC S12572-010 from Hamamatsu have been measured. Due to different quenching mechanism, a novel MAPD detector is more interesting and has been measured more accurately. Much attention has been paid to terminal capacitance and recovery time measurement of the MAPD-3N.

4.1 Electrical measurements

To calculate the values of electrical model of the MAPD, one detector sample has been measured with with a vector analyser. This measurement allowed to calculate terminal capacitance and resistance of the MAPD. Also an additional capacitance measurement for different biasing voltages with RLC meter has been performed.

Impedance measurement of MAPD

During the impedance measurement, the diode has been biased just below the breakdown voltage (80 V), in order to obtain full depletion of the p-n junction. The impedance has been measured for frequencies in range of 1 MHz – 1 GHz. The values of resistance and capacitance have been calculated from impedance results. Results and fitting curves have been shown in figure 4.1. The electrical model consists of depletion region capacitance C_{dep} , serial resistance R_s and small parasitic capacitance C_g .

As it can be seen in figure 4.1, the simulation for the proposed impedance model fits measurement data quite well for moderate frequencies. $C_{dep} = 154$ pF is the capacitance of a fully depleted pn junction where charge multiplication occurs. The capacitance is defined as the incremental increase in charge dQ upon an incremental change in applied voltage dU [51], $C = dQ/dU$. The C_{dep} capacitance depends on the depletion layer

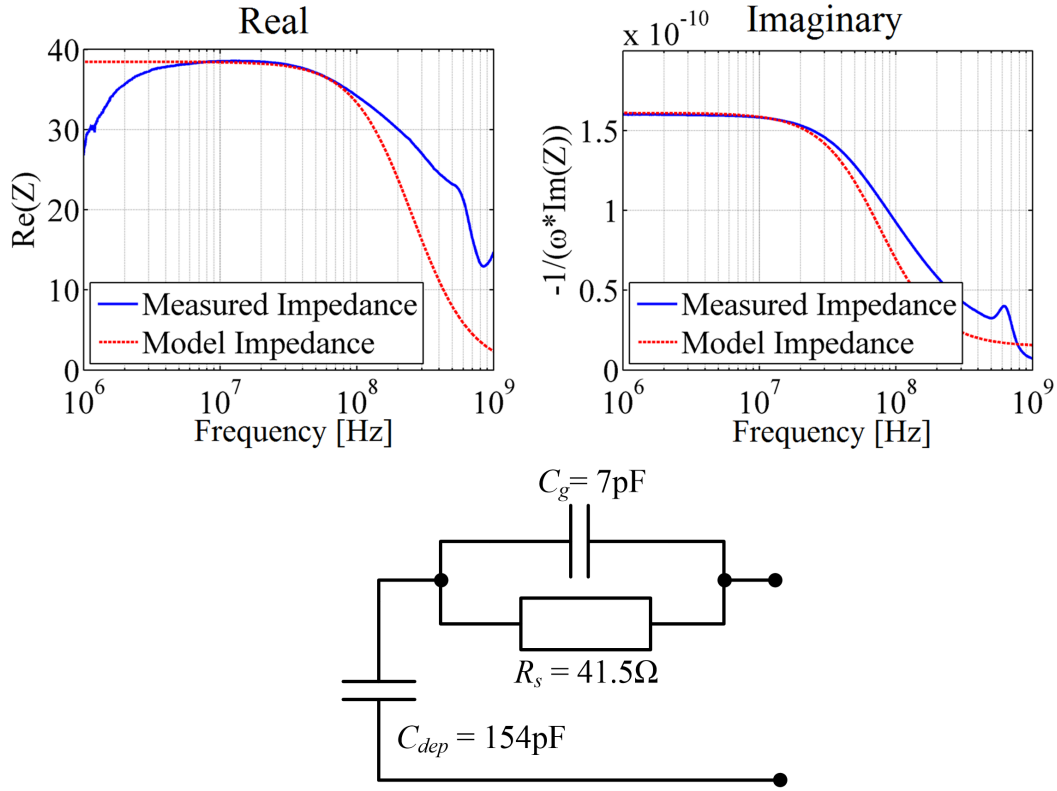


Figure 4.1: Top: Measurement data and simulation results of MAPD-3N terminal impedance. Bottom: Model of simulated terminal impedance: C_{dep} is the depletion layer capacitance, R_s serial resistance of the p+ contact layer and C_g parasitic capacitance.

thickness and it is the same as that of a parallel plate capacitor of width equal to the depletion width [52] as in equation 4.1:

$$C_{dep} = \frac{dQ}{dU} = \frac{\epsilon_r \epsilon_0 A}{w} \quad (4.1)$$

where $\epsilon_r = 11.7$ is the relative permittivity of silicon, $\epsilon_0 = 8.85 \text{ pF/m}$ is the vacuum permittivity, A is the devices's area and w is the thickness of the depletion layer. Knowing the MAPD surface area $A = 9 \text{ mm}^2$ and $C_{dep} = 154 \text{ pF}$, it is possible to calculate the thickness of the depletion layer at voltage of 80 V:

$$w = \frac{\epsilon_r \epsilon_0 A}{C_{dep}} = \frac{11.7 \cdot 8.85 \text{ pF/m} \cdot 9 \text{ mm}^2}{154 \text{ pF}} = 6.1 \cdot 10^{-6} \text{ m} = 6.1 \text{ } \mu\text{m} \quad (4.2)$$

Terminal capacitance measurement

Since the thickness of the depletion region is dependent on the applied reverse voltage, the measurement of terminal capacitance for different reverse voltages, can be used to

find out at what voltage the p-n junction is fully depleted, i.e. find the depletion voltage (V_d). The measurement of MAPD terminal capacitance has been performed with RLC meter ELC-3131D at a frequency 1 kHz. The device has been biased with 100 k Ω resistor in series.

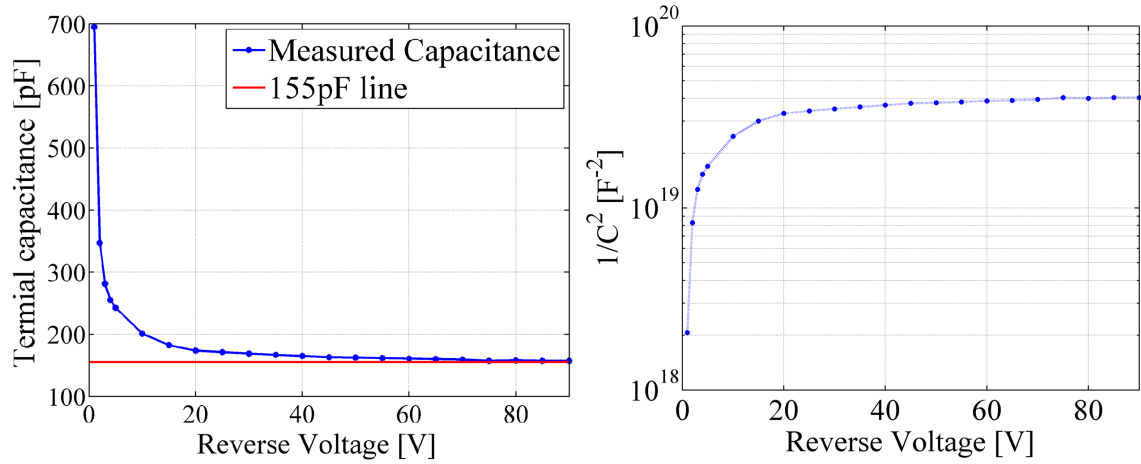


Figure 4.2: MAPD terminal capacitance measurement: Left: MAPD-3N terminal capacitance as a function of the bias voltage; Right: the $1/C^2$ versus bias voltage curve.

For a diode consisting of one-sided abrupt junction with uniform doping and constant area, the thickness of depletion layer below the depletion voltage is proportional to square root of the operating voltage. For voltages higher than depletion voltage, the depletion thickness should be constant:

$$w = x_p + x_n = \sqrt{\frac{2\epsilon_r\epsilon_0(V_{op} + V_{bi})}{q} \cdot \left(\frac{1}{N_A} + \frac{1}{N_D}\right)} \quad (4.3)$$

where N_D and N_A are the number of ionized donors and acceptors, $q = 1.6 \cdot 10^{-19}$ C is the elementary charge, V_{bi} is the built-in voltage and V_{op} is the applied bias voltage. Looking at equations 4.1 and 4.3, the dependency $1/C^2$ on the bias voltage is expected to be linear until the depletion voltage is reached. As it can be seen in figure 4.2, the capacitance dependency on voltage is more complicated and there is no clear point where depletion voltage is reached. The determination of the depletion voltage obtained from extrapolation of the $1/C^2$ curve is not possible. $1/C^2$ curve has at least four different slopes for voltages in ranges: 0 to 3V, 3 to 10V, 10 to 20V and 20 to 90V. Similar capacitance measurements have been conducted by E.A. Jafarova, Z.Y. Sadygov (the inventor of MAPD detector) et al. in 2016 [53]. The equivalent circuit of the MAPD micro-pixel is a complex connection of three p-n junctions, therefore it is difficult to clearly explain the contributions of each in total measured capacitance [53]. According to

capacitance measurement and equation 4.2, the width of depletion layer as a function of applied reverse voltage has been calculated.

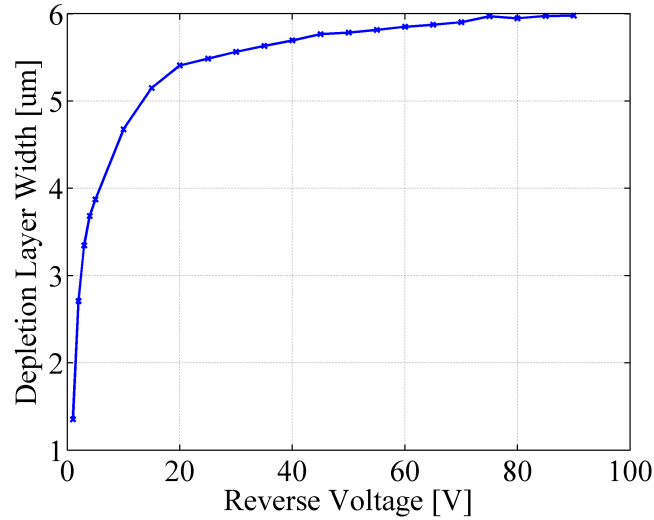


Figure 4.3: Dependence of the width of the depletion layer of MAPD-3N detector on the supply voltage.

Figure 4.3 shows the dependence of depletion layer width on the supply voltage. As it can be seen, the width of depletion layer increases sharply from 1 μm to 3 μm for voltages in range 1 to 3 V. At relatively high voltage of 20 V it reaches 5.5 μm . For voltages 20 to 90 V, the width grows very slowly and reaches 6 μm .

4.2 Histogram based measurements

Very small differences in electron gain between pixels of SiPM detectors allows to use a unique method of measuring many parameters of the detector based on recording signal amplitude histogram with low light levels (several photons). However, several conditions must be fulfilled. The temperature of the detector must be well stabilized in order to keep stable gain value. Also the noise of amplifiers must be much lower than predicted electron gain of detector under tests for clear separation of histogram peaks. Another condition is use of a stable light source with short pulse width. Two types of histogram based measurements can be distinguished:

1. Dark measurements — these measurements are performed without incident light, in result only dark and correlated noise pulses are recorded. Recorded histogram can be used for DR (dark rate) calculation and electron gain measurements.

- Light measurements — for this measurement, a well stabilized light source is needed. A detector is illuminated with short and relatively weak light pulses. From a histogram, many parameters can be calculated: electron gain, relative PDE , correlated noise and breakdown voltage.

The histogram based measurements were performed with several samples of MAPD-3N detector. Measurements were performed as both dark and light measurements. For the light measurements, light beam was positioned to illuminate the whole surface of the detector.

Histogram collection

For certain operating conditions: operating voltage, temperature, light pulse repetition frequency (PRF) and number of incidents photons, a number of response integrals is recorded. As it can be seen in figure 4.4a, signals from different number of fired pixels are clearly distinguishable even on an oscilloscope. The blue curve is the gate which was used for signal integration. Figure 4.4b shows the sample histogram. From a single histogram, a set of parameters can be calculated: electron gain, correlated noise, dark noise, mean number of fired pixels. By measuring these parameters in different conditions (operating voltage and temperature), it is possible to calculate parameter dependencies on the operating voltage and temperature. Most of histogram based measurements have been performed with low light level (several incident photons) and pulse repetition frequency of 100 kHz.

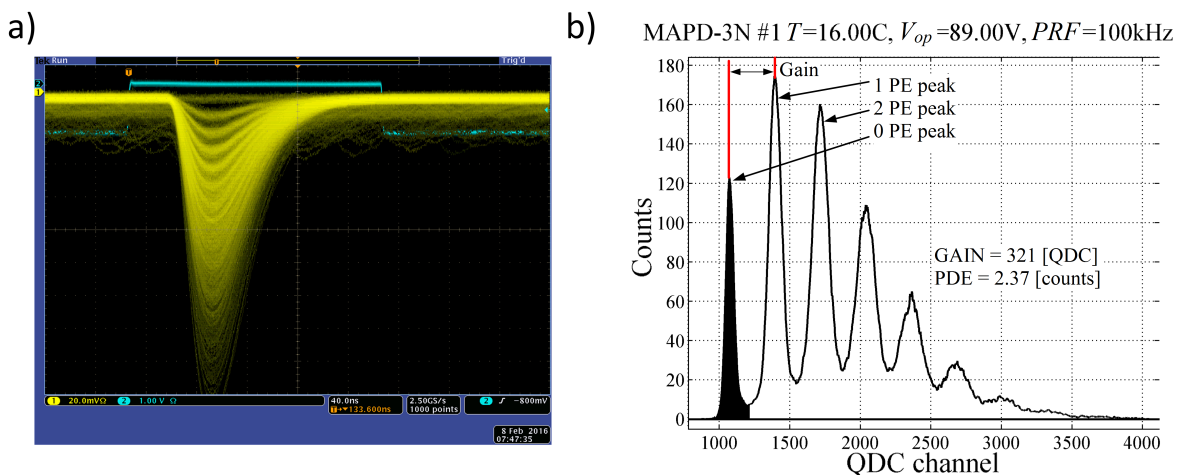


Figure 4.4: The MAPD histogram measurement; a) MAPD signal responses for a low light level pulses b) sample MAPD signal response histogram, 0 PE peak coloured in black.

Gain and breakdown voltage

The aim of this measurement is to determine the electron gain as a function of operating voltage for a given temperature. Electron gain of the SiPM detector is defined as the number of carriers produced in a single avalanche. The gain is dependent on the pixel capacitance and the applied overvoltage and can be calculated using the distance between the histogram peaks. Before determining the positions of individual peaks, each histogram is convolved with Gaussian filter in order to smooth the measurement data.

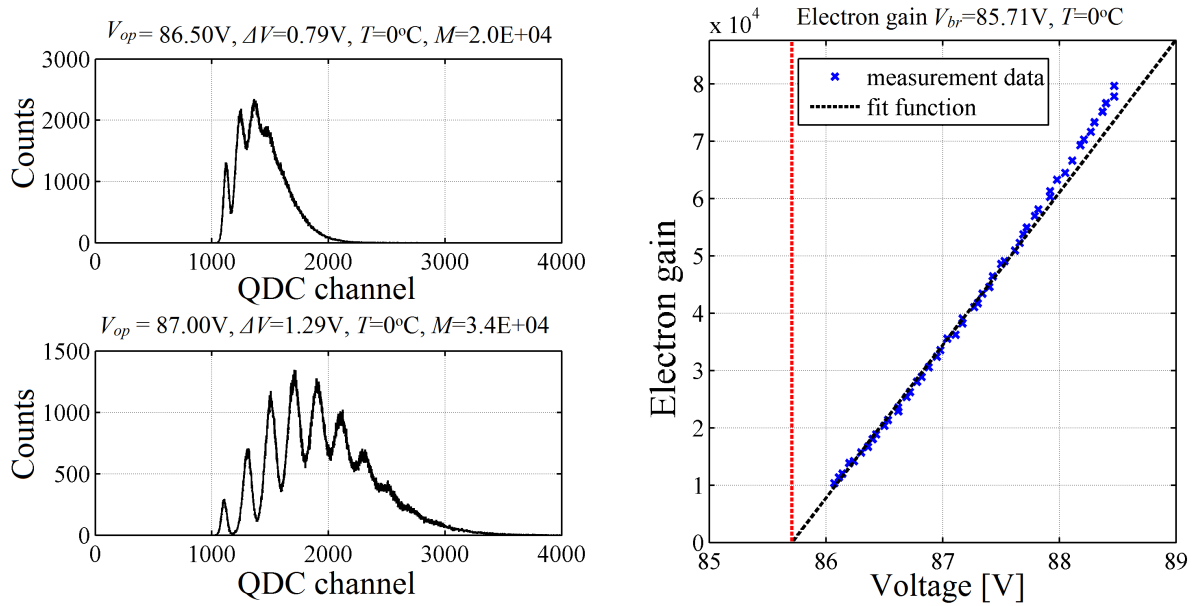


Figure 4.5: Results of gain measurements with low light pulses at temperature 0°C. To the left: histograms for two different operating voltages. To the right: electron gain for different operating voltages (V_{op}) and gain fit function.

Measurements of the electron gain at stable temperature for at least two different operating voltages can be used to calculate the breakdown voltage (V_{br}) at which the Geiger mode multiplication starts. This allows to express the measured parameters as a function of overvoltage (ΔV), like in equation 4.4:

$$M(\Delta V) = \Delta V \cdot C_{pix} \quad (4.4)$$

where C_{pix} is the capacitance of a single pixel. The overvoltage is the operating voltage above the breakdown voltage:

$$\Delta V = V_{op} - V_{br} \quad (4.5)$$

For a known breakdown voltage at a given temperature, electron gain can be expressed as a function of operating voltage and temperature:

$$M(V_{op}, T) = (V_{op} - V_{br}(T)) \cdot C_{pix} \quad (4.6)$$

As it can be seen in figure 4.5, a set of measurements of electron gain for various operating voltages at temperature 0 °C for MAPD-3N was performed. A point where extrapolated, function of gain reaches zero is the breakdown voltage for a given temperature. The fit function from figure 4.5 gives the information of breakdown voltage V_{br} (85.71 V) for temperature of 0 °C and the pixel capacitance C_{pix} (4.26 fF). The electron gain of the detector for temperature of 0 °C can be expressed as:

$$M(V_{op}, 0^\circ\text{C}) = \frac{(V_{op} - 85.71 \text{ V}) \cdot 4.26 \text{ fF}}{q} \quad (4.7)$$

where $q = 1.6 \cdot 10^{-19} \text{ C}$ is the elementary charge.

The breakdown voltage of a SiPM detector is dependent on the temperature. It is expected that the breakdown voltage decreases with decreasing temperature [54]. At lower temperature, the carrier mobility is larger, thus ionisation rates for constant electrical field are also larger, what leads to lower value of the breakdown voltage. Knowing the breakdown voltage for a set of temperatures, it is possible to calculate the breakdown voltage temperature coefficient ΔV_{brt} . Knowing the breakdown voltage for one temperature and its temperature coefficient, it is possible to calculate the breakdown voltage for any temperature.

$$V_{br}(T) = V_{br}(0^\circ\text{C}) + (0^\circ\text{C} + T) \cdot \Delta V_{brt} \quad (4.8)$$

Now the electron gain, which is the function of the operating voltage and the temperature, can be expressed as:

$$M(V_{op}, T) = \frac{\Delta V \cdot C_{pix}}{q} = \frac{(V_{op} - (V_{br0} + T \cdot \Delta V_{brt})) \cdot C_{pix}}{q} \quad (4.9)$$

where V_{br0} is the breakdown voltage for temperature 0 °C, $\Delta V_{brt}[\text{V}/^\circ\text{C}]$ is the breakdown voltage temperature coefficient and C_{pix} is the capacitance of a single pixel. Knowing electron gain for different temperatures and operating voltages it is possible to find the values of these three parameters. The measurement of the electron gain for temperatures in range from 0 °C to 24 °C and operating voltages from 86 V to 90.5 V has been performed for MAPD-3N detector. For each setting a histogram of 1 million samples has been recorded and analysed.

The electron gain data has been plotted (see figure 4.6) and fitted with function 4.9. The method of minimizing the sum of squares of the residuals of the measurement points

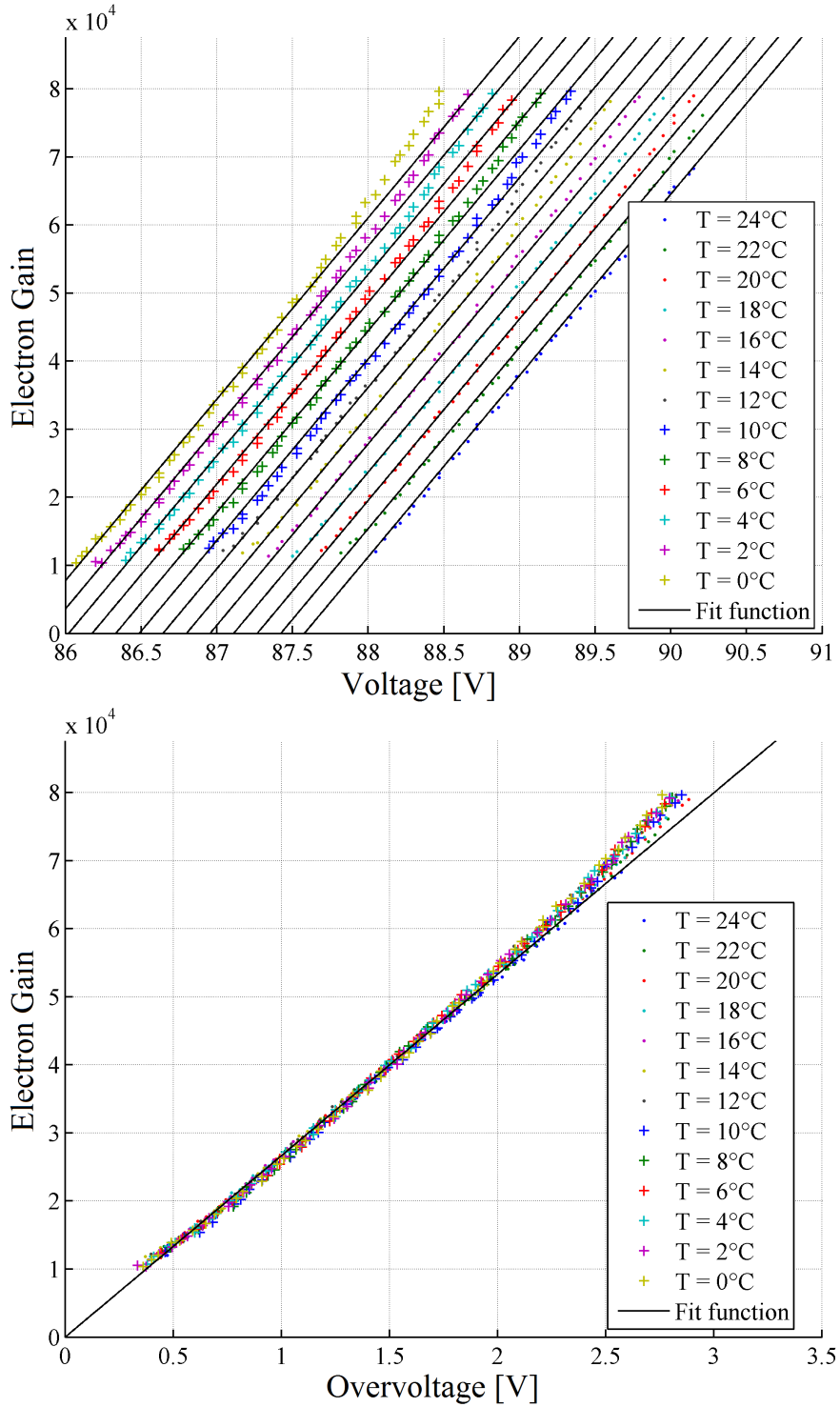


Figure 4.6: Results of MAPD-3N gain measurements for different temperatures with low level light pulses. Top: results of gain calculation as a function of operating voltage for different temperatures, solid lines represent the global fit function for gain. Bottom: The same gain measurements as a function of the overvoltage.

from the fit curve has been used to find the values of the parameters for the fit function. The best fit has been obtained for the following parameters:

- $V_{br0} = 85.708 \pm 0.004 \text{ V}$
- $\Delta V_{brt} = 77.90 \pm 0.17 \text{ mV}/^\circ\text{C}$
- $C_{pix} = 4.264 \pm 0.011 \text{ fF}$

For measured sample of MAPD-3N detector, the electron gain function can be expressed as:

$$M(V_{op}, T) = \frac{(V_{op} - (85.71 \text{ V} + T \cdot 78 \text{ mV}/^\circ\text{C})) \cdot 4.26 \text{ fF}}{1.6 \cdot 10^{-19} \text{ C}} \quad (4.10)$$

As it can be seen in the top plot in figure 4.6, measurement points fit well to electron gain function for reasonable overvoltages. The bottom plot in figure 4.6 shows gain measurement data as a function of the overvoltage for various temperatures. Measurement data are close to linear fit, what means that breakdown voltage temperature coefficient is well defined. For the overvoltage above 2.5 V, measurement data bends upward, this is caused by correlated noise (especially afterpulses) which introduces a hard to compensate systematic error to gain measurement.

Samples comparison

The electron gain and breakdown voltage measurement has been performed for nine samples of the MAPD-3N detector. The aim of this measurement was to determine the differences of these parameters between samples.

Table 4.1: Zecotek MAPD parameters comparison for nine samples

Detector sample	C_{pix} [fF]	V_{br0} [V]	ΔV_{brt} [mV/ $^\circ\text{C}$]
1	4.405	85.261	78.20
2	4.313	85.601	77.23
3	4.264	85.708	77.90
4	4.355	85.727	82.06
5	4.299	85.498	83.19
6	4.366	85.413	84.26
7	4.405	85.502	81.35
8	4.475	85.421	83.12
9	4.317	85.463	81.37
mean	4.355	85.51	80.96
SD/mean	1.41 %	0.14 %	3.00 %

As it can be seen in table 4.1, the pixel capacitances and breakdown voltages of measured detectors are very similar, the standard deviations of these parameters are 1.41 % and 0.14 %. Surprisingly the standard deviation of breakdown voltage temperature coefficient is only 3.00 %, this may be result of small number of measured detectors and the fact that they were mostly probably carefully selected by the manufacturer.

The mean pixel capacitance fits the results of terminal capacitance of the detector. For capacitance calculation from gain measurement, two capacitors $C1$ and $C2$ from fig. 2.10 are connected in parallel. On the other hand, RLC meter measures series connection of $C1$ and $C2$ capacitors. In result, measurement based on electron gain should give result four times higher (see equation 2.12). According to equation 2.13, the terminal capacitance of MAPD-3N should be:

$$C_{terminal} = 135000 \cdot 4.355 \text{ fF}/4 + 5 \text{ pF} = 152 \text{ pF} \quad (4.11)$$

which is very close to terminal capacitance (154 pF) measured with the RLC meter and vector analyser in section 4.1. This proves that n+ microwells are in the middle of the epitaxial layer, in result capacitors $C1$ and $C2$ have the same value.

Correlated noise

For calculation of CT+AP fraction, histograms obtained from measurements using low-level light pulses for various overvoltages are used – the theoretical Poisson distribution is compared with the measured one. The ratio of 1 PE (photoelectron) counts from the real histogram to the same number obtained from the theoretical one gives the probability of a CT+AP event.

As it can be seen in figure 4.7, CT+AP noise has been measured and plotted as a function of the overvoltage for different temperatures. The right plot shows the measurement method. The red bars show the theoretical Poisson distribution based on the pedestal peak and the total number of events. The mean number of fired pixels is 1.76. The orange bars show the real distribution of fired pixels. As it can be seen, 1 PE and 2 PE peaks are lower than in theoretical Poisson distribution, while the others are higher. This is the effect of the correlated noise. The left plot shows the correlated noise dependency on temperature and overvoltage. As it was noticed in [14], CT+AP noise is not dependent on temperature. The dependency on the overvoltage is more complicated, for overvoltages from 1 V to 2.3 V the noise maintains at low level, below 5 %. Above 2.3 V the noise increases steeply and linearly to the applied voltage. The correlated noise limits the performance of the detector for growing overvoltage. Due to a limited overvoltage range (to 2.3 V), achievable electron gain and PDE are also limited.

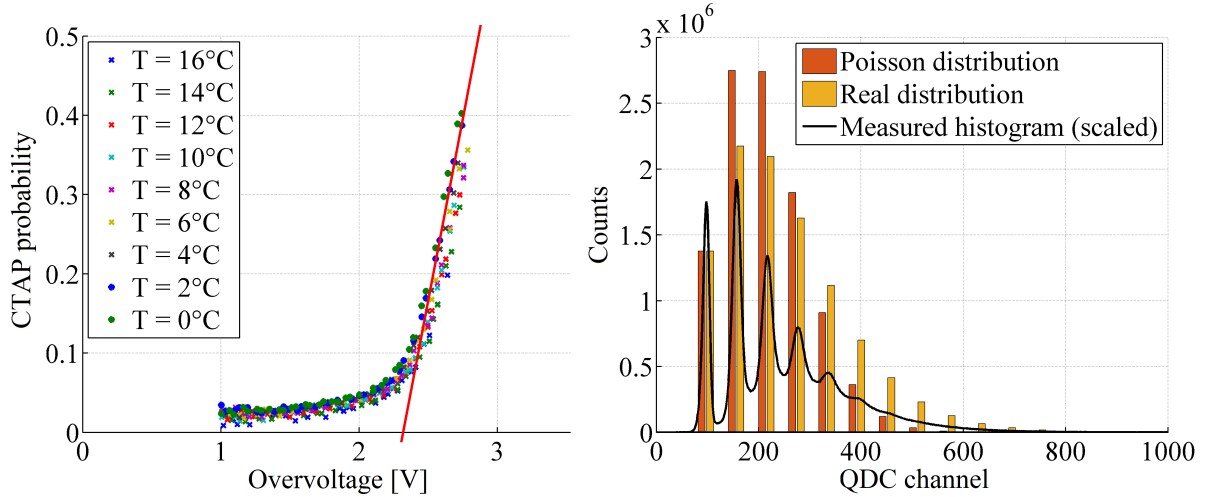


Figure 4.7: Results of correlated noise measurements: to the left: Correlated noise probability as a function of the overvoltage for temperatures in range 0°C - 12°C. To the right: example of correlated noise measurement for $V_{op} = 88.5$ V, $T = 0^\circ\text{C}$, $\Delta V = 2.4$ V. The mean number of fired pixels is 1.76.

Dark noise measurement

Two techniques were used for calculation of the dark noise of the MAPD detector. The first technique was based on histogram measurements. The second one was based on the distribution of the time intervals between consecutive dark pulses.

Histogram based measurement

The histogram based method with no incident light was used for calculation of the dark rate. In these measurements, the position of the pulse is not correlated with the position of the integrating gate, some part of recorded pulses are partially integrated, thus peaks of the histogram are wider. However the gain values should be the same as the ones obtained from measurements with low level light pulses.

The left plot in figure 4.8 shows the gain calculated for different temperatures as a function of the operating voltage. Surprisingly, gain values obtained with dark pulses varies from the one recorded with incident light. As it can be seen on the right plot in figure 4.8, the gain values for dark measurements are lower by a constant value regardless the applied overvoltage. This fact does not influence the dark rate calculation, but it is very interesting and will be investigated in another section.

Dark rate measurement technique Histograms of amplitudes of dark pulses should have a Poisson distribution. The data were collected for different temperatures and over-

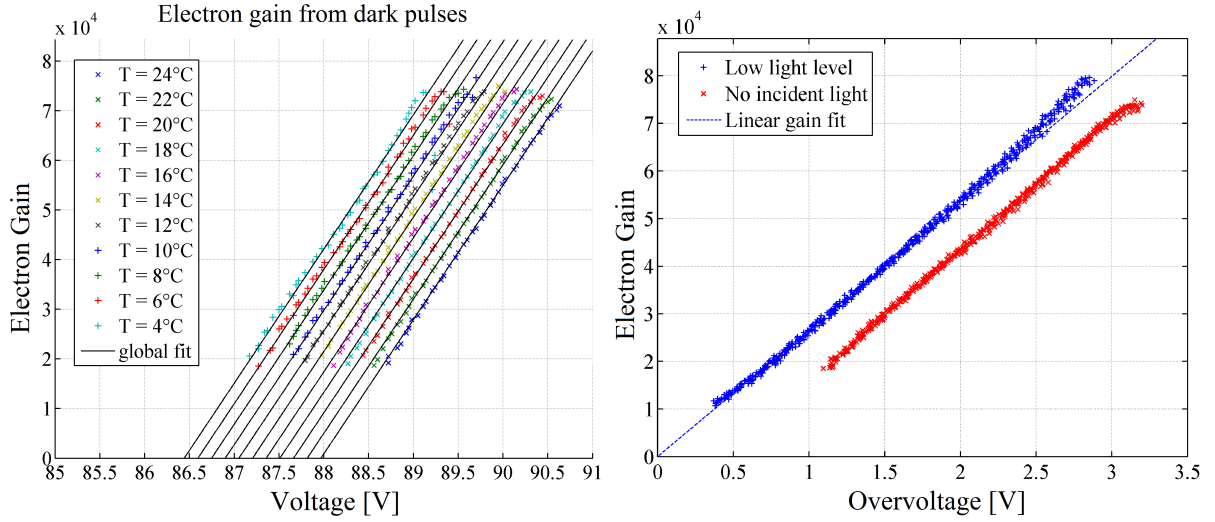


Figure 4.8: Results of electron gain measurements for different temperatures with no incident light. To the left: results of gain calculation as a function of operating voltage for different temperatures, solid lines representing gain fit function. To the right: comparison of gain results with and without incident light pulse as a function of overvoltage.

voltages. Unfortunately, dark histograms include not only pure dark count (uncorrelated noise), but also a noticeable fraction of cross-talk (CT) and afterpulsing (AP) (correlated noise). This results in a non-Poisson distribution of the registered dark pulses. The only histogram peak that is not influenced by the CT+AP noise is the 0 photoelectron (PE) peak. Therefore, one can calculate the true dark rate resulting from the theoretical Poisson process as the ratio of the 0 PE counts to the total number of counts (see eq. 4.12):

$$DR = -\ln\left(\frac{N_0}{N_{total}}\right)/\Delta t \quad (4.12)$$

where N_0 stands for the number of events with no counts, N_{total} for the total number of events and Δt for the time of integration gate.

Measurement results Dark Rate measurements of MAPD have been performed for the following settings. For every temperature and operating voltage a histogram of 10^6 samples has been recorded. An integration gate has been set to 200 ns. Measurements have been done for temperatures from 4°C to 24°C with a step of 2°C. The operating voltage has been set to cover overvoltage values in range from 0 V to 3 V. The data series were recorded at fixed temperatures over the full range of bias voltages. Although the noise pedestal peak (0 PE) was the dominant signal, it was possible to find the midpoint position between 0 PE and 1 PE peaks for overvoltages higher than 1 V and calculate the number of events with no counts.

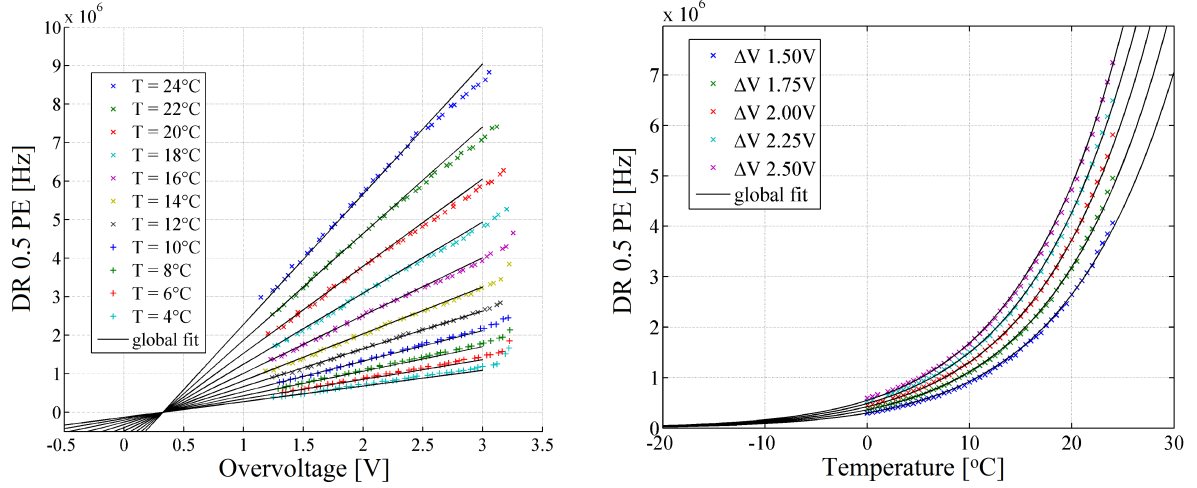


Figure 4.9: Results of dark rate measurements and fit function.

The left plot in figure 4.9 shows the dark rate as a function of overvoltage for different temperatures. As it can be seen, the dark rate is a linear function of the overvoltage. The right plot shows the measurement data as the function of the temperature for different overvoltages, the dependency is close to exponential. The measurement data shown in both figures have been fitted with a function presented in [14]:

$$DR(\Delta V, T) = A \cdot (\Delta V - V_0) \cdot \left(\frac{T}{298}\right)^{3/2} \cdot \exp\left(-\left(\frac{E}{2kT} - \frac{E}{2k \cdot 298}\right)\right) \quad (4.13)$$

where T is absolute temperature, A represents the ratio of dark rate to overvoltage at $T=298$ K (25 °C) (in MHz/V). V_0 is the offset of breakdown voltage calculated from the dark rate with respect to that obtained from gain measurements, and E is the band gap energy for silicon. As it can be seen in figure 4.9, presented function gives good approximation for measurement data. The fit parameters of an example (no. 3 in tables 4.1 and 4.2) of investigated detector are:

- $A = 3.66 \pm 0.02$ MHz/V
- $\Delta V = 275 \pm 73$ mV
- $E = 1.407 \pm 0.003$ eV

The result of the band gap energy fit is different from the value 1.18 eV given by the literature [55]. The reason for that may be the measurement technique. While recording the pulses without the incident light, it is impossible to distinguish if the recorded pulse is a pure dark or the correlated noise (especially late afterpulse) from the previous dark

pulse which was outside the integration window. For lower overvoltages the calculation of the number of 0 PE events is affected by systematic error caused by poor peak separation.

Table 4.2 shows the result of fit parameters for nine samples of the MAPD-3N detector.

Table 4.2: MAPD dark rate results for nine samples

Detector sample	A [MHz/V]	ΔV [V]	E [eV]
1	3.14	0.31	1.24
2	3.35	0.41	1.24
3	3.66	0.28	1.41
4	2.53	0.44	1.30
5	2.84	0.49	1.26
6	1.85	0.31	1.45
7	2.40	0.65	1.32
8	1.21	0.28	1.49
9	2.89	0.49	1.29
mean	2.65	0.41	1.33
SD/mean	27 %	29 %	7 %

As it can be seen, the mean value of the fit result for the band gap energy in silicon $E = 1.33$ eV is different from 1.18 eV. Surprisingly, the dark noise rate varies significantly between measured detectors. The standard deviation of the parameter A is 27 %, the lowest dark rate has been obtained for sample number 8 ($A = 1.21$ MHz/V), the highest for 3 ($A = 3.66$ MHz/V). Significant variations of the dark rate may be explained by differences in the concentrations of the traps (R-G centres) in silicon wafer.

Time intervals between dark pulses

The measurement of time intervals between dark pulses has been performed to confirm the results obtained from histogram measurements. The measurement has been performed for single temperature of 16 °C and overvoltages from 1 V to 2.5 V. For every setting a single waveform has been recorded with an oscilloscope. The sampling frequency has been set to 1 GHz, the waveform length to $1 \cdot 10^6$ samples. The threshold has been set to 0.5 PE. The number of dark counts have Poisson distribution and distribution of intervals should be exponential.

The plot in figure 4.10 shows the distribution of time intervals between dark pulses for different overvoltages. Every measurement has been fitted with single exponential function. From fit functions, the dark count rates have been calculated.

Table 4.3 shows the result of dark rate measurements for sample no. 3 for temperature 16 °C. DR_{hist} values are obtained from histogram measurements and calculated with

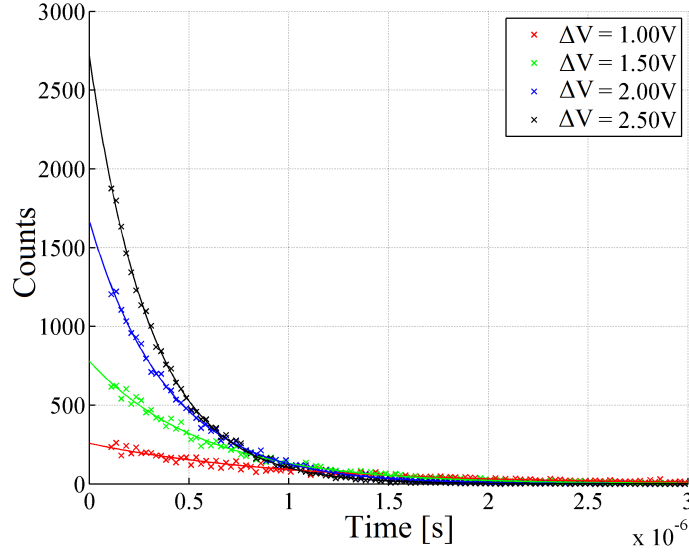


Figure 4.10: Results of dark pulses intervals measurements and exponential fit functions. Time interval distribution for different overvoltages at stable temperature $T = 16^\circ\text{C}$.

Table 4.3: MAPD dark rate measurement comparison for MAPD sample no. 3 at $T = 16^\circ\text{C}$.

ΔV (V)	DR_{time} (MHz)	DR_{hist} (MHz)
1	1.06	1.07
1.5	1.80	1.81
2	2.58	2.56
2.5	3.29	3.30

equation 4.13 and parameters from table 4.2. DR_{time} are the parameters of fit functions from figure 4.10. Both calculation techniques give very similar dark rate results.

Relative photon detection efficiency (PDE)

Relative PDE can be obtained by analysing histograms obtained from measurements using low-level light pulses for various overvoltages. The PDE is calculated by treating the number of detected photoelectrons as a Poisson distribution. The probability of detecting n photoelectrons is:

$$P(n) = \frac{\lambda^n \cdot \exp(-\lambda)}{n!} \quad (4.14)$$

where λ is the mean number of detected photons. The probability of detecting zero photons, which can be determined from the amplitude of the 0 PE (N_0) peak and the total number of events (N_{total}).

$$P(0) = \exp(-\lambda) = \frac{N_0}{N_{total}} \quad (4.15)$$

and from equation 4.15 we can calculate the mean number of detected photons λ .

$$\lambda = -\ln\left(\frac{N_0}{N_{total}}\right) \quad (4.16)$$

The calculated result is corrected by value of dark pulses that occurred randomly inside the integration gate. Since the calculation is based on the integral of pedestal peak, there was no need to correct the effect of correlated noise. The relative PDE is calculated using the formula given in eq. 4.17:

$$\lambda_{light} = \lambda_{total} - \lambda_{dark} = -\ln\left(\frac{N_0}{N_{total}}\right) - \lambda_{dark} \quad (4.17)$$

N_0 is the number of 0 PE counts, N_{total} is the total number of histogram events, λ_{dark} is the probability of thermal generation (calculated from parameters from table 4.2). The PDE has been measured for temperatures in range from 4°C to 16°C in order to minimize the effect of the dark noise.

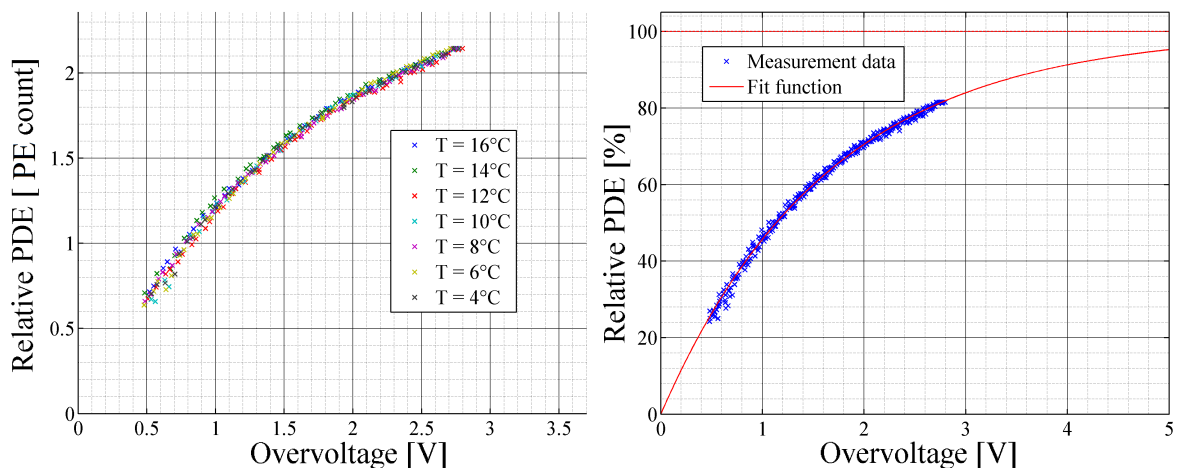


Figure 4.11: Results of relative PDE measurements. To the left: relative PDE [PE counts] as a function of the overvoltage for different temperatures. To the right: the same measurement data scaled and fitted with exponential function.

The left plot in figure 4.11 shows the relative PDE values for different temperatures. As it can be seen the temperature dependency is not visible, this confirms also the correct values of the dark rate used for PDE correction and a good stability of light pulses intensity during the measurement. As it was predicted, the PDE value grows with the increase of bias voltage as the result of growing triggering probability P_{trig} . P_{trig} grows due to the effect of higher impact ionisation coefficient for higher electric field [9] [7]. The PDE dependency of MAPD-3N on the overvoltage is not linear in any range as reported for MPPC detectors from Hamamatsu [14]. The PDE value tends to saturate

to its maximal value. The right plot in figure 4.11 shows the relative PDE values scaled to 100% and fitted with exponent function. As it can be seen, the exponential shape fits measurement data very well. It can be noticed that the PDE reaches 80% of its expected maximal value for overvoltage 2.5 V. The fit function does not have a physical background but can be used for calculation of relative PDE for MAPD detectors:

$$PDE[\%] = 100 \cdot \left(1 - \exp\left(\frac{-\Delta V}{1.64}\right) \right) \quad (4.18)$$

where ΔV is the applied overvoltage.

Summary

Many important parameters of the MAPD detector have been obtained with histogram based measurements. The measurements revealed unexpected electron gain results obtained from the dark pulses. Dark rate measurements showed significant variations between different samples. Similar measurements have been also performed for MPPC S12572-010 detector from Hamamatsu. Initial measurements results have been presented during the International Meeting on Spin Research Program "The SPIN-Praha-2014 Conference" as a talk "Recent results of measurements of photodetectors for the ECAL0 calorimeter for the COMPASS-II experiment" [56]. The final results of measurement have been presented as a poster presentation during 2014 IEEE Nuclear Science Symposium in Seattle, USA [30].

4.3 Recovery time measurements

Recovery time is the period of time after a photon hits a pixel when the pixel cannot detect another photon and may be understood as the time needed to recharge a pixel after a breakdown for traditional SiPM. It depends mostly on the pixel size, which affects the pixel capacitance C_{pix} and the quenching resistance. Recovery time nature in MAPD detector is different due to a different technology of quenching avalanche process and lack of quenching resistors.

Measuring technique

The recovery time of pixels in the MAPD detector was measured with a the method of paired light pulses with the same number of photons directed towards the whole operating surface of the detector. To ensure the participation of most of the pixels in the

avalanche process, photon density on the sample surface was higher than the pixel density in the MAPD detector. Figure 4.12 shows the schematic of measurement system used for calculation of the recovery time. Light pulses were produced with a fast laser diode system EIG200DX with a wavelength of 440 nm. The laser controller was triggered with two paired pulses with a known delay. Signal from MAPD has been measured with a fast amplifier and an oscilloscope. The oscilloscope has been programmed to record a period of 2 ms and it was possible to set the maximum delay between light pulses to 1 ms.

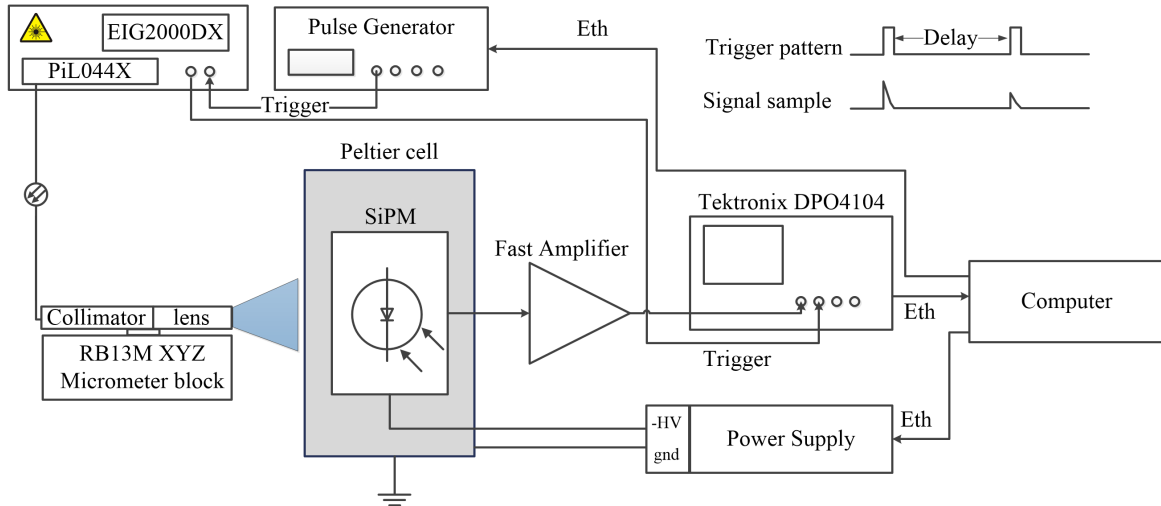


Figure 4.12: Schematic of a measurement system for recovery time calculation.

Signal amplitude test

While performing the measurements of the recovery time, it is crucial to ensure that most of the pixels are fired with a single light pulse. Tests of the light source strength were performed with MAPD-3N detector biased at two different voltages. For both measurements the MAPD-3N signal charge has been measured as a function of the laser tune settings. The first measurement was performed in the proportional mode, when the operating voltage is below the breakdown. In this mode, the signal amplitude is proportional to the number of detected photons. During the second measurement, the detector was biased above the breakdown voltage (Geiger mode), so the signal amplitude was proportional to the number of fired pixels. Both measurements were performed at the same temperature of 22 °C. The breakdown voltage is around 86.5 V for 22 °C.

Both measurements are presented in figure 4.13, the blue plot shows result for the measurement at 90 V, the green plot shows result with bias voltage of 86 V, which is 0.5 V below the breakdown. It can be seen, from the green plot, that number of incident photons

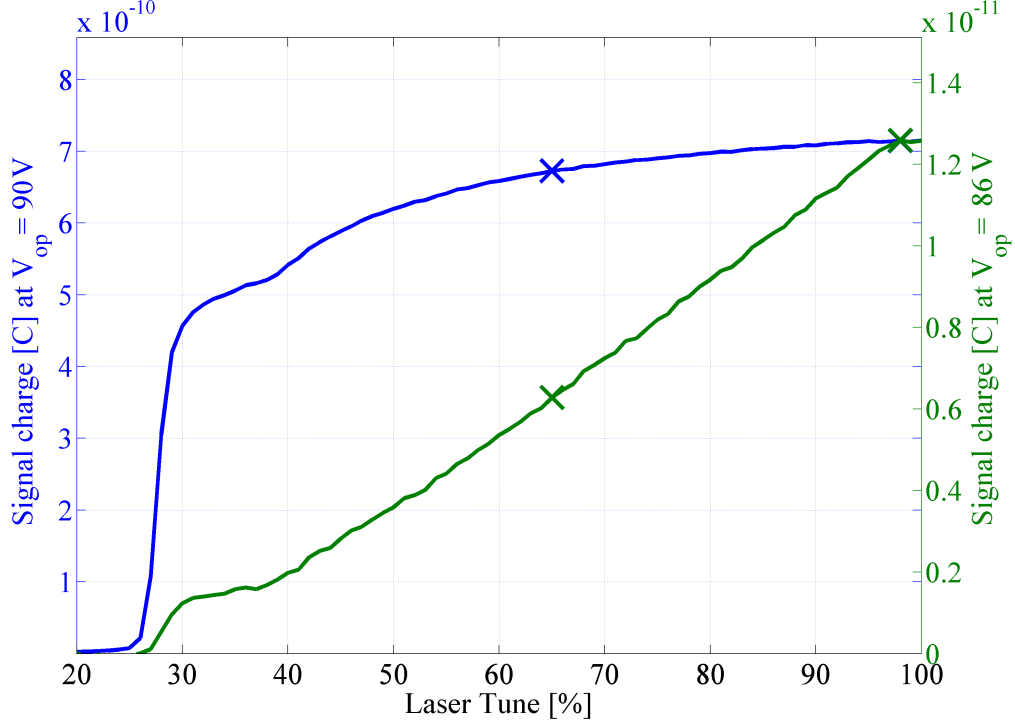


Figure 4.13: Light source strength test. Blue plot: Signal amplitude for MAPD-3N working in Geiger mode, biased at 90V. Green plot: Linear response of MAPD-3N, operating voltage below the breakdown voltage.

grows linearly for laser tune settings in the range from 40% to 100%. The number of fired pixels, when the detector is biased above the breakdown, has a Poisson distribution. The probability of firing all pixels is $P_{trig} = 1 - \exp(-X)$, where X is mean number of photons hitting one pixel. The green plot shows that number of incident photons is two times higher when comparing laser tune settings of 65% and 98%. Looking at the blue plot, it can be seen that, for the detector working in Geiger mode, the number of fired pixels grows only by 6%. To calculate the percentage of fired pixels, the equation 4.19 has to be solved.

$$\frac{P_{trig_98\%}}{P_{trig_65\%}} = \frac{1 - \exp(-2X)}{1 - \exp(-1X)} = \frac{7.15}{6.73} = 1.06 \quad (4.19)$$

The solution of the equation 4.19 is:

$$X = 2.78 \quad (4.20)$$

Knowing the $X = 2.78$ it is possible to calculate the percentage of fired pixels for laser tune of 65% and 98%;

$$P_{trig_65\%} = 1 - \exp(-M) = 1 - \exp(-2.78) = 0.938 \quad (4.21)$$

$$P_{trig_98\%} = 1 - \exp(-2X) = 1 - \exp(-2 \cdot 2.78) = 0.996 \quad (4.22)$$

The above results confirm that almost all pixels of the MAPD-3N are fired for laser tune 98% and operating voltage 90V at 22°C.

Measurement results

The first measurement of the recovery time has been performed for MAPD-3N detector biased at 90V and in the temperature of 22°C. For comparison, also a SiPM detector from Hamamatsu, MPPC S12572-010P has been measured. The MPPC detector is made in a standard technology with quenching resistors placed on top of the pixels, where the recovery time constant is dependent on the pixel capacitance and the quenching resistance.

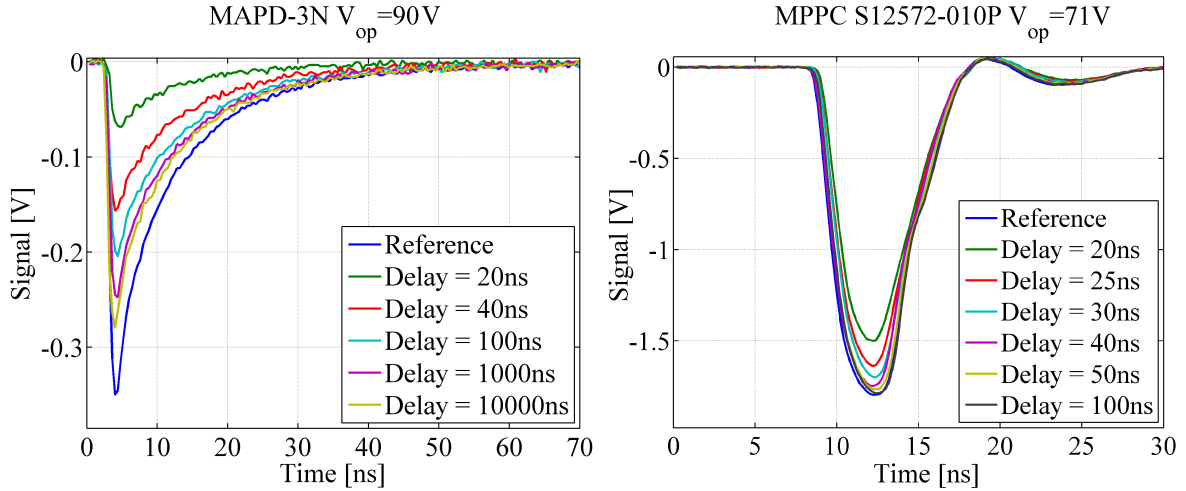


Figure 4.14: Recovery time measurement, signal samples for different delays. Blue plots - reference signals without the recovery effect. To the left: MAPD-3N detector biased at 90V and 22°C. To the right: MPPC S12572-010P biased at 71V and 22°C.

As it can be seen in figure 4.14, the longer delay of the following light pulse the higher the amplitude of the signal for both detectors. However, the recovery time of the MAPD-3N detector is much longer. For 100 ns delay, the recovery of the MAPD-3N is around 50% while the signal from MPPC is recovered by almost 100%. The recovery of MPPC detector has an exponential shape with the time constant $\tau = 15$ ns. The recovery phenomena of MAPD detector is much more complicated, what is the result of the quenching mechanism described in section 2.3. The electric field in the multiplication area is restored due to leakage of the accumulated charge to the substrate directly via the biased p-n junction between the first epilayer and the n+ region.

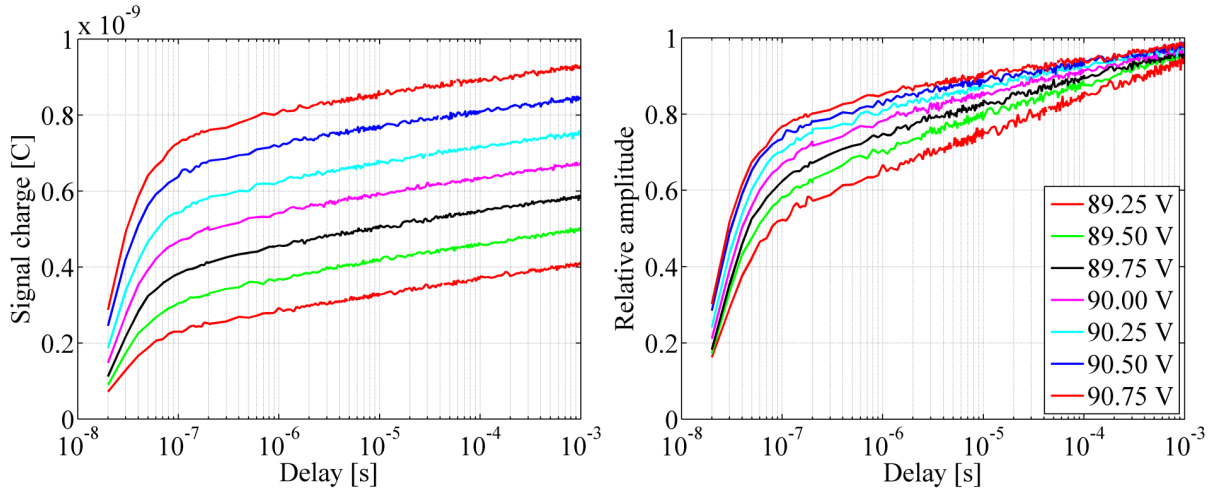


Figure 4.15: Amplitudes of the photoresponse of the MAPD-3N to the second light pulse as a function of the delay time for different operating voltages. To the left: the measured charge of the second response. To the right: signal amplitude relative to the amplitude of the response to the first light pulse. Note the logarithmic time scale.

As it can be seen in figure 4.15, the shape of the recovery curve is not exponential and can be divided into fast and slow part. The fast part of the curve has exponential shape with the time constant $\tau = 35$ ns and its scaling factor depends linearly on the applied operating voltage (see left plot in figure 4.15). The slow part has a logarithmic shape with the same amplitude and tilt regardless the operating voltage.

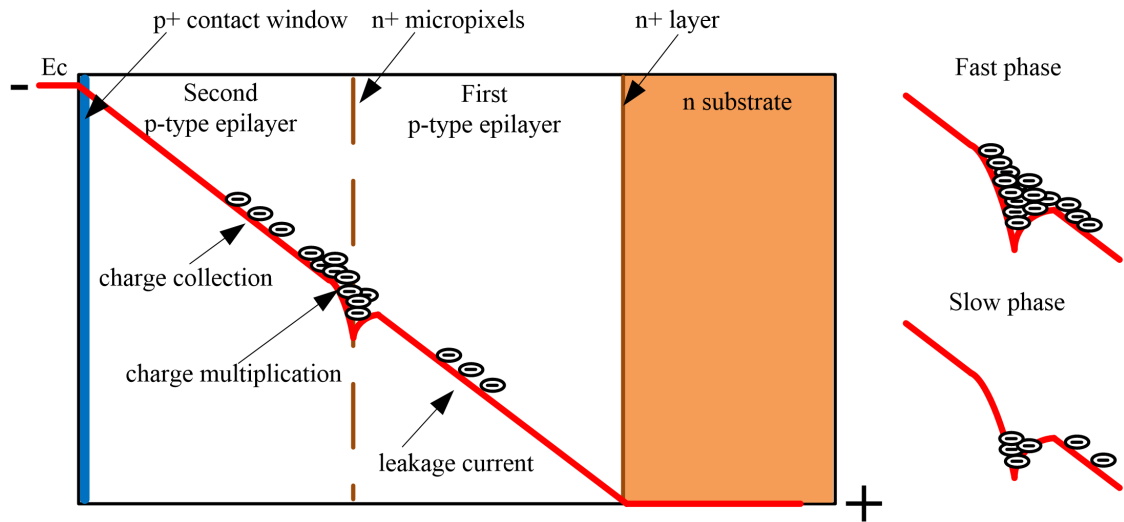


Figure 4.16: Schematic diagram showing: (a) the traverse section of MAPD and energy band diagram with applied voltage and (b) two phases of pixel recovery after an avalanche.

The fast part of the recovery curve is a result of several mechanisms and it is very difficult to describe it analytically. As it can be seen in figure 4.16, during the fast phase,

the potential well is fully filled with electrons. In this phase a large current is observed due to the absence of potential well in the n+ region. Another mechanism which affects the recovery may be a voltage drop on a sheet resistance of the p+ contact layer, which is the effect of hole current. After a period of 200 ns the slow phase becomes visible. Electrons trapped in a potential well discharge by means of a low leakage current.

The leakage current of p-n junction has an exponential dependency on the applied voltage and can be described with equation 4.23. During the process of discharging, the potential well deepens, what affects the leakage current:

$$I = -\frac{dQ}{dt} = I_0 \exp\left(\frac{\Delta U}{V_t}\right) \quad (4.23)$$

where I_0 is the initial leakage current, ΔU is the depth of a potential well and $V_t = kT/q = 25.85 \text{ mV}$ at 300 K. Knowing that the charge accumulated in the potential well will result in a voltage drop:

$$\Delta U = \frac{\Delta Q}{C_{pix}} \quad (4.24)$$

equation 4.23 can be transformed to

$$Q(t) = V_t C_{pix} \ln\left(\frac{I_0 \cdot t}{V_t \cdot C_{pix}} + 1\right) \quad (4.25)$$

The above equation describes the logarithmic character of the slow part of the recovery curve. As seen in figure 4.15, it is not dependent on applied operating voltage. Slow recovery depends on the pixel capacitance and the initial leakage current, which is the result of doping levels of first p-type epilayer and n+ microwells.

MAPD signal shape

The Shockley–Ramo theorem allows calculating the instantaneous electric current induced by a charge moving in the electric field of the depletion region in SiPM detector. The theorem was published in William Shockley’s paper in 1938 [57]. The Shockley–Ramo theorem states that the current i induced on a given electrode due to the motion of an electron is given by:

$$i = E_v \cdot q \cdot v \quad (4.26)$$

where q is the charge of the electron, v it the velocity and E_v is the component of electric field in the direction of v . As it was already explained, the depletion region in MAPD detector is divided into two regions of equal thickness (figure 4.17).

Figure 4.17 shows on the left: the traverse section of MAPD and three phases of current generation in depletion region, and on the right: the schematic shape of the

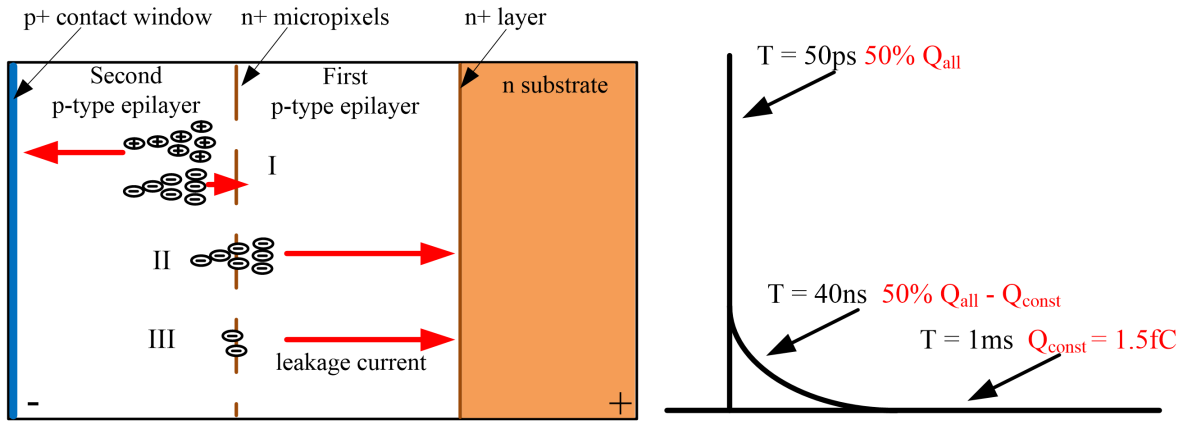


Figure 4.17: To the left: the traverse section of MAPD and three phases of current generation in depletion region. To the right: The schematic of resulting MAPD signal shape.

MAPD signal. The MAPD signal consists of three parts with different time constants corresponding to three phases of charge movement in depletion region of the detector. The fastest part is mainly the hole current from ionisation in the second epilayer during the charge multiplication within the first 50 ps (phase I in figure 4.17). Time of 50 ps has been estimated from the width of the epilayer, holes mobility and electric field . The second part of the signal corresponds to electron movement in the first epilayer, it is the charge that has not been trapped in the potential well, the time constant of this part is around 40 ns. The analytical dependency of this component of the signal has not been solved. The last phase is the charge that was accumulated in the potential well and has very long recovery time, the charge of this part is the same regardless the operating voltage and is defined by the depth of the potential well. The measurements of recovery time (see figure 4.15), showed that the charge of the signal which is accumulated in the potential well is around 1.5 fC per pixel.

4.4 MAPD electron gain investigation

The electron gain measurements of the MAPD-3N detector (section 4.2) showed that the gain measured from the dark pulses is lower when compared with measurements obtained with light pulses. This phenomenon was under investigation for a long time and its solution is one of the milestones of this thesis. Many ideas have been proposed and then rejected. The final solution of this problem has been found after the measurements of the recovery time.

MAPD and MPPC electron gain measurements

To confirm, that the results are not the effect of the measurement system neither data analysis software, measurements have been also performed for MPPC S12572 detector. Both detectors have been measured in varying temperature, MAPD-3N from 4 °C to 24 °C and MPPC from 12 °C to 24 °C due to problems with water condensation. The length of the integration window was the same (200 ns) for both measurements. In both cases, the measurements were taken with and without the incident light pulses.

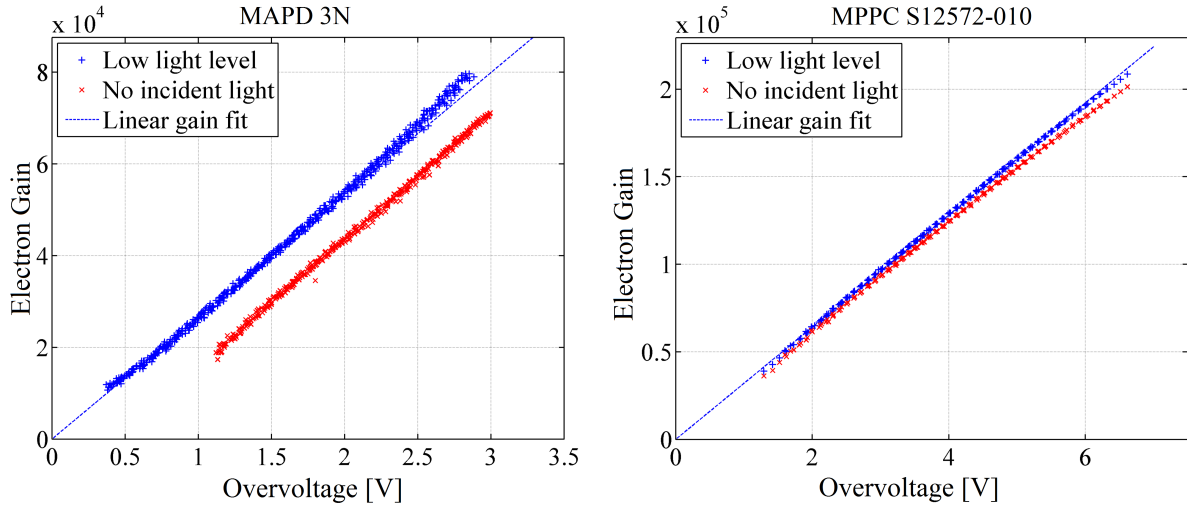


Figure 4.18: Electron gain measurement as a function of overvoltage for MAPD-3N (to the left) and MPPC S12572-010 (to the right). Both measurements performed with (blue) and without (red) incident light.

Figure 4.18 shows electron gain measurements for both detectors. As it can be seen on the left plot, the gain measured with dark pulses is significantly lower, the difference is constant regardless the supply voltage. For MPPC detector (right plot) this effect is not present. There is small gain difference, but this is due to the fact that dark pulses appear in the integration window randomly and the length of the integration window is too short. Therefore, looking at measurements of MPPC detector, one can say that both hardware and data analysis work properly.

Electron gain dependency on wavelength and length of integration window

Next step in electron gain analysis was to check the dependency of the results on the length of the integration window. As it was noticed in the previous section, the length of integration window may affect the electron gain measurements. This measurement was

performed only for MAPD-3N. Then, two different light sources were used to ensure that there is no gain dependency on the wavelength or related position of the primary electron-hole pair in the depletion region. (Different wavelengths means different absorption depths in silicon, blue light produces electron-hole pairs close to the top surface of the detector, red light penetrates the depletion region much deeper and most of the primary electron-hole pairs are ionised near the region of buried microwells.)

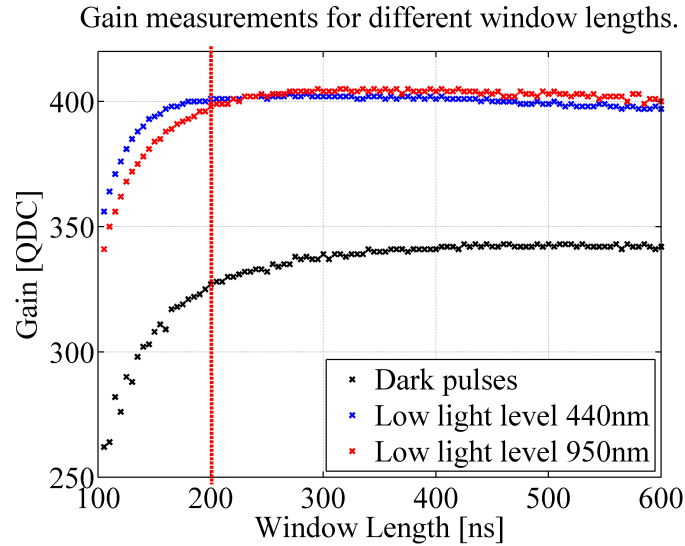


Figure 4.19: MAPD-3N electron gain measurement as a function of the integrating window length. The measurement has been performed for two wavelengths and without the incident light. Supply voltage is 88.5 V at temperature of 8 °C.

Figure 4.19 shows the results of electron gain measurement as a function of the length of integration window. Blue and red plots represent respectively 440 nm and 950 nm wavelength. Black plot is the electron gain obtained only with dark counts. For measurements with incident photons, the electron gain rises with the length of integration window and saturates for the value of 200 ns what is the length of the signal pulse. The plots are not identical, this is caused by the fact that the 440 nm light was produced with a pico-second laser system and 950 nm photons were produced with a red LED and the Kapustinsky driver [58], what resulted in longer light pulse (around 3 ns FWHM). The gain calculated with the dark pulses saturates at lower value (60 QDC less). What was predicted, the length of integrating window for dark measurements should be longer, the saturation is obtained for window length of 300 ns. This is the result of random positions of signal in the integrating window. For light measurements a noticeable drop of gain for longer window length is visible. This is caused by the fact that mean number of incident photons is the same regardless the window length (usually mean number of photons is less than 4) and number of dark pulses grows linearly with the window length. In result, for a longer

window length, dark pulses may be a noticeable part of recorded signal, which causes lower electron gain result. The above results confirm that the electron gain of MAPD-3N is not dependent on the wavelength. It is worth to notice that the length of integrating window should be 300 ns, to suppress the influence of dark pulses for light measurement and be in saturation area for dark measurements.

Recovery time influence on the electron gain

The final answer for lower gain values of dark pulses, has been found after the recovery time of the detector has been measured (in section 4.3). As it was shown, the recovery time of the MAPD-3N is much longer than for MPPC device. The quenching process in MAPD is very complicated, a constant part of generated charge is trapped in a buried microwell and cannot be recorded within a short integration gate. Small leakage current is responsible for recharging and causes long recovery time. It will be shown that long recovery time is the reason of lower charge of dark pulses. It should be reminded that dark pulses are mainly thermally generated carriers enhanced by trap assisted tunneling (TAT) through Shockley-Read-Hall (SRH) recombination-generation (R-G) centres. SRH recombination is determined by the amount of impurities and defects in the silicon. The number of generation centres in silicon depends on the quality and technology used. The more impurities and crystal defects in epitaxial layer, the higher dark count rate. The measurements of the dark rate from section 4.2 have already shown that dark count rate varies significantly between different samples of the detector. This means that the quality of the silicon wafer is not constant over its surface. The number and distribution of recombination-generation centres can be visualised by measuring the minority carrier lifetime. This parameter is one of the most important parameters for the characterisation of semiconductor wafers. The lifetime is related to the generation rate by:

$$\tau = \frac{n_i}{G} \quad (4.27)$$

where τ is the minority carrier lifetime, n_i is the intrinsic carriers concentration and G is the generation rate (proportional to dark count rate). It's important to remember that most of the dark pulses are the result of generation through defects and they do not occur in perfectly pure and undefected material. The dark rate depends strongly on the purity of the silicon in the epilayer.

Figure 4.20 shows an example measurement of minority carriers lifetime in a 125 mm by 125 mm silicon wafer with 122 μm resolution from [59]. As it can be seen, the inhomogeneity of lifetime in presented sample is noticeable. The lifetime in the central part

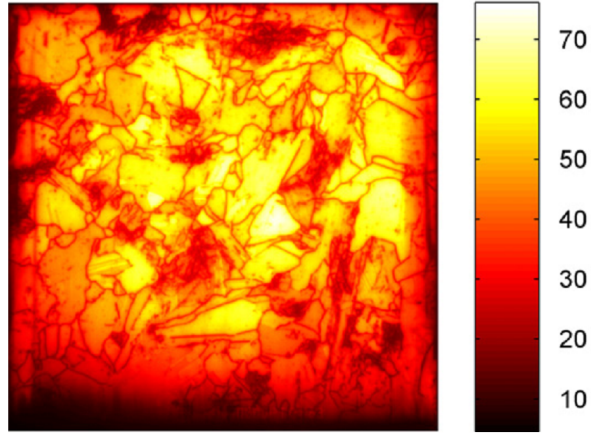


Figure 4.20: An example of effective minority carrier lifetime (μs) map of a $125\text{ mm} \times 125\text{ mm}$ silicon wafer with at a resolution of $122\ \mu\text{m} \times 122\ \mu\text{m}$ [59].

of the wafer is much longer. The real max/min difference in lifetime is even higher and would be definitely visible in a measurement performed with higher spacial resolution.

In high density SiPM detectors, with the pixels size of $10\ \mu\text{m} \times 10\ \mu\text{m}$, the differences in lifetime can reach much higher values than in presented lifetime map. In those detectors, only small part of pixels contribute to substantial part of the dark pulses. Pixels containing high number of R-G centres have much higher dark count rate. High dark rate and long recovery time result with lower electron gain value measured from dark pulses. The pixels with higher dark rate cannot fully recover before next triggering and their electron gain is lower. This phenomenon is not visible in MPPC detectors, due to fast recovery time (less than 50 ns).

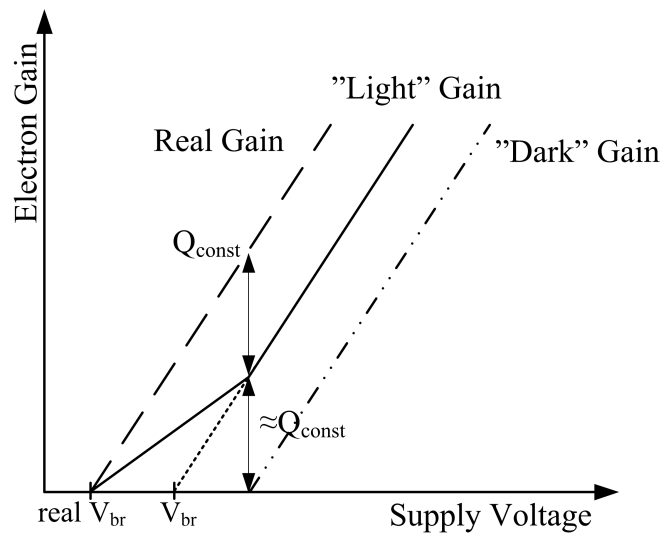


Figure 4.21: A model of MAPD electron gain.

Figure 4.21 presents three curves representing electron gain of the MAPD detector. The solid line represents the gain that is measured with the incident light. Knowing the recovery time character and the shape of MAPD signal (see figure 4.17), we can conclude that within the 200 ns integrating gate we can register only the fast part of the signal, which is related to the fast current signal from all holes and the fast part of electron current. The real electron gain of MAPD is the sum of charge that is measured and the charge that is trapped in potential wells (Q_{const}). The part of electrons that is trapped in a potential well cannot be recorded due to a very long time constant. For lower values of the overvoltage, until the potential well is fully filled, only charge movement of holes and electrons in second epilayer is observed (see also figure 4.17). From a certain overvoltage, when the potential well is fully filled, movement of electrons in first epilayer is also visible, thus the slope of the "light" electron gain curve changes. The right dotted curve is the gain from dark pulses. This gain is always lower than the light gain, but it is different for different samples. This is the result of differences in dark rate, which depends on the silicon wafer quality especially number and inhomogeneities of recombination-generation centres.

Chapter 5

Results of SiPM parameter scans

While working with new technology of a SiPM detector, it is very important to examine uniformity of various parameters over different pixels. These measurements assume both histogram based and signal shape analysis. A single scan consists of a set of measurements performed for different light spot coordinates on detector's surface. This measurement allows measuring all of previously mentioned parameters as a function of photon hit coordinates and therefore calculation of uniformity over a whole detector's surface. Because of time limitation, two types of scans are taken into account:

1. Focused scan: light is focused to a spot with size much smaller than the size of a single pixel. Single measurement step is very small and measuring field of interest containing only small number of pixels is possible in a reasonable time. It is possible to measure the response from a single pixel and analyse pixel's shape, dead space and relative *PDE* in between pixels.
2. Rough scan: The light spot size covers larger number of pixels, scanning step is bigger and allows a scan of the full detector surface but with no information about individual pixel positions. The signal comes from larger number of pixels. In the rough scan it is also possible to measure signal shape, which needs higher signal amplitude (more excited pixels) due to noise issues.

Scan procedure

A single scan of the detector surface consists of the following stages:

1. Set working parameters: operating voltage, temperature, light level and pulse repetition frequency (*PRF*).

2. Perform fast a scan of signal amplitude with a rough step and calculate boundary coordinates of the detector's surface.
3. Choose a region of interest and perform light beam focusing in the middle of this region.
4. Scan the desired region: collect histograms of amplitudes or signal waveforms for every point of the scan.
5. Calculate and plot parameters. Analyse their uniformity.

5.1 Signal shape scans

In a standard SiPM detector, the shape of the signal is determined by electrical parameters of a single pixel. As it was presented in section 2.2, the time constant of the signal tail is proportional to the pixel capacitance and the value of quenching resistor. Hence, detectors with high density of pixels have faster signal response. The technology of MAPD detector is different from the standard SiPM. The equivalent electrical circuit of MAPD-3N and its cross section has been presented in section 2.3. The function of quenching resistors has been replaced by buried microwells. In theory, signal of MAPD should be very short. Initial measurements of MAPD signal shape have revealed that its fall time is around 30 ns, what is much longer than the fall time of MPPC S12572 which has quenching resistors and similar pixel size (examples of signal shape are presented in section 4.3). What is more, it was measured that the shape of the MAPD signal depends on the position of the light spot on the detector surface. This is the result of sheet resistance of p+ contact layer, which is responsible for signal collection from all pixels to a metallic anode frame (see figure 5.1). To investigate signal shape dependence on the p+ contact layer, the measurements of signal shape as a function of light spot coordinates on the detector surface have been performed. Measurements have been performed with a fast amplifier and acquisition system described in section 3.3.

Signal shape measurement

The scan of signal shape has been performed for one sample of MAPD-3N detector. The whole area of detector surface has been measured with a step of 100 μm . The size of the light spot was approximately 300 μm . For each light beam position, an average from 128 signal responses has been recorded. Below, the measurement settings are presented:

- detector temperature: 16 $^{\circ}\text{C}$,

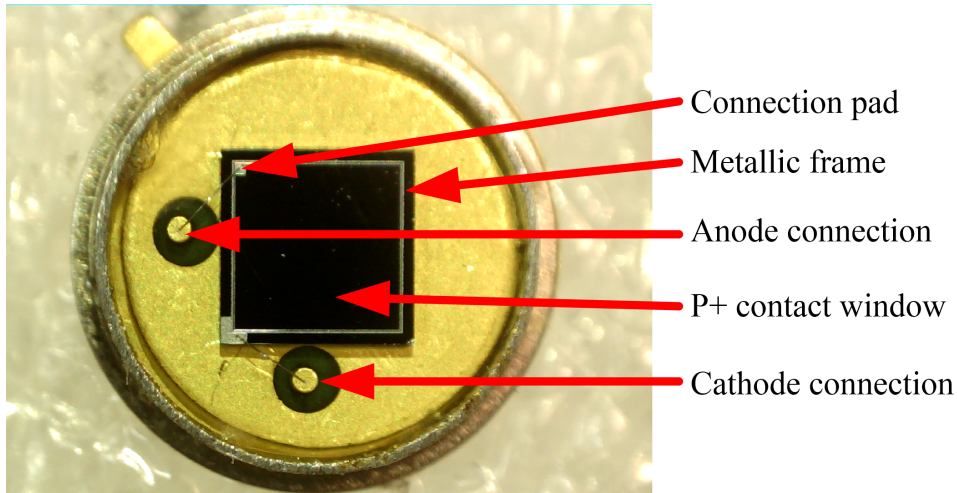


Figure 5.1: MAPD-3N top view photo. Connection pads and metallic frame marked with arrows.

- supply voltage: 89 V,
- electron gain: $6 \cdot 10^4$,
- light pulse repetition frequency: 500 Hz

A set of parameters can be calculated from every recorded signal: signal charge, pulse amplitude, rise and fall time and full width at half maximum (FWHM). Signal shapes recorded for different light beam positions are presented on the right plot in figure 5.2. The left plot is a signal charge map for all light beam positions. What is more, there are 4 coloured points, whose positions correspond to signal shapes from the right plot. Results from the left plot show that the charge uniformity is good, the edges of the detector are blurry due to relatively wide light spot size. The yellow points on the plot are the edges of the detector's active area, which is 3 mm by 3 mm. The mean signal charge is around 11.5 pC (red colour) what corresponds to 1200 fired pixels.

The right plot in figure 5.2 contains 4 curves representing signals from different light beam positions. Results show strong dependence of the signal shape on the light beam position. Signals recorded when illuminating the centre of the detectors surface are much slower from signals near the edges, while the charge of the signal is almost the same: 11 pC to 12 pC (see table 5.1). As it can be seen, the shortest rise and fall time is achieved when the corners of detector surface are illuminated. For these signals the amplitude is the highest, while the charge is slightly lower because part of the photons are not hitting the active area of the detector.

Figure 5.3 shows the signal shape parameters as a function of light beam coordinates. As it can be seen on the signal amplitude plot (top-left), the highest signal amplitude

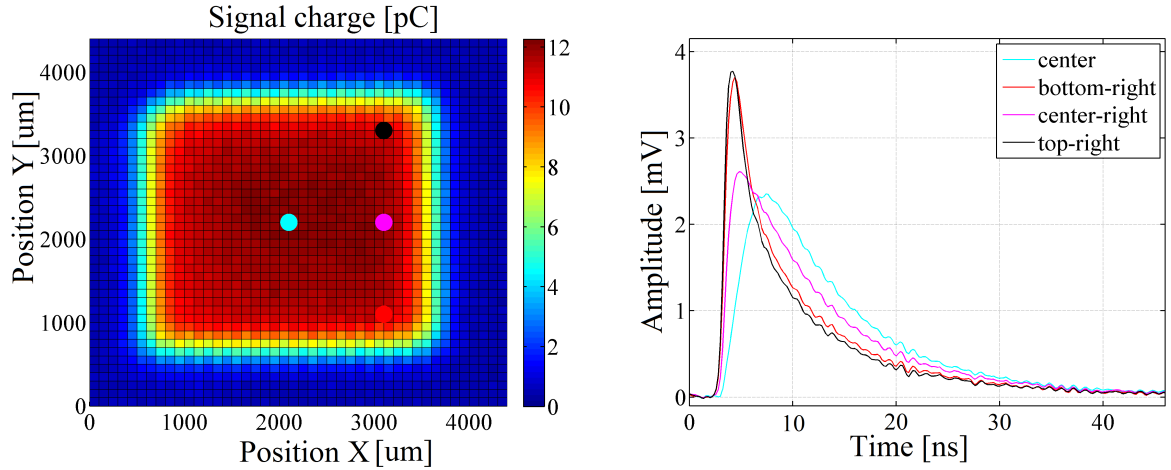


Figure 5.2: To the left: the signal charge calculated from recorded signals. To the right: Four signal samples recorder at different light beam position, the colour of the plot corresponds to one of the point on the charge scan.

Table 5.1: Calculated parameters of measured signal shapes

Hit position	Charge [pC]	Amplitude [mV]	Rise time [ns]	Fall time [ns]
Center	11.9	2.4	2.6	22.3
Bottom-right	10.9	3.7	1.0	15.8
Center-right	11.7	2.6	1.1	20.3
Top-right	11.0	3.8	0.9	13.9

is recorded when the light beam is positioned near the corners of the active area. The signal amplitudes recorded in the centre of the active area are almost two times lower than those recorded in the corners. Three timing parameters have been also presented: FWHM, rise time and fall time. The top-right plot shows the signal FWHM distribution, as it was predicted the FWHM near the edges is the shortest (around 2 ns). Bottom plots shows the rise and fall time. Both parameters are dependent on the light beam position. The rise time varies from 1 ns near the edges to 2.6 ns in the centre. The fall time plot looks noisy, the calculation of the parameter is influenced by interferences visible also on the right plot in figure 5.2. The fall time varies from 8 ns near the corners to 21 ns in the centre.

The reason for a strong signal dependence on light beam position is a sheet resistance introduced by the thin p+ contact layer laying on top of the detector window with a resistivity of about $0.01 \Omega \text{ cm}$ [22]. Thus contact layer may be modelled as a grid of low pass filters. The thickness of this layer has to be low enough to allow light to reach avalanche region and thick enough for fast collection of electrical signal. According to quantum efficiency measurement from device specification [19], the thickness of p+ contact layer has been assessed to be around 40 nm. The contact layer is connected to the metallic

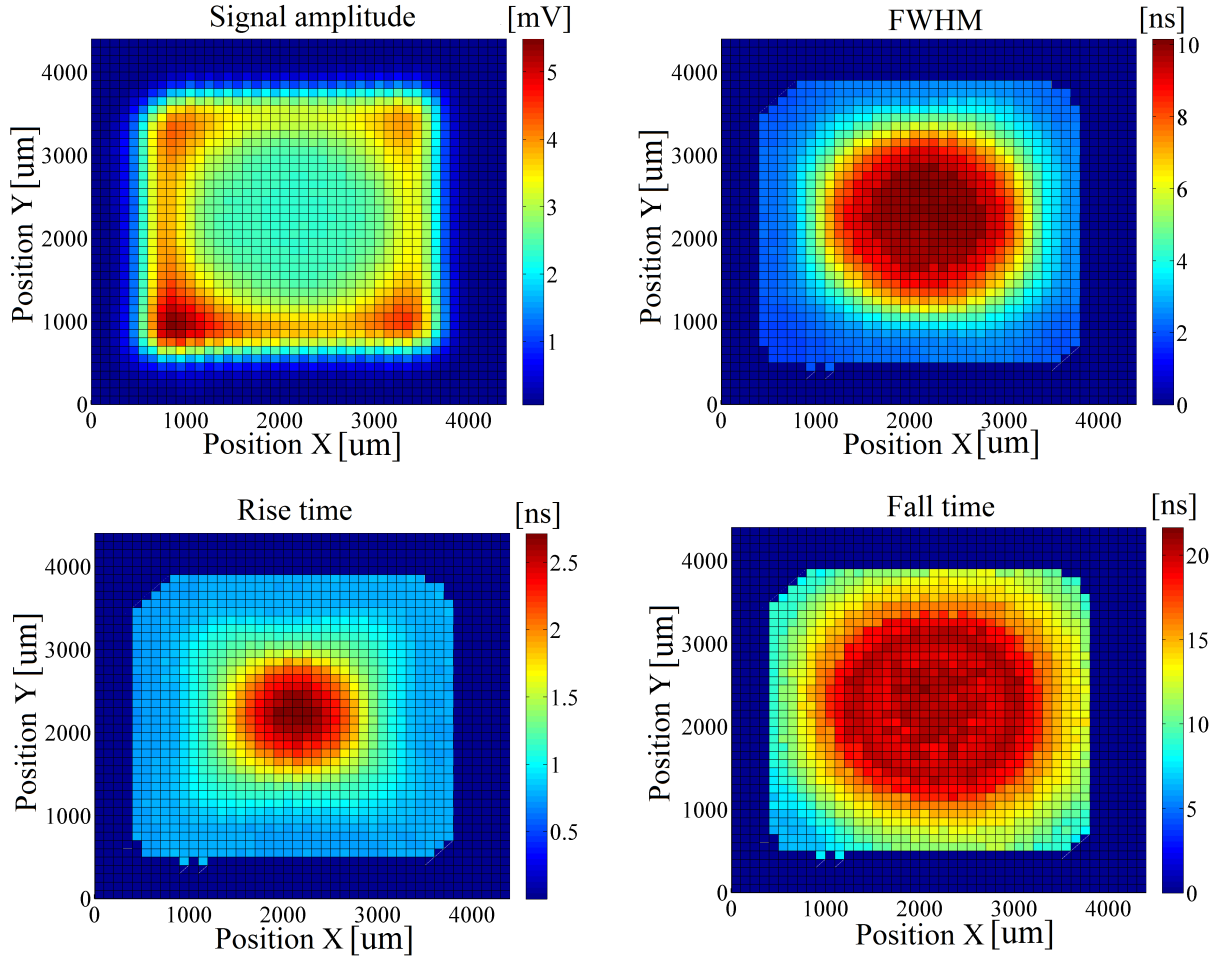


Figure 5.3: MAPD-3N signal shape maps. Top-left: signal amplitude, top-right: signal FWHM (full width at half maximum), bottom-left: signal rise time, bottom-right: signal fall time.

frame at the edges of the active area (see figure 5.1). The width of the metallic frame is around 20 μm .

P+ contact layer model

Knowing the topology and the signal shape dependence of the detector it was possible to build a model of the contact layer and simulate the signal shape. This model is presented in figure 5.4. The contact layer has been modelled as a square lattice of identical resistors with capacitors connected to ground. Each resistor represents a square part of a connection layer, the size of a square is dependent on the number of nodes in the lattice. The initial value of each resistor has been calculated from the resistivity divided by the thickness of the contact layer, the result of this operation will be in units of Ω/sq , which is dimensionally equal to an ohm. The reason for the name "ohms per square" is that

a square sheet of a semiconductor has the same resistance regardless of the size of the square. For MAPD-3N the initial sheet resistance can be calculated as follows:

$$R = \frac{\rho}{W} = \frac{0.01 \Omega \text{ cm}}{40 \text{ nm}} = 2500 \Omega/\text{sq} \quad (5.1)$$

where $\rho = 0.01 \Omega \text{ cm}$ is the resistivity and $W = 40 \text{ nm}$ is thickness of a contact layer. As it has been calculated, the sheet resistance of the contact layer is $2500 \Omega/\text{sq}$. A single capacitor C_{node} is connected to every node of the lattice, it represents a capacitance of the depletion region. Additional capacitor of 16 pF is connected to the common node, and it represents the capacitance of the metallic connection frame of the anode. The capacitance of node capacitors is reversely proportional to the number of nodes. The sum of all capacitors should be equal to 160 pF which is the terminal capacitance of the MAPD-3N. The model contains also a 5Ω resistor and an amplifier which was used in signal shape measurements. The amplifier with AD8000 chip works in voltage follower configuration to maintain wide signal bandwidth. The voltage drop on 5Ω resistor is followed to the output of the amplifier. The simulation assumes that the current source will be connected to different nodes of the square lattice. For every position of the current source, the shape of signal response will be analysed. The value of sheet resistance will be modified to fit the measurement data. Electrical simulations are performed in a LTspice. The input file for simulation is generated with a MATLAB script, so the size of the lattice and its parameters can be easily adjusted. The analysed signal is the voltage signal on the 50Ω resistor (resistor to the right in figure 5.4), which simulates the input resistance of an oscilloscope.

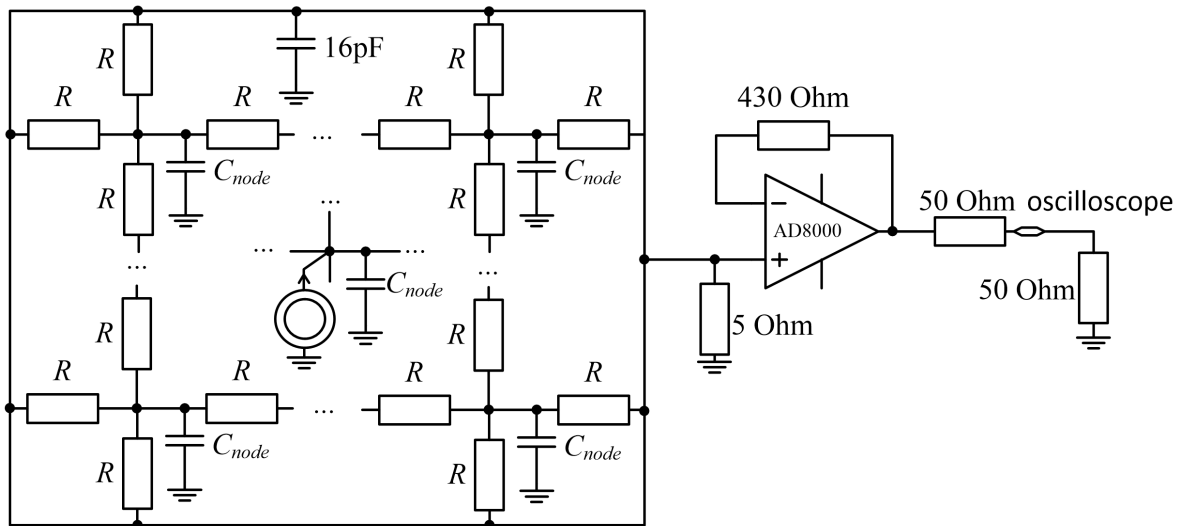


Figure 5.4: Simplified schematic of equivalent circuit of the contact layer with a current source connected to the middle node. The number of nodes in a square lattice can be adjusted.

P+ contact layer simulation result

The simulation has been performed for a resistor lattice with 32 x 32 nodes to match the number of light beam position steps in the signal shape measurements. The only adjustable parameter of simulation was the value of the sheet resistance of the contact layer. The value of capacitors at the nodes was calculated to be 140 fF.

$$C_{node} = \frac{C_{terminal} - C_{frame}}{n. \text{ of nodes}} = \frac{160 \text{ pF} - 16 \text{ pF}}{32 \cdot 32} = 140 \text{ fF} \quad (5.2)$$

The sum of all capacitances equals 160 pF. The parameter of sheet resistance has been manually found by fitting the signal shape from the simulation and measurements. Figure 5.5 shows the results of signal simulation in the central and corner node. The red plot is a signal from the corner node, the black plot represents signal from the central node. For both points, simulation data (solid line) and measurement data (x points) are plotted. The amplitude of both signals has been normalized to 1. As it can be seen, the simulation data fit the measurement data very well. Both rise and fall time are well determined. By

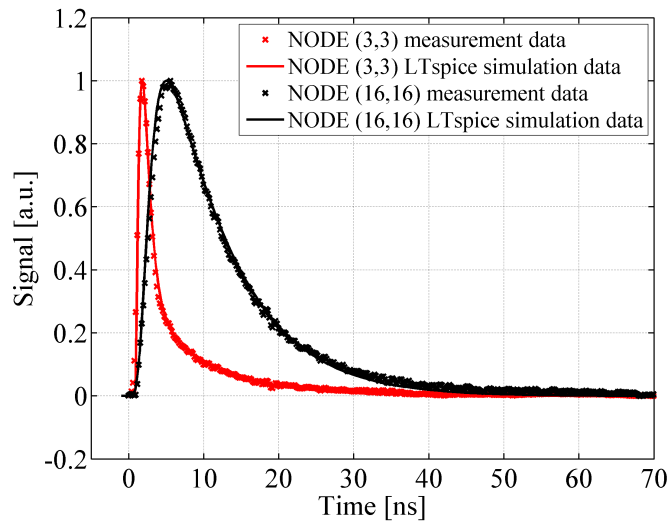


Figure 5.5: Results of signal simulation in the central and corner node compared to measurement data. The red plot is the signal from the corner node, the black plot represents signal from the central node. Note: both signals have been scaled to the same amplitude.

fitting the central and border points we can assume that simulation at the other nodes will also give good results. The final value of the sheet resistance was found to be $540 \Omega/\text{sq}$, which is around 5 times less than the initial value. Assuming that the width of contact layer is 40 nm, an actual resistivity ρ of the contact layer can be calculated:

$$\rho = R_s \cdot W = 540 \Omega/\text{sq} \cdot 40 \text{ nm} = 0.0022 \Omega \text{ cm} \quad (5.3)$$

where R_s is the new value of sheet resistance and W is the thickness of the contact layer. The new value of resistivity is $0.0022 \Omega \text{ cm}$. This difference can be easily explained: while the estimated width of the contact layer can be only slightly different from reality, the resistivity given by a producer is the approximate value. Knowing the proper value of the sheet resistance, the simulation has been performed for all nodes of the proposed model. Figure 5.6 shows the plot of the signal FWHM as a function of the light beam position. The red dots are the FWHMs calculated from measurement data, the black mesh represents simulation data. The results of simulation fits the measurement data very well. This shows that both model of contact layer and its parameters were correctly chosen and calculated. The maximum and minimum FWHM values and the shape of both plots are almost identical. There are small differences for nodes close to edges, this is the result of finite number of nodes in simulation and the fact that in measurements, the size of the light spot was quite big, around $300 \mu\text{m}$.

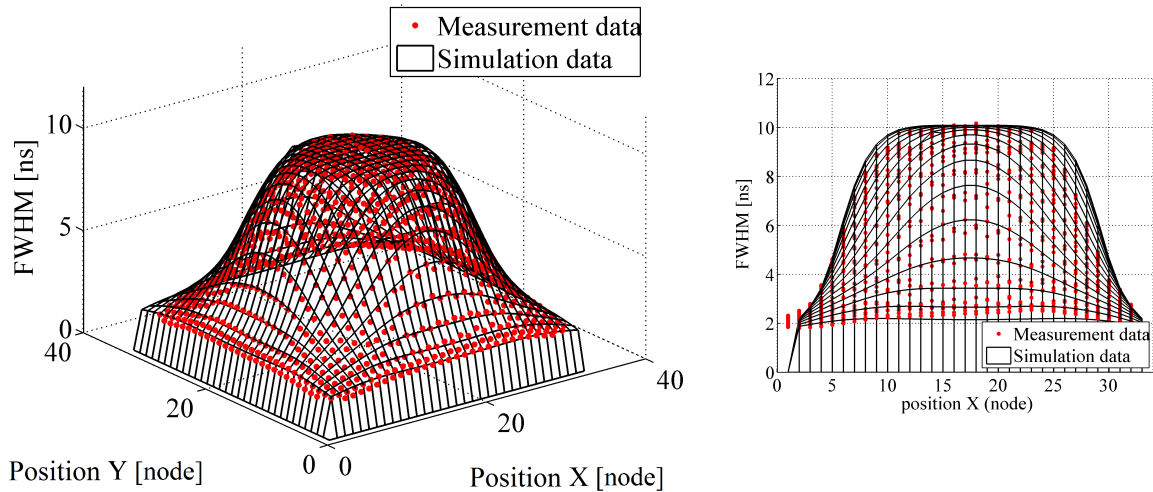


Figure 5.6: The plot of signal FWHM as a function of the light beam position for MAPD-3N detector. Red dots are the measurement data, black mesh represents simulation data. To the right: the XZ view of the same data.

Signal FWHM dependency on width of contact layer

As it was measured and simulated, signal shape dependency on the position of photon hits is strong, but it does not affect the charge of the signal. Knowing the true parameters of the contact layer it is possible to simulate the results for different layer thickness and find the optimum thickness at which the signal shape will be influenced much less. Figure 5.7 shows the results of the signal FWHM and amplitude from the central node as a function of thickness of the contact layer. The red vertical line shows the actual 40 nm thickness of

MAPD-3N contact layer. As it can be seen, the signal FWHM is inversely proportional to the width of the contact layer. Signal FWHM for layer thickness of 200 nm drops below 4 ns what is close to 2.5 ns FWHM observed in the corner of the active area (see figure 5.6). Analogically, the signal amplitude (green plot) grows with the width of the contact layer. Unfortunately, it is not possible to increase the thickness without any consequences. From quantum efficiency point of view, the contact layer is a so called "dead zone", photons absorbed in this region cannot be detected, and in result QE for short wavelengths is very poor. For wavelength of 400 nm, almost all photons are absorbed in first 300 nm of silicon.

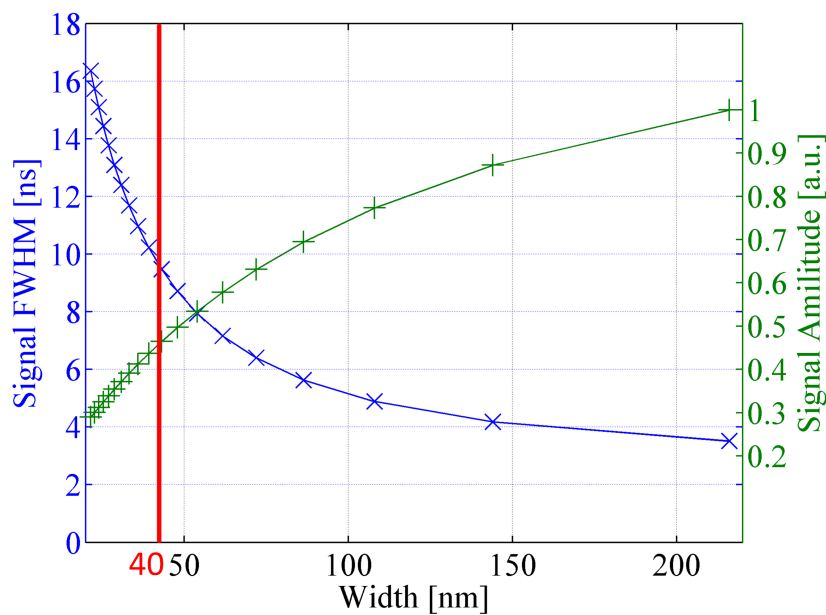


Figure 5.7: Signal FWHM (left axis, blue x symbol) and amplitude (right axis, green + symbol) from the central node as a function of the width of the contact layer.

Summary

Results of measurements of MAPD-3N detector showed strong signal shape dependence on the position of the light beam. The reason of this differences is a very thin p+ contact layer. An electrical model of the contact layer has been proposed and simulated. The results of simulation confirmed that the contact layer introduce changes to the signal response and it is dependent on the position of the electrical signal occurrence. There are several possible solutions to make MAPD-3N signal shape faster and not dependent on photon hit position:

1. Improve the sheet resistance by changing the thickness of p+ contact layer what will drastically reduce the PDE for short wavelengths.
2. There is another solution: introduce a metallic contact grid what will worsen the fill factor and consequently reduce the PDE for all wavelengths in the same proportion. This is probably a better solution, but requires additional process in production, what will increase costs.

The actual design seems to be a reasonable trade-off between PDE and signal shape uniformity. Signal FWHM is less than 10 ns while the PDE in range of 400 nm to 600 nm is around 30 % [19].

The measurement system, results and the model of the contact layer have been shown during the 2015 IEEE Nuclear Science Symposium and Medical Imaging Conference in San Diego as a poster presentation: "An Automated System for Scanning Micropixel Avalanche Photodiodes with a Fast Amplifier" [60].

5.2 Histogram based scans

Using the front-end system for collection of amplitude histograms and laser spot positioning system, it is possible to measure parameters such as gain and relative PDE as functions of the position on the detector surface. Such measurements allow to estimate uniformity of the parameters of the detector. For every position of a pulsed light source, a histogram of signal amplitudes is built, from which various parameters are calculated. In this section some scans of MAPD-3N and MPPC S12572 detectors are presented. Both full detector scan and scans of individual micro-pixels were performed. Scans of the whole detector show the uniformity of the photon detection efficiency and electron gain. Scans in a higher resolution near the edges of the detector provide information on the influence of the deformation of the electric field on the detector parameters.

Initial fast scan of signal amplitude

The first scan of the MAPD-3N has been performed while measuring only the signal amplitude. The scan step has been set to 100 μm . For every position of the laser spot, signal has been measured with an oscilloscope and sent to the computer. The average number of fired pixels was 50 with the FWHM of laser spot of 100 μm . The result of the signal amplitude scan is presented in figure 5.8. The scan has been performed in full range of 13 mm in X and Y planes. The result gives information about position of the

detector's active area. The centre position of the detector is $x \approx 3$ mm, $y \approx 7$ mm. An anode connection pad is visible in the upper-left corner of the detector.

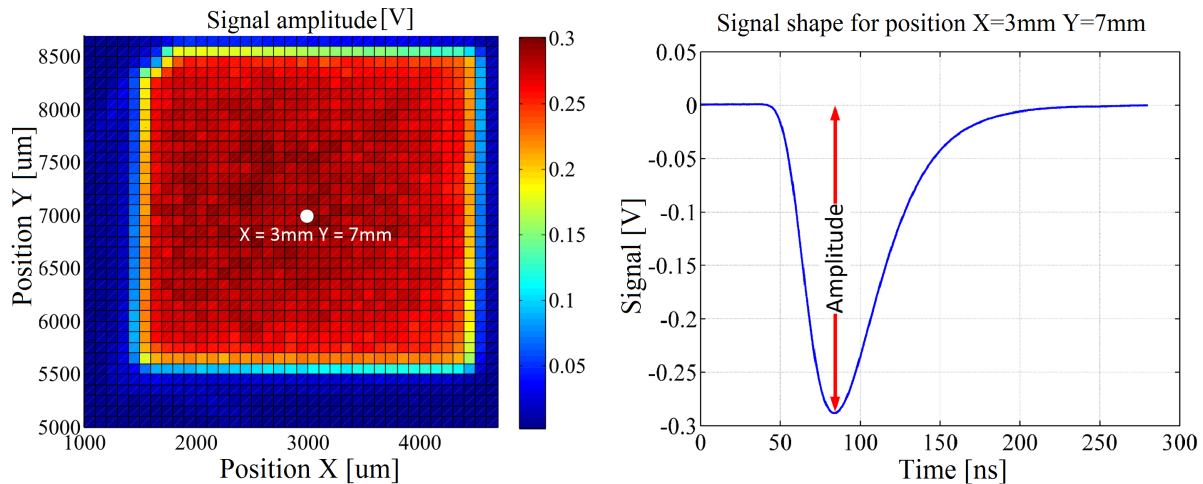


Figure 5.8: To the left: fast scan of signal amplitude of MAPD-3N detector. To the right: typical waveform signal.

Light spot focusing

There is no possibility to directly measure the light spot size on top of the detector active area during the scan. However, for scans with a micro precision a light spot should be as small as possible. The light beam has to be focused on the detector's surface before a scan. For this purpose, a signal amplitude measurement as a function of the distance between the micro-focus lens and the detector surface has to be performed before each scan in XY directions.

Figure 5.9 shows the light beam focusing procedure and measurement results. The initial position $z = 0$ is the closest possible position between the microfocus lens and the detector surface. The measurement is performed in stable temperature and supply voltage for different microfocus lens positions. The global minimum of the amplitude function is the position at which the width of the light beam is the smallest, what means the distance between the lens and the detector surface equals the focal length of the lens. The size of the light spot in a focal point is approximately $3 \mu\text{m}$. For scans which are performed with large steps in XY directions, the light beam diameter is set to be close to the step size.

Rough scans

After the fast scan of signal amplitude, a scan with histogram collection within limited boundaries and the same step of $100 \mu\text{m}$ has been performed. For every position of the

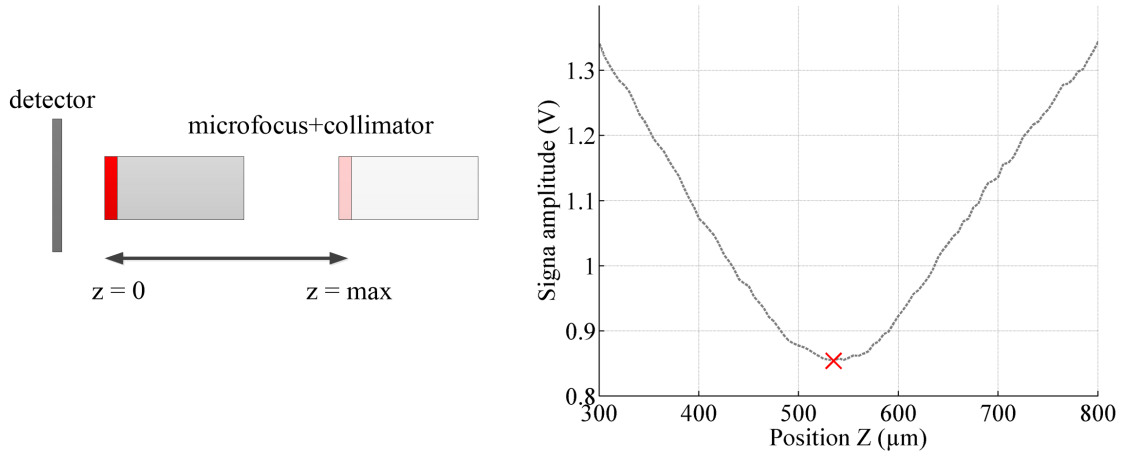


Figure 5.9: Light beam focusing procedure example. The amplitude of the signal as a function of the distance between the detector and the microfocus lens.

laser beam, a histogram of signal charge with $100 \cdot 10^3$ samples has been recorded. A pulse repetition frequency (PRF) has been set to 100 kHz, so the collection of a single histogram took around 1 second. The average number of fired pixels was 2. The FWHM of the laser spot was 100 μm .

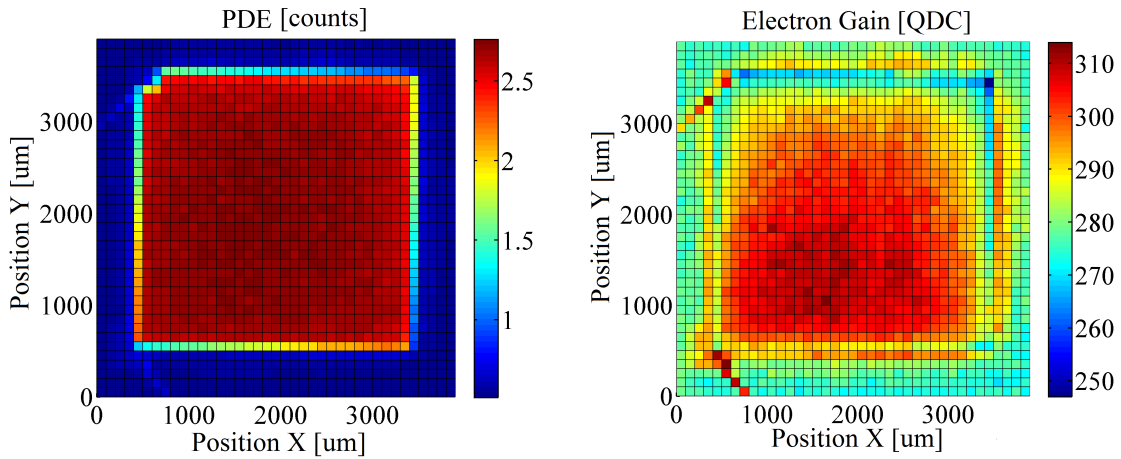


Figure 5.10: The result of MAPD-3N detector scan with histogram collection, $V_{op} = 89\text{ V}$, $T = 16^\circ\text{C}$, light pulse repetition frequency $PRF = 100\text{ kHz}$. Left plot: distribution of relative PDE . Right plot: electron gain measurement.

Results of relative PDE and gain calculation are presented in figure 5.10. Left plot shows the relative PDE as a mean number of fired pixels, right plot shows gain measurements results expressed in the number of channels of charge to digital converter (QDC channels). Comparing these plots, it can be seen that the uniformity of both parameters

looks similar. The gain values drop significantly on top edge of the detector surface. For the corresponding area the mean number of fired pixels is also lower. The gain drop effect near remaining three edges is weaker. What is more, the gain is definitely higher in the bottom half of the detector. Non-zero gain outside the chip area is an effect of dark pulses which enter the integration window. It is lower than the gain within the chip area because of the effect of long recovery time of the detector, explained in section 4.4. Furthermore, lower values of the gain and relative PDE within the chip area are implied by the fact that the breakdown voltage is higher for these areas while the operating voltage (89V) stays the same. This can be caused by a deformation of electric field at boundaries of the active area, electron gain is lower especially near the edges of the detector. It can be seen that there are several outlying points, the reason for that may be local scratches or dust particles on the top of the detector window, which result in lower signal values. The electron gain inside the active area is also influenced by recovery time and high light pulse repetition frequency (100 kHz). This explains higher electron gain values near outer edges of the active area, when only small part of photons hit the pixels. The highest electron gain is obtained from the photons which were reflected from both anode and cathode wires, red lines of pixels near top-left and bottom-left corners of the active area. Photons, reflected from both wires, hit random pixels on the detector surface what reduces the influence of long recovery time.

Scan of anode connection pad

The anode connection pad visible in the left upper corner of the detector has been scanned with a higher resolution. Knowing the position of the detector with 100 μm accuracy, the scan of the connection pad in the upper left corner of the device has been performed with accuracy of 10 μm and with similar light beam diameter. The left picture in figure 5.11 shows the microscope photo of the connection pad and the anode wire. The right picture is the 3d visualisation of mean number of fired pixels as a function of light beam position, the colour map on the right informs about the mean number of fired pixels. As it can be seen, there is a 200 μm by 200 μm square of inactive region occupied by the connection pad. The position of the connection wire is also visible, photons from a focused light beam are reflected and hit random pixels of the active area of the detector.

Two plots in figure 5.12 show the parameters calculated from the same measurement data. The left picture is a colour map of a mean number of fired pixels, the right map shows corresponding electron gain values. From the electron gain measurements in section 4.4, it was showed that the gain measured from dark pulses is lower due to a long recovery

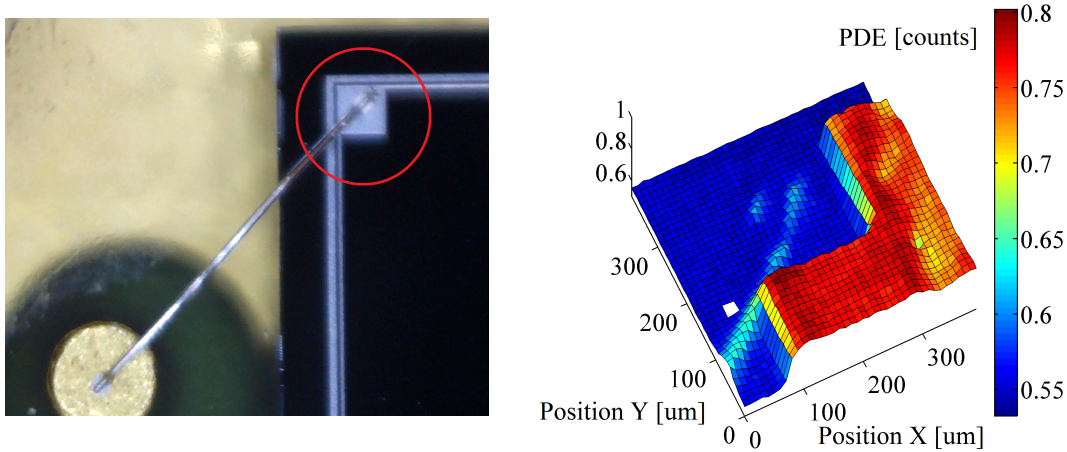


Figure 5.11: Left plot: A microscope photo of MAPD-3N connection pad to anode. Right plot: A 3d plot of signal amplitude scan of $400\ \mu\text{m}$ by $400\ \mu\text{m}$ area.

time of the detector. This phenomenon is also clearly visible in this scan. Knowing that the light beam is well focused on the detector surface and the pulse repetition frequency (PRF) was set to $100\ \text{kHz}$, we can predict that recovery time influence in active region will be visible. On the right plot, we can see that the electron gain value drops significantly when the light beam is over the active area (red points on the left plot). What is more, there is a noticeable drop of electron gain at the edges of the active area, this is probably the effect of deformation of electric field caused by proximity of the pixels near edges to the substrate layer. This effect is not caused by the connection pad, which is placed on top of the connection layer. The highest electron gain (red colour) is obtained for photons reflected from the wire soldered to the connection pad. The light reflected from the wire is no longer focused and hits random pixels, thus there is no recovery time influence and the measured gain is higher. The value of electron gain outside of the active area is the gain calculated from dark pulses.

Figure 5.13 shows the results of a scan in the upper right corner of the MAPD-3N, which does not have the connection pad and a soldered wire. This scan was performed with a light beam step of $10\ \mu\text{m}$, the field of view was $600\ \mu\text{m}$ by $600\ \mu\text{m}$. The light beam pulse was $1\ \text{MHz}$. As it can be seen on the right plot, the electron gain near the edges of the detector is also lower. Observing the inside of the active area, one can see that higher electron gain means higher relative PDE (on the left plot). The electron gain of dark pulses is the same as in figure 5.12, inside the active area the electron gain is lower due to a higher light beam pulse repetition frequency ($1\ \text{MHz}$) and the influence of recovery time.

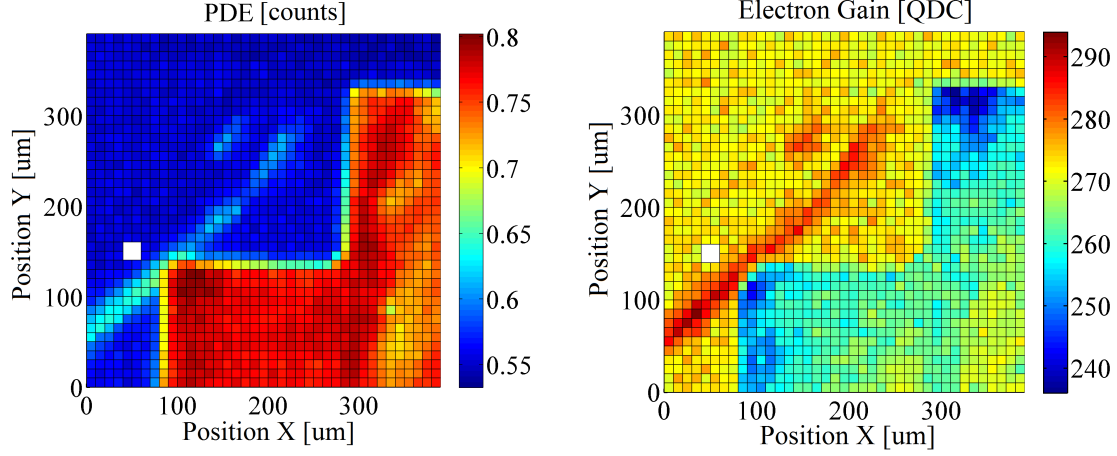


Figure 5.12: MAPD-3N corner scan, $V_{op} = 89$ V, $T = 16$ °C, $PRF = 100$ kHz, field of view $400\ \mu\text{m}$ by $400\ \mu\text{m}$, scan step $10\ \mu\text{m}$; Left plot: Mean number of fired pixels. Right plot: Electron gain calculation.

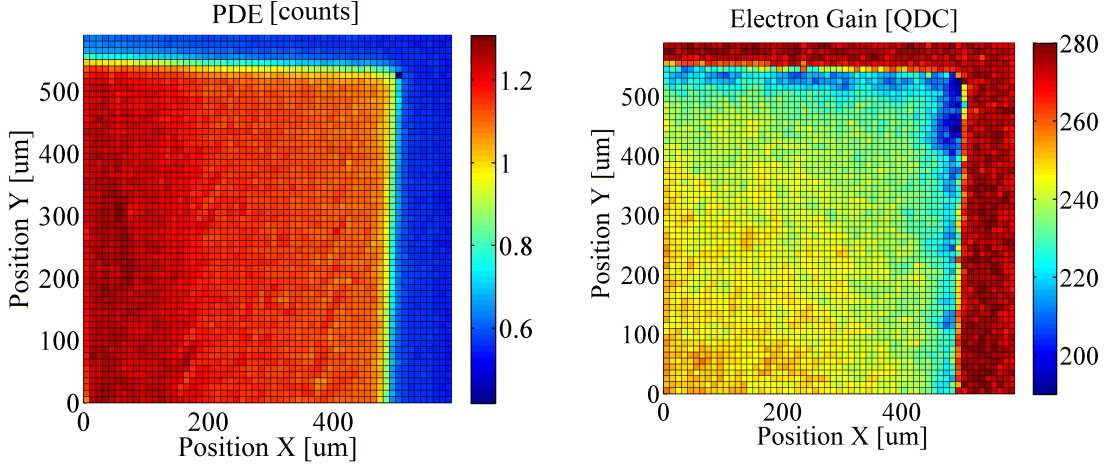


Figure 5.13: MAPD-3N upper right corner scan, $V_{op} = 89$ V, $T = 16$ °C, $PRF = 1$ MHz, field of view $600\ \mu\text{m}$ by $600\ \mu\text{m}$, scan step $10\ \mu\text{m}$; Left plot: Mean number of fired pixels. Right plot: Electron gain calculation.

Micro scan in detector's corner

The next scan was performed in the left upper corner of the active area. To improve the scan resolution, the light beam was set to the lowest possible size of $3\ \mu\text{m}$, and the scan step was set to $2\ \mu\text{m}$. The field of view was shrunk to $300\ \mu\text{m}$ by $150\ \mu\text{m}$ to keep the scan time acceptable. With the scan step of $2\ \mu\text{m}$ it should be possible to distinguish individual micro-cells of the detector.

As it can be seen in figure 5.14, the scan covers the upper part of the scan area from previous scan in upper-left corner (see figure 5.12). The top figure represents relative PDE as a mean number of fired pixels, the red areas (the highest number of counts)

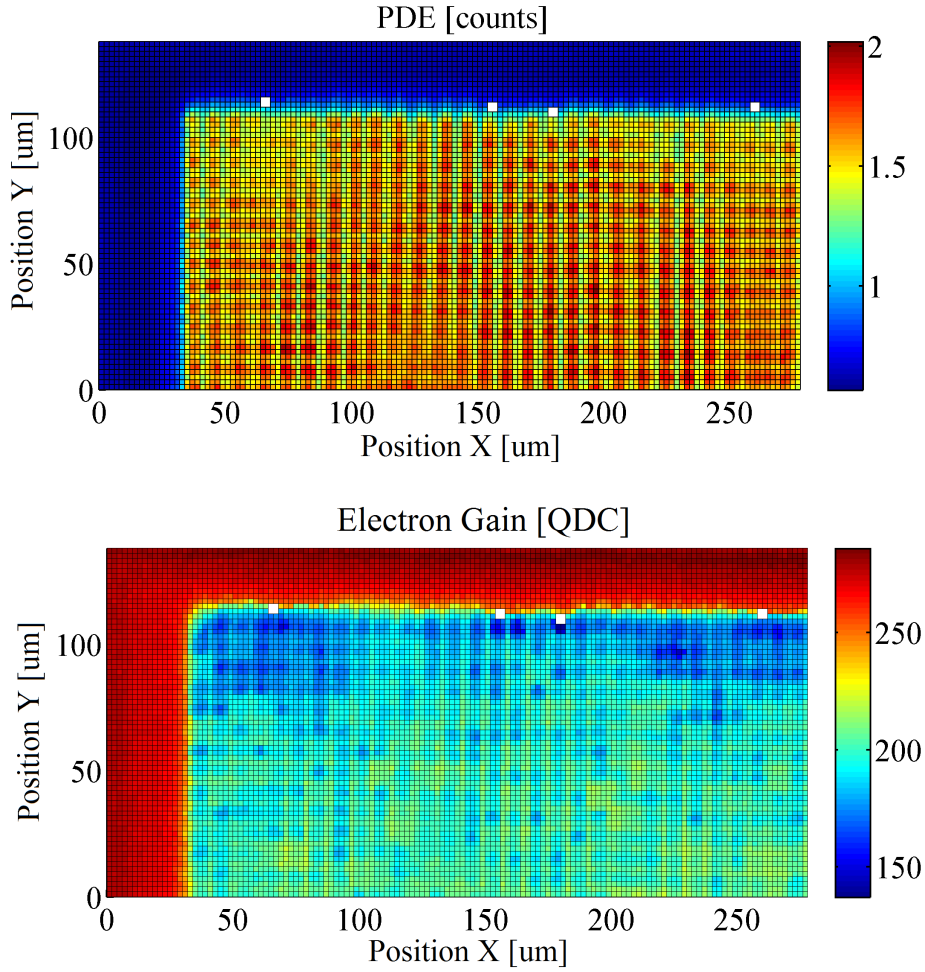


Figure 5.14: MAPD-3N corner scan with high resolution, $V_{op} = 89\text{ V}$, $T = 16^\circ\text{C}$, $PRF = 1\text{ MHz}$, light beam step $2\text{ }\mu\text{m}$. Top figure: mean number of fired pixels, bottom figure: calculated electron gain.

are the positions of micro-wells indicating centres of the pixels. As it can be seen, the mean spacing between red regions is about $8\text{ }\mu\text{m}$ what is the size of a pixel of MAPD-3N detector. It can be noticed that the PDE near the top edge of the active area is slightly lower. The bottom figure shows the electron gain distribution. The anode wire is not visible in this scan. Because of the high light pulse repetition frequency, the highest electron gain is obtained for the light spot positioned over the non-active area when only dark pulses are measured. Within the active area, the electron gain is lower for pixels near the top edge. What is surprising, the pixels with lower electron gain have also lower PDE , this is the effect which was mentioned in previous section. This confirms the effect of deformation of electric field caused by the proximity of the pixels near edges to the n^{++} substrate layer. This deformation causes the non-uniformity in breakdown voltage, which is definitely higher for pixels close to the edge. Higher breakdown voltage, for a

constant supply voltage, results in lower overvoltage and consequently lower PDE and electron gain values.

Micro scan in the centre of the active area

The next scan of MAPD-3N detector has been performed with a step of $1\ \mu\text{m}$. The field of scan was $70\ \mu\text{m} \times 70\ \mu\text{m}$. For this scan the light beam spot on the detector surface was $3\ \mu\text{m}$ (FWHM). The average number of fired pixels was 1. The light pulse repetition frequency has been set to $100\ \text{kHz}$, so the recovery time influence should be visible. The

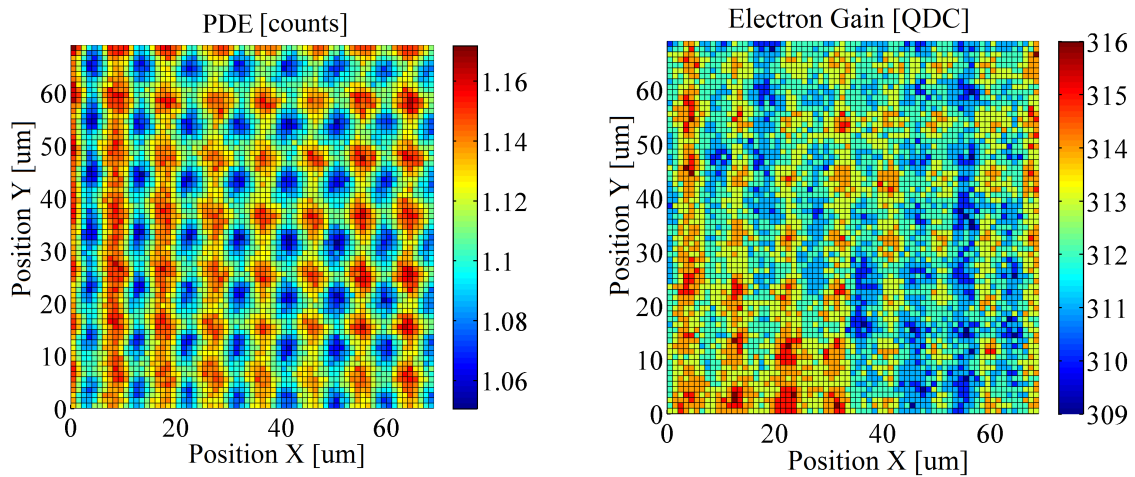


Figure 5.15: Results of MAPD-3N detector scan with histogram collection, $V_{op} = 89\ \text{V}$, $T = 16\ ^\circ\text{C}$, $PRF = 100\ \text{kHz}$, light beam step $1\ \mu\text{m}$. On the left plot - distribution of the relative PDE . On the right plot - gain measurement.

results of the $1\ \mu\text{m}$ scan are shown in figure 5.15. The left plot shows relative PDE with clearly visible positions of buried microwells. The value of the relative PDE for positions corresponding to the microwells ($5\ \mu\text{m}$ width) is only slightly higher when compared to the position between the microwells. This is the effect of the absence of the metallic grid and quenching resistors. The fill factor of the MAPD detectors is almost $100\ \%$. As it was noticed, one can observe small signal drop when photons hit the area between microwells. The gain distribution is presented in the right plot. The gain variations are caused by the effects of the recovery time. When light illuminates the centre of the pixel, the gain value is a little bit lower. When neighbouring pixels "share" the light beam, the recovery time influence on gain is weaker. What is important, there are visible differences in electron gain between individual pixels. These differences are probably the effect of positions and sizes of buried microwells, what means this is a technological effect. What is important, pixels with higher electron gain have also slightly higher PDE , this is not visible in the left figure due to a not suitable colour scale.

Micro scan of MPPC S12572-010

The MPPC detector from Hamamatsu has been also scanned. The device from Hamamatsu has a standard construction with a metallic grid and resistors on top of the detector surface. In second generation of the detector, the quenching resistor is a thin metal resistor placed on the top of active area. Figure 5.16 shows the results of a scan in a centre area of the MPPC detector. This scan was performed with a light beam step of $1\ \mu\text{m}$, the field of view was $75\ \mu\text{m}$ by $75\ \mu\text{m}$. The light beam pulse was $100\ \text{kHz}$. The temperature was set to $16\ ^\circ\text{C}$ and operating voltage to $69\ \text{V}$.

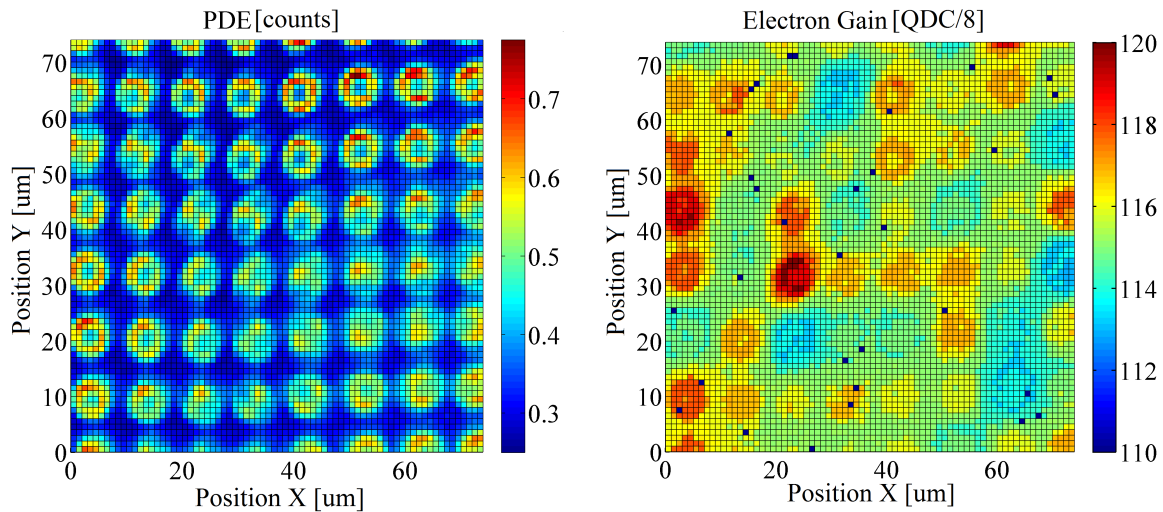


Figure 5.16: Results of MPPC S12572-010 detector scan with histogram collection, $V_{op} = 69\ \text{V}$, $T = 16\ ^\circ\text{C}$, $PRF = 100\ \text{kHz}$, light beam step $1\ \mu\text{m}$. On the left plot - distribution of the relative PDE . On the right plot - gain measurement (NOTE: measured with a different gain stage of QDC).

As it can be seen in figure 5.16, in MPPC device, the relative PDE drops much more when the light spot is positioned between pixels. This is the effect of low fill factor, which is 33% for MPPC with pixel size of $10\ \mu\text{m} \times 10\ \mu\text{m}$. The mean number of counts does not drop to 0 due to the size of light spot, which is around $3\ \mu\text{m}$. What is surprising, there is a noticeable drop of the relative PDE in the centre of each pixel, which can be a result of presence of the contact point between the p+ contact layer and metal quenching resistor. The right plot is the electron gain distribution. Like for the MAPD detector, there are gain differences between the individual pixels. What was predicted, the recovery time influence is not visible for MPPC detector (for comparison see MAPD scan in figure 5.15). The electron drops slightly when the relative PDE is lower (eg. centres of some pixels), what is probably caused by the height of the 1 PE peak and filtering technique.

Histogram scans summary

All presented scans have been performed in stable conditions: temperature of 16 °C and supply voltage of 89 V for MAPD-3N and 69 V for MPPC. The number of fired pixels was determined by laser pulse strength and the size of the light beam on the surface of the detector. The scans of the whole MAPD detector with a step of 100 μm have shown that electron gain uniformity is not perfect. For measured sample of MAPD, the electron gain reaches the highest values in one half of the active area (see figure 5.10) while the gain in the second half is almost 10 % lower. The scans with a higher resolution revealed that the gain is significantly lower for pixels which are near the edges of the active area, what is the effect of the deformation of electric field near boundaries. The precise scans of MAPD with a step of 1 μm showed that the *PDE* is lower for areas around the micro-pixels. The electron gain calculation from individual pixels also showed differences, (which are probably caused by the technological problems) what is the result of dispersions of the breakdown voltage. The measurement system and scan results for MAPD-3N detector have been presented during the International Conference on New Photo-detectors in Moscow in 2015 as a contributed talk: "Fully Automated Machine for Scanning SIMP detectors" [61]. The latest precise scan of MPPC S12572 detector has revealed a lower signal amplitude when the centre of the micro-pixel is being illuminated, what is probably an influence of a connection pad of a quenching resistor.

Chapter 6

Monte Carlo simulation of Geiger discharge

The overall photon detection efficiency is determined by three parameters as given by equation 6.1: QE is quantum efficiency, ϵ is the geometrical fill factor and P_{trig} is Geiger discharge probability.

$$PDE = QE \cdot \epsilon \cdot P_{trig} \quad (6.1)$$

The geometrical fill factor describes the ratio of the effective active area of the detector to the total detector's surface. It is usually around 20 % – 70 % and depends on the density of pixels. The active area is limited by quenching resistors, metal connection grid and optical trenches for crosstalk suppression. In case of MPPC, this parameter is dependent on the technology and will not be included in simulation.

A Monte Carlo simulation of both Geiger discharge triggering probability and quantum efficiency has been performed. An approximate iterative model of avalanche process in a pixel of a SiPM detector initiated by a single photoelectron has been built. A HPK structure of MPPC (Multi Pixel Photon Counter) detector from Hamamatsu (S12725-010C) has been modelled and used for simulation. The MAPD structure (with buried microwells) is much more complicated and difficult to calculate the electric field distribution and perform simulations. The main reason for using HPK reverse structure was the known cross-section of structure of the first generation MPPC detector (S10362-11) published by the manufacturer [7]. As it will be presented in further section, the structure of a new type of MPPC has changed in comparison to model S10362-11, but with proper measurement and analysis it was possible to propose the model of cross section of pixel of MPPC S12725 detector.

6.1 Detector structure

The cross section structure of the old type MPPC detector has been presented by K. Yamamoto in 2007 [7]. The MPPC detector is based on a structure of Si Avalanche Photodiodes called "HPK reverse Structure", with a peak sensitivity wavelength of 450 nm. The HPK reverse structure is a one-sided junction with p-type epitaxial layer on a heavily doped n++ substrate. The HPK (p+/p/n++) structure from figure 6.1 consists of 3 layers. The first p+ layer is a contact layer used for the ohmic contact and it is connected to the metallic connection grid through the quenching resistors. The 300 nm light is almost totally absorbed in the first 20 nm of silicon. When an electron-hole pair is generated in this region, there is a high probability for the electron and hole to recombine, thus it is very difficult to obtain good photon detection efficiency for wavelengths shorter than 300 nm. The p+ contact layer is covered with a protection coating layer made of epoxy resin and with anti-reflection (AR) coating which also limits the sensitivity for deep UV photons. For reversely biased detector, the depletion layer penetrates primarily into the lighter doping side (the p- epilayer). The width of the depletion layer in the n+ substrate can be neglected [62]. An electron photogenerated near the surface drifts through the depletion layer towards the junction interface with the high field region, where the triggering probability is the highest.

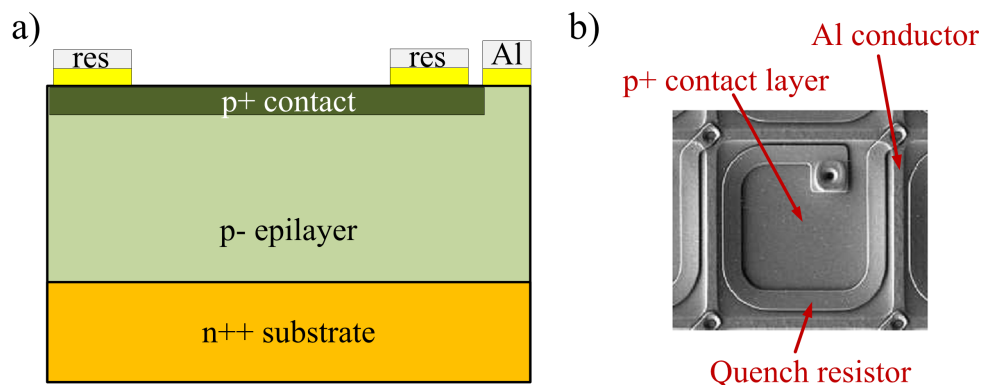


Figure 6.1: MPPC S12572-010 detector. To the left: the junction structure of the old type MPPC detector (HPK reverse structure); To the right: image of a MPPC S12572 which has 25 μm micro-pixel pitches with thin metal resistor placed on top of a photosensitive area, photo from [63].

Under reverse bias, the depletion layer needs to widen in order to dissipate the larger voltage drop across it [62]. At a certain voltage (called depletion voltage V_d) the width of a depletion layer is limited by physical size of the epitaxial layer. The depletion layer of

a single pixel may be modelled as a parallel-plate capacitor with capacitance:

$$C_{pix} = \frac{\epsilon_r \epsilon_0 A}{W} \quad (6.2)$$

where ϵ_r is relative permittivity of silicon, ϵ_0 is vacuum permittivity, A is the surface area of a single pixel and W is the thickness of the depletion region.

MPPC impedance measurement

The impedance measurement of the SiPM detector can give valuable information about detector's structure: pixel capacitances and value of quenching resistors. The MPPC S12572-010 detector, with the bias voltage of 60 V, has been measured with a E5071C Agilent vector signal analyzer.

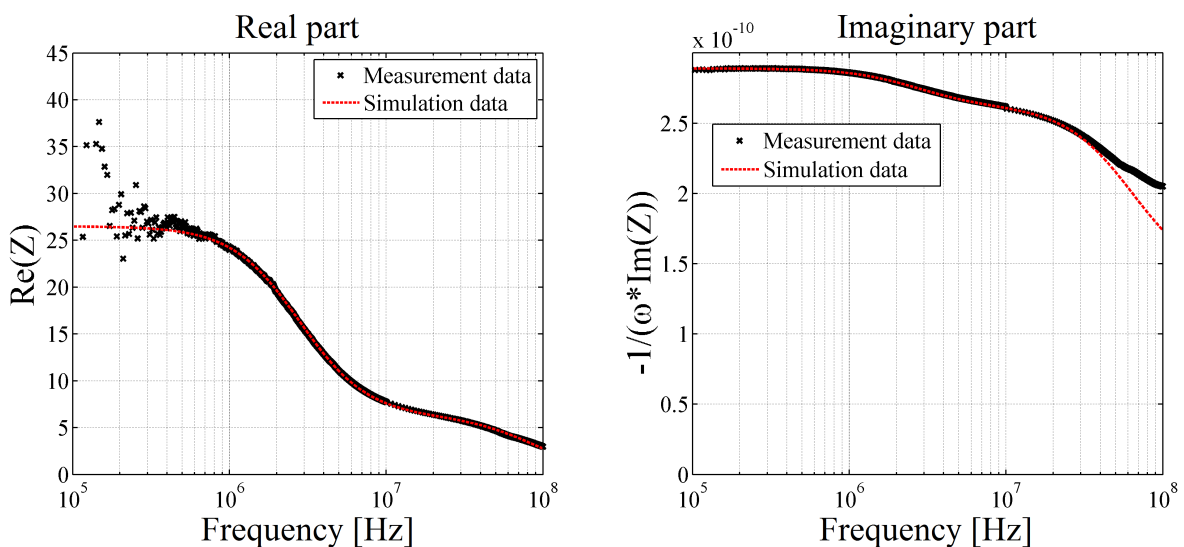


Figure 6.2: MPPC S12572-010 impedance measurement with E5071C Agilent vector signal analyzer. The device has been biased with 60 V. To the left: the real part of measured impedance and model from figure 6.3; To the right: the imaginary part of impedance.

As it can be seen in figure 6.2, the impedance has been measured for frequencies in range from $1 \cdot 10^5$ Hz to $1 \cdot 10^8$ Hz. For lower frequency values the real part of impedance (representing quenching resistors) is noisy. It can be seen that the real part of impedance changes significantly with frequency. It can be concluded that for lower frequencies it is around 27Ω .

A behavioural model of MPPC (see figure 6.3) impedance is plotted with a red dashed line. The impedance of the model fits the measurement data very well. It should be pointed out that, for higher frequencies, simple RC impedance model can't be used to model the MPPC detector. The main reason are small capacitances of a single pixel

and the complicated shape of a metal quenching resistor (see figure 6.1). The thin metal resistor has noticeable parasitic capacitances to both conductor grid and p+ contact layer. The curved shape of the resistor results in an inductive character of this element which is observed for high frequencies. Looking at impedance plots, two points of inflection can be seen. This implies the existence of two parallel RC circuits.

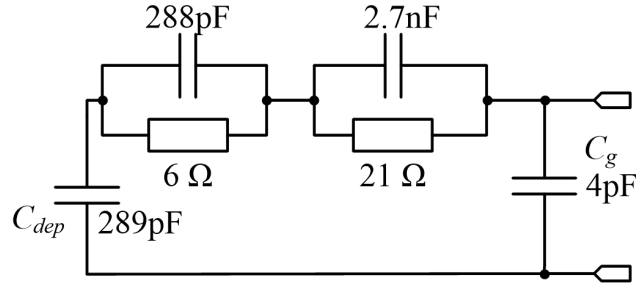


Figure 6.3: Behavioural model of the MPPC S12572-010 impedance.

Figure 6.3 shows the proposed simplified impedance model of the MPPC S12572-010 detector. The values of all components have been chosen empirically to fit the measurement data from impedance measurement. The main capacitor C_{dep} is the sum of capacitances of all pixels (there are 90000 pixels in MPPC S12572-010). This capacitance define the maximum charge of the signal that can be produced by the detector for a given overvoltage. Two parallel RC circuits represent the parallel connection of all quenching resistors and their parasitic capacitances. The $C_g = 4$ pF is the parasitic capacitance of the connection grid and terminals of the detector.

Capacitance calculation from charge measurement The capacitance of the whole detector has been also calculated from pulse charge measurement with a fast amplifier. The whole area of the detector has been illuminated with a 440 nm laser diode. The MPPC detector supply voltage was 71 V at the temperature of 22 °C. Knowing the applied overvoltage and the charge of the pulse response, it is possible to calculate the capacitance of the detector. The left plot in figure 6.4 shows the measurement of signal charge for different light levels. The breakdown voltage for 22 °C is 64.65 V, so the overvoltage is $\Delta V = 6.35$ V. The green curve shows the measurement of a signal charge in proportional mode, it can be seen that the light signal grows linearly with laser tune settings. The signal charge in Gegier mode (blue curve) saturates with value 1.88 nC, what means that almost total surface of the detector is illuminated. The capacitance of depletion region of the whole detector can be calculated with following equation:

$$C_{dep} = \frac{\Delta Q}{\Delta U} = \frac{1.88 \text{ nC}}{6.35 \text{ V}} = 296 \text{ pF} \quad (6.3)$$

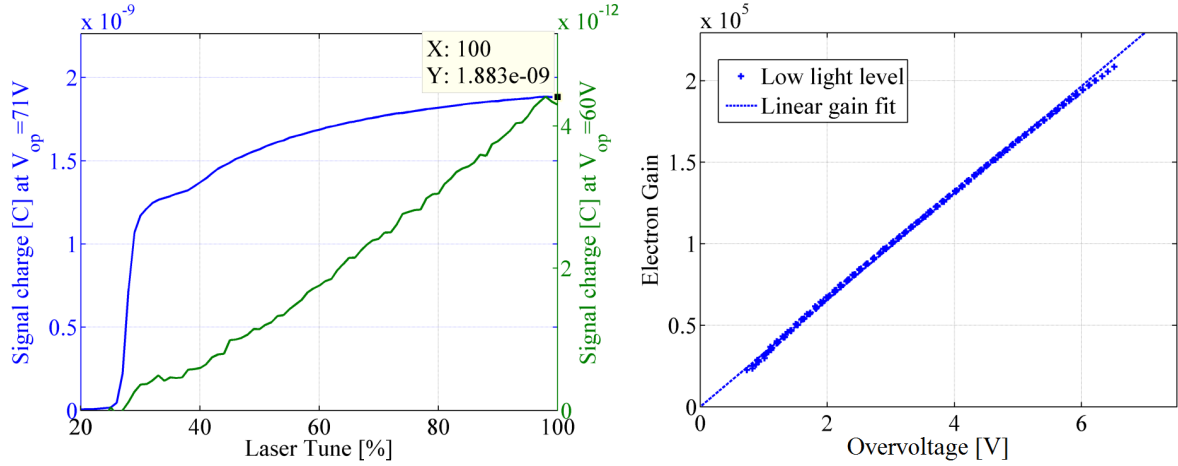


Figure 6.4: MPPC S12572-010 charge measurements at 22 °C. To the left: Signal charge measurement for different light pulses measured at 71 V (in Geiger mode) and at 60 V (in proportional mode). As it can be seen for the measurement in Geiger mode, the output charge saturates at 1.88 nC. To the right: gain measurement calculated from histogram measurements obtained with low light levels for different operating voltages. The pixel capacitance C_{pix} calculated from the gain slope is 5.25 fF.

The capacitance result from charge measurement is slightly higher than the capacitance measured with the vector analyser. The difference is small and may be caused by measurement accuracy. On the other hand, the signal charge which is generated during the ongoing avalanche charges the parallel connection of pixel capacitance and the capacitance which is the result of the parasitic capacitance of quenching resistors, input capacitance of the amplifier C_{amp} (AD8000) and parasitics capacitance of connection grid and terminal connections C_g , like in the figure 6.5. For this reason the capacitance calculated from charge measurements is higher by several percent.

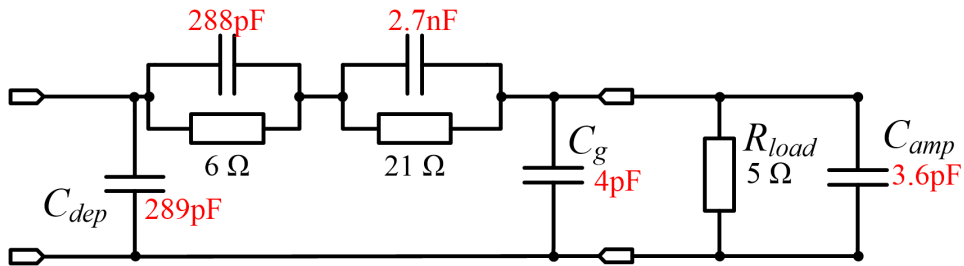


Figure 6.5: Behavioural model of the MPPC S12572-010 impedance for signal measurement with AD8000 amplifier.

Knowing the total number of pixels ($N_{total} = 90000$) the capacitance of single pixel can be calculated.

$$C_{pix} = C_{dep}/N_{total} = 290 \text{ pF}/90000 = 3.22 \text{ fF} \quad (6.4)$$

The right plot in figure 6.4 shows the gain calculation for different overvoltages. The gain values were calculated from histogram measurements. The pixel capacitance can be calculated from the slope of the linear gain fit function:

$$C_{pix-hist} = \frac{\Delta Q}{\Delta U} = \frac{1.97 \cdot 10^5 \cdot 1.6 \cdot 10^{-19} \text{ C}}{6 \text{ V}} = 5.25 \text{ fF} \quad (6.5)$$

As it can be seen, the pixel capacitance is 60% higher in comparison to previously calculated capacitance. The explanation for this behaviour may be the capacitances between neighbouring pixels, which are not visible in impedance measurement neither when the whole detector surface is illuminated. In electron gain measurement only several pixels of the detector are illuminated. When a single pixel is illuminated, the parasitic capacitance to non-illuminated neighbouring pixels results in higher signal amplitude. Thus, the pixel capacitance calculated from electron gain measurements, can lead to wrong conclusions while trying to assess the dimensions of the depletion region in the SiPM detector.

Capacitance characteristic measurement

Having the impedance measurement data for different voltages and a range of frequencies, it is possible to plot the terminal capacitance at a certain frequency as a function of the applied supply voltage. The MPPC S12572-010 capacitance for different operating voltages has been measured with a vector analyser and RLC meter in order to find the reverse bias voltage at which the full depletion of the detector junction is achieved.

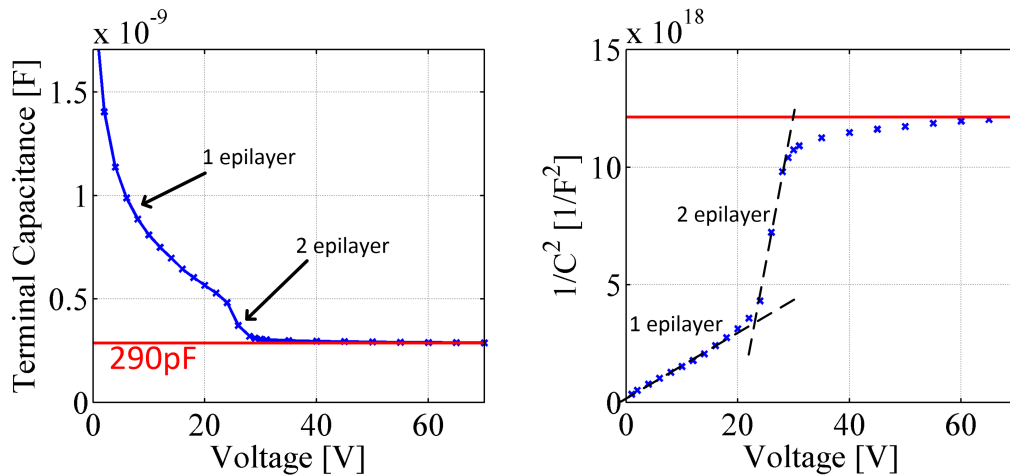


Figure 6.6: MPPC S12572-010 capacitance measurement with vector analyser at 200 kHz. To the left: terminal capacitance measurement for different voltages: To the right: $1/C^2$ plot of the terminal capacitance used to determine doping concentration of epitaxial layer.

The depletion voltage (V_d) can be determined by extrapolating the intersect point of the two fit lines in the region before and after the depletion voltage. As it can be seen on the left plot in figure 6.6, the full depletion is achieved for a voltage of around 30 V. For voltages higher than 30 V the capacitance of the detector decreases very slowly, what is the effect of expansion of the depletion region into highly doped n++ substrate. For the voltage of 70 V, what is the operating voltage, the measured capacitance is 290 pF, what is 10 % less than the value of 320 pF from the device specification [64]. For a diode consisting of one sided abrupt junction with uniform doping and constant area, the dependency $1/C^2$ on the bias voltage is expected to be linear until the depletion voltage is reached. As it can be seen in figure 6.6, the capacitance dependency on voltage is more complicated and it consists of two regions with almost linear $1/C^2$ dependency. The explanation of this characteristic may be that the MPPC S12572 epilayer is divided into two regions with different doping concentration, like shown in figure 6.7. The capacitance measurement results are consistent with the data presented by V. Mikhaylov in [65].

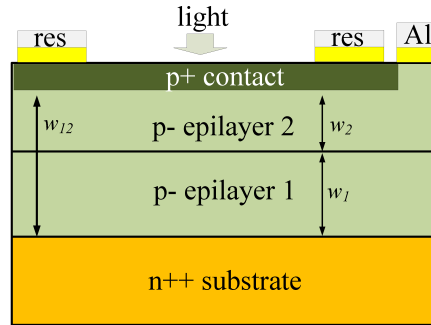


Figure 6.7: MPPC S12572-010. The assumed junction structure of the detector (based on HPK reverse structure) consisting of two parts of epilayer with different doping concentration.

As it can be seen in figure 6.7, the junction consists of two types of epilayer. The first epilayer, with the width w_1 , is positioned close to the junction interface and forms a region with the highest electric field where the charge multiplication occurs. The second epilayer region w_2 , with lower doping concentration, is responsible for the absorption process of electron-hole pairs. The electron generated in the second epilayer is transported to the avalanche region in first epilayer. The thickness of the first epilayer should be thick enough to allow both electrons and holes to ionise, so the avalanche can start. The presence of the second epilayer ensures better light absorption.

MPPC doping profile

Knowing the surface dimensions A and the terminal capacitance of the detector (C_{dep} measured with vector analyser, see figure 6.6), the total width of epilayer w_{12} can be calculated:

$$w_{12} = \frac{\epsilon_r \epsilon_0 A}{C_{dep}} = \frac{11.7 \cdot 8.85 \text{ pF/m} \cdot 9 \text{ mm}^2}{290 \text{ pF}} = 3.2 \text{ } \mu\text{m} \quad (6.6)$$

where $\epsilon_r = 11.7$, $\epsilon_0 = 8.85 \text{ pF/m}$, $A = 9 \text{ mm}^2$. For the calculation of the width of the first epilayer, the capacitance $C_{dep1} = 470 \text{ pF}$ obtained for voltage $V=24 \text{ V}$, as the inflection point of $1/C^2$ curve has been chosen (see figure 6.6).

$$w_1 = \frac{\epsilon_r \epsilon_0 A}{C_{dep1}} = \frac{11.7 \cdot 8.85 \text{ pF/m} \cdot 9 \text{ mm}^2}{470 \text{ pF}} = 2 \text{ } \mu\text{m} \quad (6.7)$$

Knowing the width of the first epilayer and the total thickness of the junction, the width of the second epilayer is $1.2 \text{ } \mu\text{m}$.

$$w_2 = w_{12} - w_1 = 3.2 \text{ } \mu\text{m} - 2 \text{ } \mu\text{m} = 1.2 \text{ } \mu\text{m} \quad (6.8)$$

The concentration of dopants in both junction areas can be calculated from the $1/C^2$ curve slopes from figure 6.6:

$$Na = 2(q\epsilon_0\epsilon_r \frac{1/C^2}{dV})^{-1}/A \quad (6.9)$$

where $\frac{1/C^2}{dV}$ is the slope of the $1/C^2$ curve. For the first epilayer, the linear part covers the voltage range from 0 V to 20 V .

$$Na1 = \frac{2(1.6 \cdot 10^{-19} \text{ C} \cdot 8.85 \text{ pF/m} \cdot 11.68 \cdot \frac{3.14 \cdot 10^{18} \text{ C}^{-2}}{20 \text{ V}})^{-1}}{9 \text{ mm}^2} = 9.51 \cdot 10^{15} \text{ cm}^{-3} \quad (6.10)$$

The depletion in second epilayer builds up for voltages in range from 24 V to 29 V . The doping concentration of the second epilayer can be estimated with:

$$Na2 = \frac{2(1.6 \cdot 10^{-19} \text{ C} \cdot 8.85 \text{ pF/m} \cdot 11.68 \cdot \frac{6.103 \cdot 10^{18} \text{ C}^{-2}}{5 \text{ V}})^{-1}}{9 \text{ mm}^2} = 1.22 \cdot 10^{15} \text{ cm}^{-3} \quad (6.11)$$

Knowing that the most of depletion region covers the two p- epilayer regions and for *PDE* simulation only the epilayer region will be modelled.

Calculation of electric field and ionisation rates

According to above analysis, the depletion region of the MPPC detector consists of two epilayers. Knowing the thickness and the concentration of acceptors in both epilayers it is possible to calculate the electric field and impact ionisation rate for electrons and holes across the pn junction for a known bias voltage. The reverse bias voltage, V_{bias} applied to the pixel, creates a depletion layer of thickness W with mean electric field E_{mean} . The electric field decreases linearly from the junction interface to the edge of the depletion region. In the first epilayer, the electric field is:

$$E(x) = E_{max} - x \cdot \frac{qN_{a1}}{\epsilon_r \epsilon_0} \quad (6.12)$$

in the second epilayer the electric field will be:

$$E(x) = E_{max} - w_1 \cdot \frac{qN_{a1}}{\epsilon_r \epsilon_0} - x \cdot \frac{qN_{a2}}{\epsilon_r \epsilon_0} \quad (6.13)$$

where E_{max} is the electric field at the junction interface and x is the distance from the junction interface.

Ionisation rates The number of electron-hole pairs created by carrier running in unit length is called impact ionisation coefficient. This coefficient is field dependent and it is always higher for electrons. The field dependency of the ionisation rates for electrons (α) and holes (β) has been computed from the measurements of charge multiplication in silicon p-n junction by Overstraeten and Man [66]. The ionisation rates for electrons can be approximated by:

$$\alpha(E) = 7.03 \cdot 10^5 \cdot \exp(-1.231 \cdot 10^6/E) \quad (6.14)$$

for $1.75 \cdot 10^5 \leq E \leq 6.0 \cdot 10^5$ V/cm. The ionisation rates for holes can be approximated by:

$$\beta(E) = 1.582 \cdot 10^5 \cdot \exp(-2.036 \cdot 10^6/E) \quad (6.15)$$

for $1.75 \cdot 10^5 \leq E \leq 4.0 \cdot 10^5$ V/cm.

$$\beta(E) = 6.71 \cdot 10^5 \cdot \exp(-1.693 \cdot 10^6/E) \quad (6.16)$$

for $4.0 \cdot 10^5 \leq E \leq 6.4 \cdot 10^5$ V/cm. Where electric field E is in V/cm and α and β are in 1/cm.

The left plot in figure 6.8 shows the electric field distribution in depletion region for reverse voltage of 70 V. The mean value is $E_{mean} = 70 \text{ V}/3.2 \mu\text{m} = 2.2 \cdot 10^5$ V/cm and the electric field slope is proportional to holes concentration in both epilayers. The right

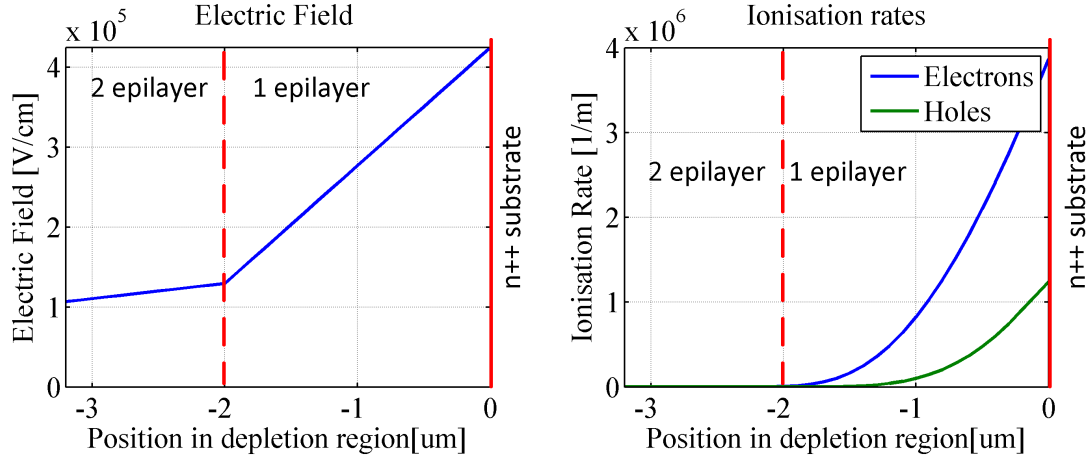


Figure 6.8: Ionisation rate calculation example for reverse voltage $V_{bias} = 70$ V. To the left: Calculated electric field. To the right: Ionisation rates for electrons and holes as a function of position in the depletion region. Solid red line indicates the interface junction.

plot in figure 6.8 shows the ionisation rates for electrons and holes for different positions in depletion region. The calculation of ionisation rates is based on equations from 6.14 to 6.16 and electric field values from the left plot. As it can be seen, in a region close to the junction interface the ionisation rate values are the highest and reaches $4/\mu\text{m}$ for electrons and $1.2/\mu\text{m}$ for holes what high enough for triggering the avalanche. Having a model of ionisation rates across the detector junction, it is possible to perform MC simulation giving the Geiger discharge probability.

Quantum efficiency analysis

As it was mentioned in section 2.2, the quantum efficiency (QE) in SiPM detector represents the probability for a photon to generate an electron-hole pair in the depletion region of the device. QE is the product of two factors: the transmittance of the top layer that covers the detector active area and the internal QE . Both factors are dependent on the wavelength [67]. The first factor can be improved by implementing an anti-reflective coating, the second one is highly dependent on the type of the junction and the width of the depletion layer. For short wavelengths the best results are achieved with HPK structure (p+/p-/n++), where the junction interface is between the epilayer and the substrate. The 400 nm light is almost totally absorbed in the first $0.5\mu\text{m}$ of silicon, so the contact layer (p+) should be as thin as possible (see figure 6.9).

Light Absorption in MPPC S12572. As it was shown in previous section, the epilayer in MPPC S12572 consists of two parts, where the second epilayer ($1.2\mu\text{m}$ thick)

is responsible for absorption of the photoelectrons. Some part of photoelectrons (with higher wavelength) will be also absorbed in the first epilayer (2 μm thick), but the probability for triggering the avalanche will be much smaller, mainly due to shorter path in the region with high electric field.

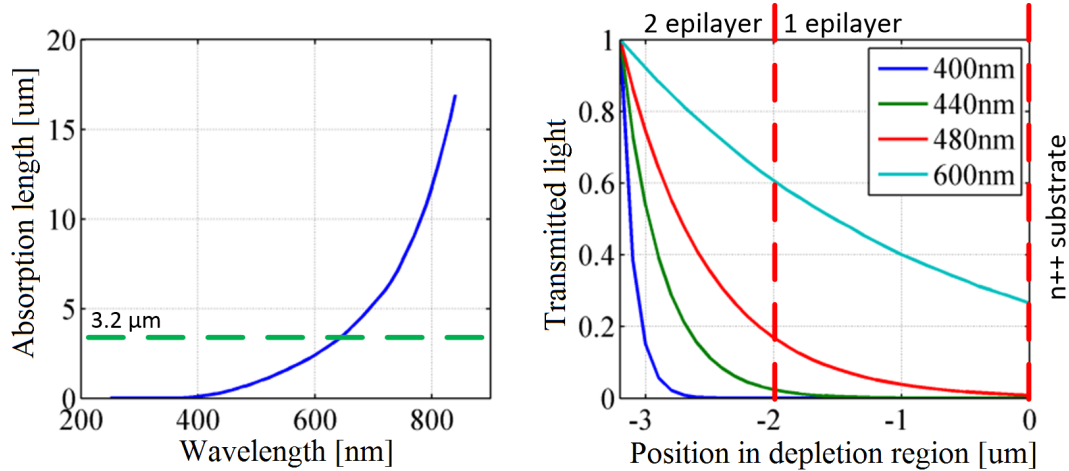


Figure 6.9: Simulation of light absorption in silicon. To the left: Light absorption coefficient according to [68]. Horizontal line for 3.2 μm depletion layer thickness in MPPC detector. To the right: MC simulation of absorption in 3.2 μm depletion region in MPPC S12572 structure.

The left plot in figure 6.9 shows the absorption length of light in silicon as a function of wavelength. The absorption length gives the distance into the material at which the light drops by the factor of e which gives about 36 % of its original intensity. As it can be seen the absorption length grows exponentially with the wavelength. The green horizontal line shows the width of the depletion region in MPPC S12572; it means that 36 % of 640 nm light will be absorbed in the depletion region.

The right plot in figure 6.9 shows the Monte Carlo simulation of light absorption in MPPC depletion region. The figure shows the result for four different wavelengths: 400 nm, 440 nm, 480 nm and 600 nm. As it can be seen, the higher the wavelength, the deeper is the absorption. For 400 nm and 440 nm almost 100 % of the light is absorbed in the second epilayer. The 480 nm light is fully absorbed in the depletion layer, but small part of the light is absorbed in the first epilayer and has smaller probability to trigger an avalanche. Looking at absorption plot 6.9 and ionisation rates from figure 6.8, it is clear that for wavelengths from 400 nm to 480 nm, almost every absorbed photon creates an electron-hole pair in a region preceding the high field, what maximizes the Geiger triggering probability. For 600 nm wavelength, a noticeable part of photons is absorbed in the substrate and cannot trigger an avalanche. The simulation of light absorption does not take into account the p+ contact window, which covers the second epilayer. Its thickness

is estimated to be less than 20 nm, and it fully absorbs the light of the wavelength shorter than 300 nm.

6.2 Simulation procedure

The performed Monte Carlo simulation gives information on the triggering probability dependency of the diode on applied voltage and wavelength. Figure 6.10 shows the MC simulation graph. To start the simulation input data has to be determined: wavelength, diode model, supply voltage. The second phase consists of two parts: the MC simulation of absorption depths (based on the wavelength and diode model) which returns the vector of starting positions of electron-hole pairs. The second part is the calculation of electric field and ionisation rates for a given diode model and supply voltage.

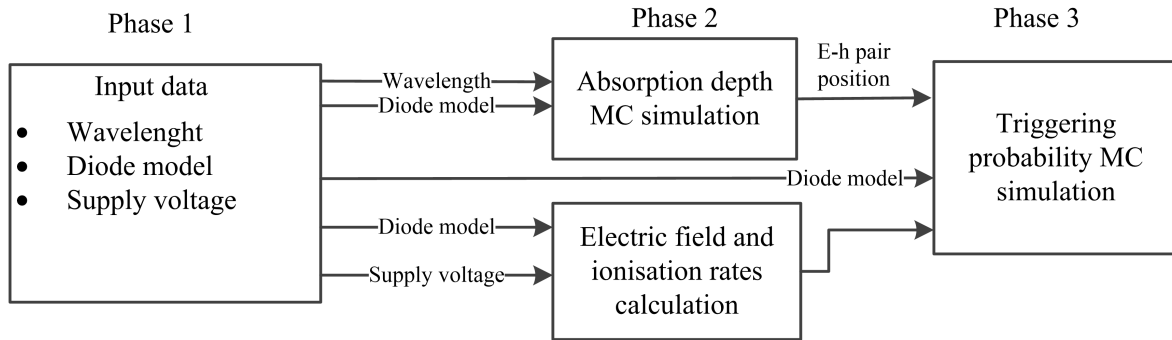


Figure 6.10: Monte Carlo simulation graph. The simulation consists of three phases: determination of input data, diode model calculation, photon absorption depths simulation and the final phase: triggering probability calculation.

The last phase is the MC simulation of the avalanche triggering probability based on the diode model, electric field distribution and the start position of the electron-hole pairs. The triggering probability is calculated by dividing the number of events which resulted with a Geiger avalanche ($N_{positive}$) by the total number of simulated events (N_{total}).

$$P_{trig} = \frac{N_{positive}}{N_{total}} \quad (6.17)$$

The model of the diode is based on the capacitance measurement and analysis from section 6.1. To summarize, the main diode model assumptions are:

- the width of the depletion region is $3.2\mu\text{m}$ and it is divided into two parts with different doping concentrations calculated in equations 6.10 and 6.11,

- the depletion region is equally divided into subregions with a constant width δW , within a single subregion the electric field and ionisation rates are assumed to be constant,
- the applied supply voltage determines the electric field and ionisation rates values across the depletion region (see figure 6.8).

Main assumptions of the triggering probability simulation are:

- the position of first electron-hole pair is determined by photon absorption simulation in silicon,
- for every iteration, electrons and holes move to neighbouring subregions in opposite directions,
- during the carrier movement, a number of new created electron-hole pairs are simulated,
- the simulation can finish with results:
 - positive: electron-hole pair has been ionised by a hole. Since the ionisation rate of electrons is always higher than ionisation rate of holes, the positive feedback from hole and electron impact ionisation has occurred what means that the avalanche process cannot stop,
 - negative: all carriers left the depletion region without impact ionisation initiated by a hole, the Geiger avalanche has not been triggered.

The approach of waiting for the first ionisation caused by a hole is a big simplification, but it is very time-saving. Figure 6.11 presents two different scenarios of the simulation. In this case the depletion region has been divided into 7 subregions in order to show the mechanism of the simulation. Incoming photons enter the depletion region through the p+ connection layer and can create an electron-hole pair in one of seven subregions. Red dashed vertical lines show the iteration points. After every iteration electrons move one subregion towards the substrate (holes move towards p+ contact layer).

Simulation - negative result example. The left picture in figure 6.11 is an example of the simulation with a negative result. As it can be seen, the first electron-hole pair has been created in 6th subregion. After two iterations, the hole has left the depletion region. During the third iteration, a new electron-hole pair has been ionised by the remaining electron, but this is not a condition to finish the simulation. After seven iterations all charges have left the depletion region, what ends the simulation.

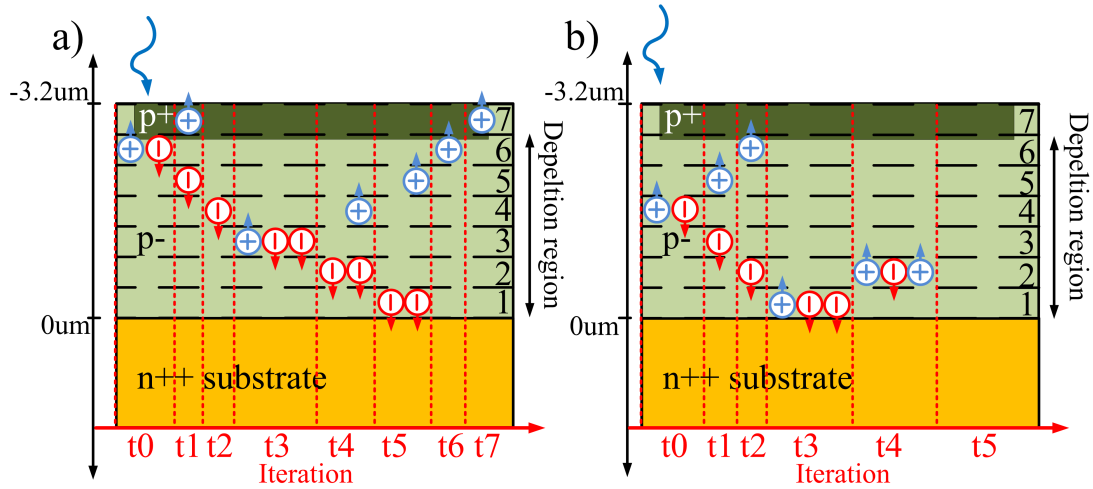


Figure 6.11: Schematic model of triggering probability simulation. Figure a) simulation with the negative result, no ionisation by a hole during the whole process b) simulation with the positive result, ionisation caused by a hole (positive feedback) during the fourth iteration.

Simulation - positive result example. Figure 6.11 b) shows a simulation example with a positive result. The incoming photon has ionised a first electron-hole pair in the fourth subregion. The first ionisation has been caused by the electron after third iteration. A newly generated hole ionised a new pair in the following iteration, what means that positive feedback of ionisation has occurred and the avalanche cannot be stopped. The simulation stops with a positive result after fifth iteration.

6.3 Simulation results

The goal of the Geiger triggering probability simulation is to investigate the dependency of triggering probability on applied voltage, wavelength and the initial position of the electron hole pair. Especially interesting is the analysis of the triggering probability for supply voltages near the breakdown voltage and for voltages much higher, this dependency cannot be investigated in real measurement due to a low electron gain for low overvoltage or to high correlated and dark count noise for high overvoltage.

Geiger triggering probability dependency on supply voltage

The first simulation of Geiger discharge probability has been performed for one wavelength of 400 nm to be sure that all generated photons will be fully absorbed in depletion region of the detector. This simulation should give the information on the dependency of the triggering probability on the applied supply voltage. The simulation input data was:

- wavelength: 440 nm,
- diode model: 32 subregions of 0.1 μm width,
- supply voltage: from 60 V to 100 V.

Figure 6.12 shows the results of the simulation. As it was predicted, the Geiger discharge triggering probability is zero until the breakdown voltage is reached. For 440 nm wavelength, the probability rises with the voltage (at the beginning very slowly, then linearly) and saturates at 100 %. By fitting the central part of the curve, it is possible to find the approximate value of breakdown voltage, which in this case is 72 V. From the authors measurements, the breakdown voltage of MPPC S12572-010 at 26 °C should be around 65 V. 7 V difference seems to be much, but it should be remembered that the calculation of the diode dimensions and doping concentration is affected by not negligible measurement errors.

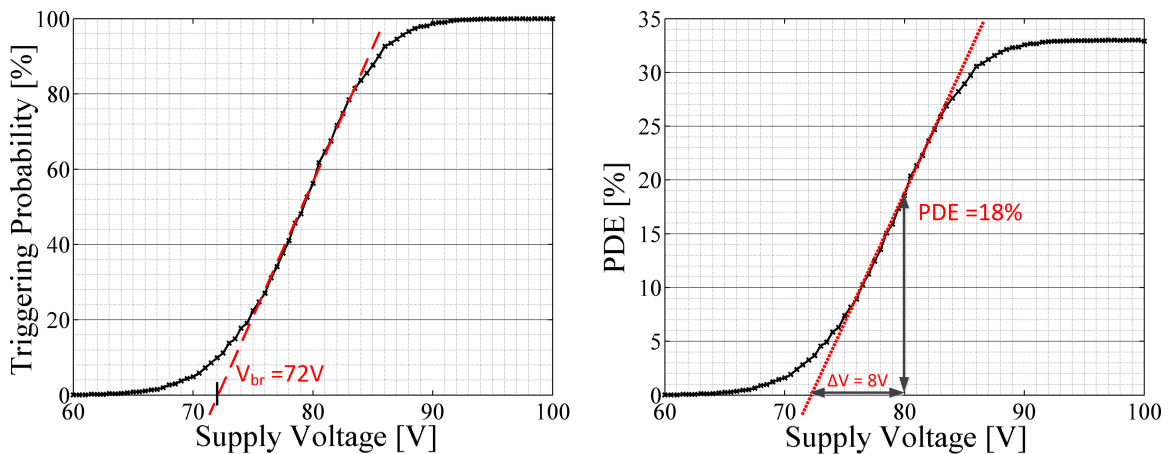


Figure 6.12: Left: Triggering probability simulation result as a function of supply voltage. Simulation performed for wavelength 440 nm Right: Triggering probability simulation result corrected with geometrical fill factor of 33 % from [64]: PDE result as a function of the supply voltage.

The right plot in figure 6.12 shows the results from the left plot corrected with geometrical fill factor of the device which is 33 % [64]. Since the result data contains QE , triggering probability and geometrical factor, it can be treated as photon detection efficiency (PDE). As it is marked on the plot, for 8 V overvoltage the PDE value is 18 %, what is close to the PDE data from the technical specification of the detector [64]. For overvoltages in range from 2 V to 16 V the probability is linearly dependent on the supply voltage, what is also consistent with results from technical specification and author's measurements from [56]. A non-linear characteristic for voltages near breakdown voltage

may be a result of simulation assumption that first ionisation by a hole starts a Geiger discharge.

Geiger triggering probability dependency on electron-hole pair position

Another simulation has been performed to investigate the triggering probability dependency on the position of the primary charge. The simulation has been performed for supply voltages of 75 V, 80 V, 85 V and 90 V. The depletion region has been divided into 32 subregions.

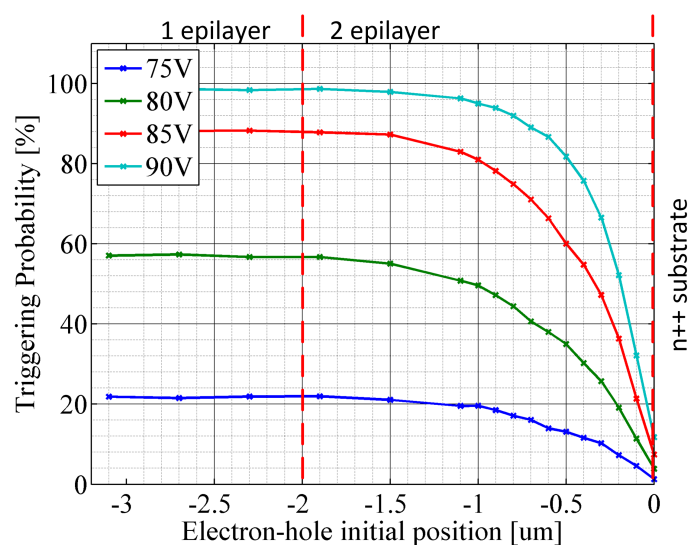


Figure 6.13: Triggering probability simulation results as a function of the initial electron-hole pair position. The simulation has been performed for different supply voltages: 75 V, 80 V, 85 V and 90 V. The red dashed lines show the positions of both epitaxial layers and the junction with substrate.

Figure 6.13 shows simulation results of the triggering probability as the function of the position of primary charge. An electron photogenerated near the surface drifts through the whole depletion layer. The probability is constant for the first 1.5 μm depth. The triggering probability drops significantly when the electron is generated close to the junction interface and the path in high energy field is too short. This behaviour is the same regardless the supply voltage. The results of simulation show that the thickness of depletion region should be always thicker than the thickness calculated from absorption depth for a given wavelength. The thickness of depletion region, at which the probability drops by 10 %, can be called the effective width. For the MPPC S12572 structure, the effective width is the 80 % of the total depletion region width. This can explain the structure of

MPPC S12572, where the depletion region consists of two epilayer regions. Within the first epilayer, where most of absorption takes place, the triggering probability is constant. In the middle of the second layer the triggering probability begins to drop, but this is the region where the charge multiplication occurs. The existence of the first epilayer influences the triggering probability dependency on the wavelength, it widens the wavelength range with the highest sensitivity, what will be simulated in the following section.

PDE dependency on wavelength

As it was already mentioned, the peak sensitivity of the MPPC detector is for blue wavelength. The structure of MPPC S12572 detector has the junction located deep in the bulk in order to obtain the peak sensitivity close to the blue light. To confirm this, a simulation of quantum efficiency as the function of the wavelength has been performed. The simulation has been performed for supply voltage of 90 V. The result should show how the width of the depletion region influences the spectral sensitivity of the detector. The *QE* should be the highest for the wavelength that goes through the contact layer and is fully absorbed in the first 1.5 μm of the depletion region (see figure 6.13).

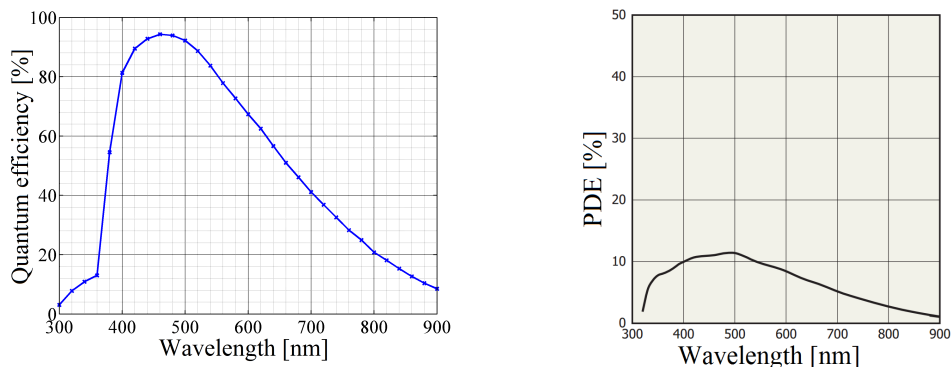


Figure 6.14: To the left: *QE* simulation result as a function of the wavelength. To the right: the photon detection efficiency of MPPC S12572-010 detector [64].

Left plot in figure 6.14 shows the *QE* results for different wavelengths. The simulation has been performed for supply voltage of 90 V. For this simulation, the influence of the width of contact layer has been also taken into account. As it can be seen, the peak sensitivity is obtained for wavelengths from 420 nm to 500 nm, what is consistent with the device specification [64]. The contact layer width has been set to 20 nm, in result the triggering probability drops significantly for wavelength shorter than 360 nm. For longer wavelengths, the probability is limited by longer absorption depths (see also figure 6.9), for 800 nm the probability drops to 20 %. The right plot in figure 6.14 shows the *PDE* of the MPPC S12572-010, as it can be seen the shape of the plot is very similar

to simulation result. The biggest difference is observed for lower wavelengths, what is probably caused by overestimated width of the contact layer p+ and a simplified model which does not include the metal quenching resistor and the AR (anti-reflection) coating.

6.4 Simulation summary

The model of depletion region of MPPC S12572 has been proposed and simulated. It has been build according to the capacitance measurement with different techniques. The measurements showed that the depletion region of the detector has changed in comparison to the previous versions and consists of two layers with different doping concentrations. The important conclusion from simulation is that the probability of Geiger discharge is linearly dependent on the supply voltage for a wide range of voltages, until the saturation point is reached. The simulations showed also that the photons photogenerated near the junction area have much smaller probability to trigger an avalanche. The results of simulation of spectral sensitivity are very similar to *PDE* data from manufacturer's specification.

Chapter 7

Conclusions

Author was involved in building the new electromagnetic calorimeter ECAL0 for COM-PASS experiment in CERN. His main activity was to measure photosensors which were planned to be used in the new calorimeter. Initially the MAPD detector was the only candidate. In the final detector, the MPPC detectors from Hamamatsu have been used. Both detectors have high pixel density and consequently relatively low electron gain. This dissertation contains a detailed description of both standard type Silicon Photomultipliers and novel Micropixel Avalanche Photodiodes. A special automated system with low noise front-end electronics, for measurements and scans of SiPM detectors, has been designed and built.

Author has proposed an electrical model of the MAPD detector. The parameters of the model have been calculated from electrical measurements. The measurements of MAPD detector have shown several issues with the detector. The histogram based measurements have shown that the electron gain from dark pulses is significantly lower from the gain measured with light. Another measurements revealed very long recovery time, which is a result of sophisticated method of quenching avalanches. The investigation led to conclusion that the long recovery time is the reason of lower electron gain calculated from dark pulses. Similar measurement have been performed for MPPC detector. The recovery time of the MPPC detector is much shorter and does not cause such problems. Both histogram based and recovery time measurements revealed that measured electron gain of MAPD device is only a part of charge generated during Geiger discharge. Author has proposed a model of electron gain in MAPD detector.

A big part of research work has been spent on measuring the parameters as the function of the light spot position on the detector's surface. The measurement system with a fast amplifier has been used for measurements of signal shape. Measurements have shown that the shape of signal is dependent on the position of incident photons. Author has

proposed an electrical model of the thin connection layer which was the reason of signal shape deformation. Result of simulation of the proposed model fit the measurement data very well. The same positioning system has been used for scans with a micron precision and histogram measurements. Measurement results have shown that the fill factor of the MAPD detector is not 100 % but its efficiency slightly drops in the region between the microwells. Scans at the edges of the active surface have revealed that electron gain in these areas is slightly lower due to the deformation of the electric field.

Author has proposed and simulated the model of the Geiger discharge probability in SiPM detectors. The model has been based on the HPK reverse structure of the MPPC detector. In order to determine the cross section of the pixel, the impedance for different supply voltages has been measured. The Monte Carlo simulations showed the relation between the triggering probability and the supply voltage and the initial position of first electron-hole pair. Also simulation of spectral sensitivity has been performed with results similar to manufacturer's data.

The results of measurements and simulations of SiPM detectors have been presented on five international conferences [3][56][30][61][60].

Bibliography

- [1] G. F. Knoll. *Radiation Detection and Measurement*. John Wiley & Sons, 1999.
- [2] D. Renker. Geiger-mode avalanche photodiodes, history, properties and problems. *Nuclear Instruments and Methods in Physics Research Section A: Accelerators, Spectrometers, Detectors and Associated Equipment*, 567(1):48 – 56, 2006.
- [3] A. Rychter. Simulation and measurement of super-high density micropixel avalanche photodiodes. In *Photonics Applications in Astronomy, Communications, Industry, and High-Energy Physics Experiments 2012*, pages 84540Q–84540Q. International Society for Optics and Photonics, 2012.
- [4] M. Dziejewicki et al. Study of a 3×3 module array of the ECAL0 calorimeter with an electron beam at the ELSA. In *Journal of Physics: Conference Series*, volume 587, page 012040. IOP Publishing, 2015.
- [5] Z. Sadygov et al. Microchannel avalanche photodiode with broad linearity range. *Technical Physics Letters*, 36(6):528–530, 2010.
- [6] A. Stoykov and R. Scheuermann. Silicon avalanche photodiodes. *Laboratory for Muon Spin Spectroscopy, Paul Scherrer Institut*, 2004.
- [7] K. Yamamoto et al. Newly developed semiconductor detectors by Hamamatsu. *PoS*, PD07:004, 2007.
- [8] P. R. Hobson. Avalanche photodiodes and vacuum phototriodes for the electromagnetic calorimeter of the CMS experiment at the Large Hadron Collider. *Nuclear Instruments and Methods in Physics Research Section A: Accelerators, Spectrometers, Detectors and Associated Equipment*, 604(1–2):193 – 195, 2009. PSD8Proceedings of the 8th International Conference on Position Sensitive Detectors.
- [9] W. Maes, K. De Meyer, and R. Van Overstraeten. Impact ionization in silicon: A review and update. *Solid-State Electronics*, 33(6):705 – 718, 1990.

- [10] S. Piatek. Physics and operation of an MPPC. *Hamamatsu Corporation & New Jersey Institute of Technology*, 2014.
- [11] G. Barbarino et al. *Silicon Photo Multipliers Detectors Operating in Geiger Regime: an Unlimited Device for Future Applications, Photodiodes - World Activities in 2011*. Prof. Jeong Woo Park (Ed.), 2011.
- [12] W. Shockley and W. T. Read. Statistics of the recombinations of holes and electrons. *Phys. Rev.*, 87:835–842, Sep 1952.
- [13] G. Collazuol et al. Studies of silicon photomultipliers at cryogenic temperatures. *Nuclear Instruments and Methods in Physics Research Section A: Accelerators, Spectrometers, Detectors and Associated Equipment*, 628(1):389 – 392, 2011. VCI 2010 Proceedings of the 12th International Vienna Conference on Instrumentation.
- [14] A. Vacheret et al. Characterization and simulation of the response of Multi-Pixel Photon Counters to low light levels. *Nuclear Instruments and Methods in Physics Research A*, 656:69–83, November 2011.
- [15] C. Dietzinger, T. Ganka, A. Márquez Seco, N. Miyakawa, P. Iskra, and F. Wiest. Improved SiPM device performance by introduction of a new manufacturing technology. In *Proceedings of SPIE - The International Society for Optical Engineering*, volume 8847, pages 884703–884703–11, 2013.
- [16] W. G. Oldham, R. R. Samuelson, and P. Antognetti. Triggering phenomena in avalanche diodes. *IEEE Transactions on Electron Devices*, 19(9):1056–1060, Sep 1972.
- [17] K. A. Wangerin, G. C. Wang, C. Kim, and Y. Danon. Passive electrical model of silicon photomultipliers. In *Nuclear Science Symposium Conference Record, 2008. NSS '08. IEEE*, pages 4906–4913, Oct 2008.
- [18] Z. Sadygov, A. Olshevski, I. Chirikov, I. Zheleznykh, and A. Novikov. Three advanced designs of micro-pixel avalanche photodiodes: Their present status, maximum possibilities and limitations. *Nuclear Instruments and Methods in Physics Research Section A: Accelerators, Spectrometers, Detectors and Associated Equipment*, 567(1):70 – 73, 2006. Proceedings of the 4th International Conference on New Developments in Photodetection BEAUNE 2005.
- [19] Zecotek Photonics Inc. MAPD White Paper. <http://www.zecotek.com/media/MAPD-WhitePaper-March-2011.pdf>, 2011. Accessed: 2016-02-12.

- [20] Z. Sadygov et al. Performance of new Micro-pixel Avalanche Photodiodes from Zecektek Photonics. *Nuclear Instruments and Methods in Physics Research Section A: Accelerators, Spectrometers, Detectors and Associated Equipment*, 610(1):381 – 383, 2009. New Developments In Photodetection NDIP08 Proceedings of the Fifth International Conference on New Developments in Photodetection.
- [21] N. Anfimov et al. Novel micropixel avalanche photodiodes MAPD with super high pixel density. *Nuclear Instruments and Methods in Physics Research A*, 628:369–371, February 2011.
- [22] Z. Sadygov. Micro-channel avalanche photo-diode. European Patent 2026386 A1, 02 2009.
- [23] E. Garutti. Silicon photomultipliers for high energy physics detectors. *Journal of Instrumentation*, 6(10):C10003, 2011.
- [24] S. Aoki et al. The T2K side muon range detector (SMRD). *Nuclear Instruments and Methods in Physics Research Section A: Accelerators, Spectrometers, Detectors and Associated Equipment*, 698:135–146, 2013.
- [25] Compass Collaboration et al. COMPASS-II proposal. *CERN-SPSC,(14)*, 2010.
- [26] N. Anfimov et al. Shashlyk EM calorimeter prototype readout by MAPD with super-high pixel density for COMPASS II. *Nuclear Instruments and Methods in Physics Research Section A: Accelerators, Spectrometers, Detectors and Associated Equipment*, 718:75 – 77, 2013. Proceedings of the 12th Pisa Meeting on Advanced Detectors La Biodola, Isola d’Elba, Italy, May 20 – 26, 2012.
- [27] E. Roncali and S. R. Cherry. Application of silicon photomultipliers to positron emission tomography. *Annals of Biomedical Engineering*, 39(4):1358–1377, 2011.
- [28] New compass page. <https://wwwcompass.cern.ch>, 2016. Accessed: 2016-03-31.
- [29] P. H. Abbon et al. The COMPASS setup for physics with hadron beams. *Nuclear Instruments and Methods in Physics Research Section A: Accelerators, Spectrometers, Detectors and Associated Equipment*, 779:69–115, 2015.
- [30] A. Rychter, J. Marzec, G. Domanski, M. Dziewiecki, B. Konarzewski, R. Kurjata, K. Zaremba, and M. Ziembicki. Results of measurements of photodetectors for the ECAL0 calorimeter for the COMPASS-II experiment. In *2014 IEEE Nuclear Science Symposium and Medical Imaging Conference (NSS/MIC), Seattle, USA*, pages 1–5, Nov 2014.

- [31] I. Chirikov-Zorin, Z. Krumshtein, A. Olchevski, V. Utkin, and P. Zhmurin. The design of a module of a new electromagnetic calorimeter for COMPASS II. *Physics of Particles and Nuclei Letters*, 11(3):252–258, 2014.
- [32] M. Dziewiecki. *Measurement-based characterization of multipixel avalanche photodiodes for scintillating detectors*. PhD thesis, Warsaw University of Technology, 2012.
- [33] A. Izmaylov et al. Scintillator counters with WLS fiber/MPPC readout for the side muon range detector (SMRD) of the t2k experiment. *Nuclear Instruments and Methods in Physics Research Section A: Accelerators, Spectrometers, Detectors and Associated Equipment*, 623(1):382–384, 2010.
- [34] M. Dziewiecki, R. Kurjata, J. Marzec, R. Sulej, K. Zaremba, and M. Ziembicki. A system for automated measurement of parameters of large quantities of MPPC detectors. In *International Workshop on New Photon Detectors (PD09)*, 2009.
- [35] M. Tobin. LHCb upgrade: Scintillating fibre tracker. *Nuclear Instruments and Methods in Physics Research Section A: Accelerators, Spectrometers, Detectors and Associated Equipment*, 2015.
- [36] LHCb Collaboration et al. LHCb tracker upgrade technical design report. Technical report, LHCb Collaboration, 2014.
- [37] K. Yamamura, S. Kamada, and K. Yamamoto. History and current status of hamamatsu si detectors for high energy physics experiment. In *10th International "Hiroshima" Symposium on the Development and Application of Semiconductor Tracking Detectors, Xi'an, China*, 2015.
- [38] A. Del Guerra et al. Advantages and pitfalls of the silicon photomultiplier (SiPM) as photodetector for the next generation of PET scanners. *Nuclear Instruments and Methods in Physics Research Section A: Accelerators, Spectrometers, Detectors and Associated Equipment*, 617(1–3):223 – 226, 2010. 11th Pisa Meeting on Advanced Detectors Proceedings of the 11th Pisa Meeting on Advanced Detectors.
- [39] A. Ronzhin et al. A SiPM-based TOF-PET detector with high speed digital DRS4 readout. *Nuclear Instruments and Methods in Physics Research Section A: Accelerators, Spectrometers, Detectors and Associated Equipment*, 703:109 – 113, 2013.
- [40] S. I. Kwon and J. S. Lee. Signal encoding method for a time-of-flight PET detector using a silicon photomultiplier array. *Nuclear Instruments and Methods in*

Physics Research Section A: Accelerators, Spectrometers, Detectors and Associated Equipment, 761:39 – 45, 2014.

- [41] T. Kato et al. Development of a large-area monolithic 4x4 MPPC array for a future PET scanner employing pixelized Ce:LYSO and Pr:LuAG crystals. *Nuclear Instruments and Methods in Physics Research Section A: Accelerators, Spectrometers, Detectors and Associated Equipment*, 638(1):83 – 91, 2011.
- [42] J. Kataoka et al. Recent progress of MPPC-based scintillation detectors in high precision X-ray and gamma-ray imaging. *Nuclear Instruments and Methods in Physics Research Section A: Accelerators, Spectrometers, Detectors and Associated Equipment*, 784:248 – 254, 2015.
- [43] S. Seifert, G. Van der Lei, H. T. Van Dam, and D. R. Schaart. First characterization of a digital SiPM based time-of-flight PET detector with 1 mm spatial resolution. *Physics in medicine and biology*, 58(9):3061, 2013.
- [44] T. Frach, G. Prescher, C. Degenhardt, R. de Gruyter, A. Schmitz, and R. Ballizany. The digital silicon photomultiplier - principle of operation and intrinsic detector performance. In *2009 IEEE Nuclear Science Symposium Conference Record (NSS/MIC)*, pages 1959–1965, Oct 2009.
- [45] R. de Asmundis, G. Barbarino, et al. First results of performance tests of the newly designed vacuum silicon photo multiplier tube (VSIPMT). *Journal of Instrumentation*, 9(04):C04016, 2014.
- [46] G. Barbarino et al. Vacuum silicon photomultipliers: Recent developments. *Nuclear Instruments and Methods in Physics Research Section A: Accelerators, Spectrometers, Detectors and Associated Equipment*, 718:582 – 583, 2013. Proceedings of the 12th Pisa Meeting on Advanced Detectors La Biodola, Isola d’Elba, Italy, May 20 – 26, 2012.
- [47] W. Sansen and Z. Y. Chang. Limits of low noise performance of detector read-out front ends in CMOS technology. *Circuits and Systems, IEEE Transactions on*, 37(11):1375–1382, Nov 1990.
- [48] F. S. Goulding. Pulse-shaping in low-noise nuclear amplifiers: A physical approach to noise analysis. *Nuclear Instruments and Methods*, 100(3):493 – 504, 1972.
- [49] CAEN S.p.A. V965A 8 channel dual range multievent QDC. <http://www.caen.it/>, 2011. Accessed: 2016-01-13.

- [50] J. G. Ziegler and N. B. Nichols. Optimum settings for automatic controllers. *Trans. ASME*, 64(11), 1942.
- [51] S. M. Sze and K. K. Ng. *Physics of Semiconductor Devices*. John Wiley & Sons, 2006.
- [52] K. T. McDonald. Electric field distribution in a reverse-biased p-n junction. physics.princeton.edu/~mcdonald/examples/diode.pdf, 2012. Accessed: 2016-04-12.
- [53] E. A. Jafarova, Z. Y. Sadygov, et al. Features of barrier capacitance of micropixel avalanche photodiodes at different frequencies. *Universal Journal of Physics and Application*, pages 1–4, 2016.
- [54] N. Dinu et al. Temperature and bias voltage dependence of the MPPC detectors. In *Nuclear Science Symposium Conference Record (NSS/MIC), 2010 IEEE*, pages 215–219, Oct 2010.
- [55] J. J. Low et al. Band gap energy in silicon. *American Journal of Under Graduate Research*, 7(1):27–32, 2008.
- [56] A. Rychter. Recent results of measurements of photodetectors for the ECAL0 calorimeter for the COMPASS-II experiment. In *The SPIN-Praha-2014 Conference, Praha, Czech Republic*, Feb 2014.
- [57] W. Shockley. Currents to conductors induced by a moving point charge. *Journal of applied physics*, 9(10):635–636, 1938.
- [58] J. S. Kapustinsky et al. A fast timing light pulser for scintillation detectors. *Nuclear Instruments and Methods in Physics Research Section A: Accelerators, Spectrometers, Detectors and Associated Equipment*, 241(2–3):612 – 613, 1985.
- [59] J. A. Giesecke, M. C. Schubert, B. Michl, F. Schindler, and W. Warta. Minority carrier lifetime imaging of silicon wafers calibrated by quasi-steady-state photoluminescence. *Solar Energy Materials and Solar Cells*, 95(3):1011 – 1018, 2011.
- [60] A. Rychter, J. Marzec, G. Domanski, M. Dziewiecki, B. Konarzewski, R. Kurjata, K. Zaremba, and M. Ziembicki. An automated system for scanning micropixel avalanche photodiodes with a fast amplifier. In *2015 IEEE Nuclear Science Symposium and Medical Imaging Conference (NSS/MIC), San Diego, USA*, pages 1–3, Nov 2015.

- [61] A. Rychter, J. Marzec, G. Domanski, M. Dziewiecki, B. Konarzewski, R. Kurjata, K. Zaremba, and M. Ziembicki. Fully automated machine for scanning SiPM detectors. In *International Conference on New Photo-Detectors (PD15), Moscow, Russia*, pages 1–7, July 2015.
- [62] C. Hu. *Modern Semiconductor Devices for Integrated Circuits*. Prentice Hall, 2010.
- [63] K. Sato, R. Yamada, Y. Takahashi, T. Nagano, and K. Yamamoto. The reliability and reproducibility of MPPC. In *Nuclear Science Symposium and Medical Imaging Conference (NSS/MIC), 2013 IEEE*, pages 1–3, Oct 2013.
- [64] Hamamatsu Photonics. *MPPC S12572-010P technical note*, 12 2015. Accessed: 2016-04-18.
- [65] V. Mikhaylov et al. Radiation hardness tests of avalanche photodiodes for FAIR, NICA, and CERN SPS experiments. In *The European Physical Society Conference on High Energy Physics, 2015 Vienna, Austria, PoS*, Oct 2015.
- [66] R. Van Overstraeten and H. De Man. Measurement of the ionization rates in diffused silicon p-n junctions. *Solid-State Electronics*, 13(5):583 – 608, 1970.
- [67] C. Piemonte. A new silicon photomultiplier structure for blue light detection. *Nuclear Instruments and Methods in Physics Research Section A: Accelerators, Spectrometers, Detectors and Associated Equipment*, 568(1):224 – 232, 2006.
- [68] M. A. Green and M. J. Keevers. Optical properties of intrinsic silicon at 300 K. *Progress in Photovoltaics: Research and Applications*, 3:189 – 192, 1995 1995.

Nomenclature

- ΔV Overvoltage, page 17
- ΔV_{brt} breakdown voltage temperature coefficient of SiPM, page 60
- ϵ geometric factor or fill factor of SiPM, page 19
- ϵ_0 vacuum permittivity, page 55
- ϵ_r relative permittivity of silicon, page 55
- C_g parasitic capacitance of SiPM detector, page 20
- C_{pix} capacitance of single pixel of SiPM, page 20
- ENC equivalent noise charge, page 38
- P_{trig} the probability that the incoming photon triggers geiger discharge in SiPM, page 19
- R_q quenching resistance of SiPM, page 20
- R_s series resistance of SiPM, page 21
- V_d applied reverse voltage at which p-n junction is fully depleted, page 56
- V_{br} breakdown voltage of SiPM, page 14
- V_{op} operating voltage of SiPM, page 17
- APD Avalanche Photodiode, page 9
- CCD Charge Coupled Device, page 51
- CERN The European Organization for Nuclear Research, page 10
- COMPASS COmmon Muon Proton Apparatus for Structure and Spectroscopy experiment in CERN, page 10

CSA Charge sensitive amplifier, page 36

CTAP Cross-Talk and After-Pulsing, page 18

DAQ data acquisition, page 36

DR dark pulses count rate of SiPM, page 18

dSiPM digital silicon photomultiplier, page 33

FPGA Field-programmable gate array, page 33

HEP High Energy Physics, page 11

HPK Reverse Structure p on n pixel structure used in first generation of MPPC devices, page 12

INGRID an on-axis interactive neutrino grid detector in T2K experiment in Japan, page 29

J-FET junction gate field-effect transistor, page 39

LHCb Large Hadron Collider beauty experiment in CERN, page 30

MAPD Micro Pixel Avalanche Photodiode, SiPM detector produced by Zecotek Comapny, page 10

MPPC Multi Pixel Photon Counter, SiPM detector produced by Hamamatsu, page 10

ND280 near detector complex in T2K neutrino experiment, page 24

PCB Printed Circuit Board, page 27

PDE Photon Detection Efficiency, page 19

PE photoelectron, page 63

PET Positron Emission Tomography, page 24

PIN a diode with a wide, undoped intrinsic semiconductor region between a p-type semiconductor and an n-type semiconductor region., page 11

PMT Photomultiplier, page 9

PRF Pulse repetition frequency, page 58

q elementary charge, $q = 1.6 \cdot 10^{-19} \text{ C}$, page 56

QDC charge to digital converter, page 36

QE Quantum Efficiency, page 19

RMS root mean square, page 40

SiPM Silicon Photomultiplier, page 9

SMRD a side muon range detector in T2K experiment in Japan, page 29

SPECT Single Photon Emission Computed Tomography, page 24

SRH Shockley-Hall-Read recombination, Trap-assisted recombination, page 17

T2K Tokai to Kamikoa Experiment, Japan, page 24

TAT Trap-Assisted Tunneling, page 17

VME Versa Module Europa bus, page 44

VSIPMT Vacuum Silicon PhotoMultiplier Tube, page 34

WLS fibres Wave-Length Shifting fibres, page 26

List of Figures

2.1	The structure and electric field strength distribution of an APD with HPK structure.	12
2.2	Impact ionisation coefficient as a function of inversion of electric field[7].	13
2.3	Gain versus bias voltage in avalanche photodiode, adopted from [10].	14
2.4	Schematic of a SiPM matrix of avalanche diodes and quenching resistors.	15
2.5	Signal response linearity of SiPM detectors with two different number of pixels: $N_{2pixels} > N_{1pixels}$	16
2.6	Cross section of pixels surrounded by an optical trench isolation preventing penetration of generated secondary photons to neighbouring pixels.	19
2.7	Schematic of an equivalent electrical model of SiPM detector.	20
2.8	Current pulse generated by an SiPM pixel [10].	21
2.9	To the left: a sectional view of MAPD pixels. To the right: energy band diagram across the APD junction and a top view of the MAPD pixel.	23
2.10	Schematic of an equivalent electrical model of MAPD detector.	24
2.11	Three-dimensional view of the COMPASS setup for measurements with hadron beams. The beam comes from the left side. The upstream part of the setup (beamline) is not shown here [29].	25
2.12	To the left: ECAL0 calorimeter before the final assembly. To the right: ECAL0 detector after cabling, transportation to the final beam position. CERN, April 2016.	26
2.13	Schematic of a module from ECAL0 calorimeter [4].	27
2.14	To the left: MAPD-3N detectors with Winston cones placed on the thermostabilizer. To the right: MPPC aluminium interface PCB boards with smt pads for MPPC detectors on top side.	28
2.15	Location of the detectors in T2K experiment [32].	29

2.16	To the left: A single scintillator module of the SMRD detector - without a light-housing [32]. To the right: a part of automated system for measurement of MPPC detectors: the temperature stabilised feeder for 32 MPPC with preamplifier and LED flasher [34].	30
2.17	To the top-left: a front view of SciFi matrix which is optically coupled a MPPC array detector (bottom-left: zoomed view of MPPC detector). To the right: a photo of Hamamatsu detector S10943-3183 [37]	31
2.18	Pictures of the 4×4 MPPC array developed by Hamamatsu, picture adopted from [41].	32
2.19	Schematic representation of the digital silicon photomultiplier (dSiPM) array. The larger inset depicts a zoom on a single die consisting of four pixels. Each pixel contains 6396 microcells (a number of which are shown in the smaller inset) that are arranged into 4 subpixels.	33
3.1	A simplified schematic of measurement system consisting of: light-tight box with SiPM detector inside, light source, amplifier circuit and data acquisition system for signal sampling and integration.	35
3.2	To the left: signal charge histogram example. To the right: signal waveform sampled with an oscilloscope and full width at half maximum (FWHM) calculation.	36
3.3	A photo of the light-tight box with water cooling system mounted on the front wall and accompanying electronics.	37
3.4	A photo of the inside of the light-tight box.	38
3.5	A schematic of a low noise charge amplifier used in the measurement system.	39
3.6	A schematic of a second stage amplifier.	40
3.7	Equivalent noise scheme of the CSA.	41
3.8	<i>ENC</i> calculation as a function of width of integrating gate.	42
3.9	<i>ENC</i> calculation as a function of number of input transistors.	43
3.10	Schematic of a calibration system.	45
3.11	To the left: Measurement results and linear fit of system calibration procedure. To the right: Deviations of the measured values from linear approximated curve.	45
3.12	Results of system calibration - noise fit of pedestal peak.	46
3.13	Simplified schematic of a front-end electronics and data acquisition system for histogram based measurements.	47
3.14	Simplified schematic of the front-end electronics and data acquisition system for signal shape measurements.	47

3.15	Schematic of the fast amplifier.	48
3.16	Schematic of the temperature control system.	48
3.17	The plot of temperature during the SiPM measurement. Measurement was performed for 7 different temperatures. Zoomed picture shows the part of the plot with temperature change form 24°C to 20°C.	49
3.18	Schematic of a light source and light spot positioning system.	50
3.19	A schematic view of micro-focus lens tests with OmniVision CCD camera. On the bottom: the example picture of laser beam profile taken with CCD camera.	52
3.20	To the left: A photo of laser focus lens tests with CCD camera. To the right: result of laser spot width measurement.	52
4.1	Top: Measurement data and simulation results of MAPD-3N terminal impedance. Bottom: Model of simulated terminal impedance: C_{dep} is the depletion layer capacitance, R_s serial resistance of the p+ contact layer and C_g - parasitic capacitance.	55
4.2	MAPD terminal capacitance measurement: Left: MAPD-3N terminal capacitance as a function of the bias voltage; Right: the $1/C^2$ versus bias voltage curve.	56
4.3	Dependence of the width of the depletion layer of MAPD-3N detector on the supply voltage.	57
4.4	The MAPD histogram measurement; a) MAPD signal responses for a low light level pulses b) sample MAPD signal response histogram, 0 PE peak coloured in black.	58
4.5	Results of gain measurements with low light pulses at temperature 0°C. To the left: histograms for two different operating voltages. To the right: electron gain for different operating voltages (V_{op}) and gain fit function.	59
4.6	Results of MAPD-3N gain measurements for different temperatures with low level light pulses. Top: results of gain calculation as a function of operating voltage for different temperatures, solid lines represent the global fit function for gain. Bottom: The same gain measurements as a function of the overvoltage.	61
4.7	Results of correlated noise measurements: to the left: Correlated noise probability as a function of the overvoltage for temperatures in range 0°C - 12°C. To the right: example of correlated noise measurement for $V_{op} = 88.5\text{ V}$, $T = 0^\circ\text{C}$, $\Delta V = 2.4\text{ V}$. The mean number of fired pixels is 1.76.	64

4.8	Results of electron gain measurements for different temperatures with no incident light. To the left: results of gain calculation as a function of operating voltage for different temperatures, solid lines representing gain fit function. To the right: comparison of gain results with and without incident light pulse as a function of overvoltage.	65
4.9	Results of dark rate measurements and fit function.	66
4.10	Results of dark pulses intervals measurements and exponential fit functions. Time interval distribution for different overvoltages at stable temperature $T = 16^\circ\text{C}$	68
4.11	Results of relative <i>PDE</i> measurements. To the left: relative <i>PDE</i> [PE counts] as a function of the overvoltage for different temperatures. To the right: the same measurement data scaled and fitted with exponential function.	69
4.12	Schematic of a measurement system for recovery time calculation.	71
4.13	Light source strength test. Blue plot: Signal amplitude for MAPD-3N working in Geiger mode, biased at 90V. Green plot: Linear response of MAPD-3N, operating voltage below the breakdown voltage.	72
4.14	Recovery time measurement, signal samples for different delays. Blue plots - reference signals without the recovery effect. To the left: MAPD-3N detector biased at 90V and 22°C . To the right: MPPC S12572-010P biased at 71V and 22°C	73
4.15	Amplitudes of the photoresponse of the MAPD-3N to the second light pulse as a function of the delay time for different operating voltages. To the left: the measured charge of the second response. To the right: signal amplitude relative to the amplitude of the response to the first light pulse. Note the logarithmic time scale.	74
4.16	Schematic diagram showing: (a) the traverse section of MAPD and energy band diagram with applied voltage and (b) two phases of pixel recovery after an avalanche.	74
4.17	To the left: the traverse section of MAPD and three phases of current generation in depletion region. To the right: The schematic of resulting MAPD signal shape.	76
4.18	Electron gain measurement as a function of overvoltage for MAPD-3N (to the left) and MPPC S12572-010 (to the right). Both measurements performed with (blue) and without (red) incident light.	77

4.19	MAPD-3N electron gain measurement as a function of the integrating window length. The measurement has been performed for two wavelengths and without the incident light. Supply voltage is 88.5 V at temperature of 8 °C.	78
4.20	An example of effective minority carrier lifetime (μs) map of a 125 mm \times 125 mm silicon wafer with at a resolution of 122 μm \times 122 μm [59].	80
4.21	A model of MAPD electron gain.	80
5.1	MAPD-3N top view photo. Connection pads and metallic frame marked with arrows.	84
5.2	To the left: the signal charge calculated from recorded signals. To the right: Four signal samples recorder at different light beam position, the colour of the plot corresponds to one of the point on the charge scan.	85
5.3	MAPD-3N signal shape maps. Top-left: signal amplitude, top-right: signal FWHM (full width at half maximum), bottom-left: signal rise time, bottom-right: signal fall time.	86
5.4	Simplified schematic of equivalent circuit of the contact layer with a current source connected to the middle node. The number of nodes in a square lattice can be adjusted.	87
5.5	Results of signal simulation in the central and corner node compared to measurement data. The red plot is the signal from the corner node, the black plot represents signal from the central node. Note: both signals have been scaled to the same amplitude.	88
5.6	The plot of signal FWHM as a function of the light beam position for MAPD-3N detector. Red dots are the measurement data, black mesh represents simulation data. To the right: the XZ view of the same data.	89
5.7	Signal FWHM (left axis, blue x symbol) and amplitude (right axis, green + symbol) from the central node as a function of the width of the contact layer.	90
5.8	To the left: fast scan of signal amplitude of MAPD-3N detector. To the right: typical waveform signal.	92
5.9	Light beam focusing procedure example. The amplitude of the signal as a function of the distance between the detector and the microfocus lens.	93
5.10	The result of MAPD-3N detector scan with histogram collection, $V_{op} = 89\text{ V}$, $T = 16\text{ }^\circ\text{C}$, light pulse repetition frequency $PRF = 100\text{ kHz}$. Left plot: distribution of relative PDE . Right plot: electron gain measurement.	93
5.11	Left plot: A microscope photo of MAPD-3N connection pad to anode. Right plot: A 3d plot of signal amplitude scan of 400 μm by 400 μm area.	95

5.12	MAPD-3N corner scan, $V_{op} = 89\text{ V}$, $T = 16^\circ\text{C}$, $PRF = 100\text{ kHz}$, field of view $400\text{ }\mu\text{m}$ by $400\text{ }\mu\text{m}$, scan step $10\text{ }\mu\text{m}$; Left plot: Mean number of fired pixels. Right plot: Electron gain calculation.	96
5.13	MAPD-3N upper right corner scan, $V_{op} = 89\text{ V}$, $T = 16^\circ\text{C}$, $PRF = 1\text{ MHz}$, field of view $600\text{ }\mu\text{m}$ by $600\text{ }\mu\text{m}$, scan step $10\text{ }\mu\text{m}$; Left plot: Mean number of fired pixels. Right plot: Electron gain calculation.	96
5.14	MAPD-3N corner scan with high resolution, $V_{op} = 89\text{ V}$, $T = 16^\circ\text{C}$, $PRF = 1\text{ MHz}$, light beam step $2\text{ }\mu\text{m}$. Top figure: mean number of fired pixels, bottom figure: calculated electron gain.	97
5.15	Results of MAPD-3N detector scan with histogram collection, $V_{op} = 89\text{ V}$, $T = 16^\circ\text{C}$, $PRF = 100\text{ kHz}$, light beam step $1\text{ }\mu\text{m}$. On the left plot - distribution of the relative PDE . On the right plot - gain measurement.	98
5.16	Results of MPPC S12572-010 detector scan with histogram collection, $V_{op} = 69\text{ V}$, $T = 16^\circ\text{C}$, $PRF = 100\text{ kHz}$, light beam step $1\text{ }\mu\text{m}$. On the left plot - distribution of the relative PDE . On the right plot - gain measurement (NOTE: measured with a different gain stage of QDC).	99
6.1	MPPC S12572-010 detector. To the left: the junction structure of the old type MPPC detector (HPK reverse structure); To the right: image of a MPPC S12572 which has $25\text{ }\mu\text{m}$ micro-pixel pitches with thin metal resistor placed on top of a photosensitive area, photo from [63].	102
6.2	MPPC S12572-010 impedance measurement with E5071C Agilent vector signal analyzer. The device has been biased with 60 V . To the left: the real part of measured impedance and model from figure 6.3; To the right: the imaginary part of impedance.	103
6.3	Behavioural model of the MPPC S12572-010 impedance.	104
6.4	MPPC S12572-010 charge measurements at 22°C . To the left: Signal charge measurement for different light pulses measured at 71 V (in Geiger mode) and at 60 V (in proportional mode). As it can be seen for the measurement in Geiger mode, the output charge saturates at 1.88 nC . To the right: gain measurement calculated from histogram measurements obtained with low light levels for different operating voltages. The pixel capacitance C_{pix} calculated from the gain slope is 5.25 fF	105
6.5	Behavioural model of the MPPC S12572-010 impedance for signal measurement with AD8000 amplifier.	105

6.6	MPPC S12572-010 capacitance measurement with vector analyser at 200 kHz. To the left: terminal capacitance measurement for different voltages: To the right: $1/C^2$ plot of the terminal capacitance used to determine doping concentration of epitaxial layer.	106
6.7	MPPC S12572-010. The assumed junction structure of the detector (based on HPK reverse structure) consisting of two parts of epilayer with different doping concentration.	107
6.8	Ionisation rate calculation example for reverse voltage $V_{bias} = 70$ V. To the left: Calculated electric field. To the right: Ionisation rates for electrons and holes as a function of position in the depletion region. Solid red line indicates the interface junction.	110
6.9	Simulation of light absorption in silicon. To the left: Light absorption coefficient according to [68]. Horizontal line for $3.2\mu\text{m}$ depletion layerL thickness in MPPC detector. To the right: MC simulation of absorption in $3.2\mu\text{m}$ depletion region in MPPC S12572 structure.	111
6.10	Monte Carlo simulation graph. The simulation consists of three phases: determination of input data, diode model calculation, photon absorption depths simulation and the final phase: triggering probability calculation.	112
6.11	Schematic model of triggering probability simulation. Figure a) simulation with the negative result, no ionisation by a hole during the whole process b) simulation with the positive result, ionisation caused by a hole (positive feedback) during the fourth iteration.	114
6.12	Left: Triggering probability simulation result as a function of supply voltage. Simulation preformed for wavelength 440 nm Right: Triggering probability simulation result corrected with geometrical fill factor of 33 % from [64]: <i>PDE</i> result as a function of the supply voltage.	115
6.13	Triggering probability simulation results as a function of the initial electron-hole pair position. The simulation has been performed for different supply voltages: 75 V, 80 V, 85 V and 90 V. The red dashed lines show the positions of both epitaxial layers and the junction with substrate.	116
6.14	To the left: <i>QE</i> simulation result as a function of the wavelength. To the right: the photon detection efficiency of MPPC S12572-010 detector [64]. . .	117

List of Tables

- 2.1 Comparison of Zecotek MAPD and Hamamatsu MPPC parameters [19] 22
- 4.1 Zecotek MAPD parameters comparison for nine samples 62
- 4.2 MAPD dark rate results for nine samples 67
- 4.3 MAPD dark rate measurement comparison for MAPD sample no. 3 at $T = 16^\circ\text{C}$. 68
- 5.1 Calculated parameters of measured signal shapes 85